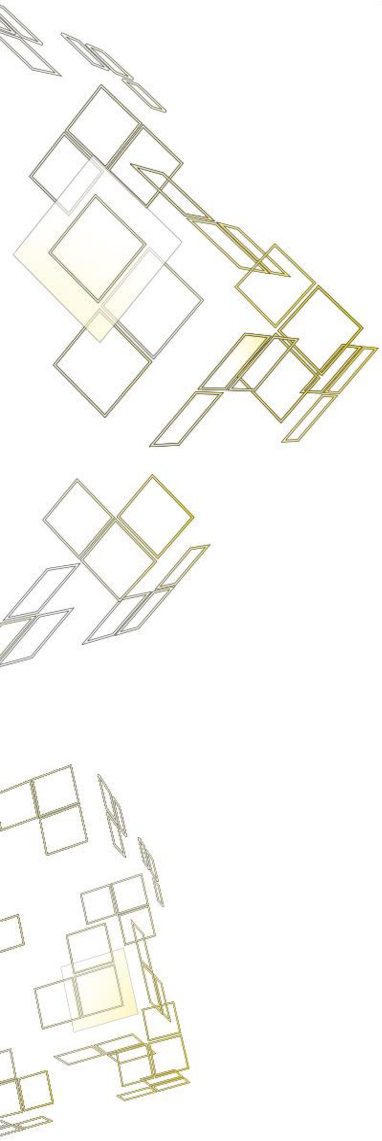

ULTRASHORT PULSED LASER ABLATION IN MASS PRODUCTION OF SMALL METAL PARTS

INCREASING ABLATION EFFICIENCY AND REDUCING HEAT INPUT

MASTER THESIS

JELMER M. VIS

ENGINEERING TECHNOLOGY – MECHANICAL ENGINEERING

CHAIR OF LASER PROCESSING

08-2023

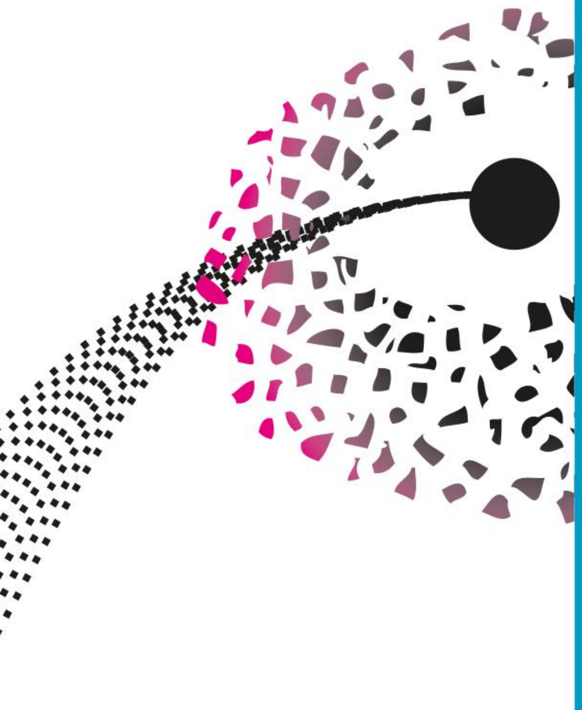

UNIVERSITY OF TWENTE.

COLOPHON

GRADUATION COMMITTEE
Prof.dr.ir. G.R.B.E. Römer (chair)
Dr. M. Feinaeugle (internal member)
Dr. G.G.M. Stoffels (external member)
MSc. M.L Stok-Van Houwelingen (observer)

COMPANY
Philips Drachten
Ing. F. Vrijburg
Ing. J. Buitendijk

DATE
08-2023

AUTHOR(S)
Jelmer Maarten Vis

EMAIL
J.M.Vis-1@student.utwente.nl

POSTAL ADDRESS
P.O. Box 217
7500 AE Enschede

WEBSITE
www.utwente.nl

PREFACE

In this thesis, all information about my master's thesis, ultrashort pulsed laser ablation in mass production of small metal parts: increasing ablation efficiency and reducing heat input, is presented, and discussed. The master's thesis is conducted in collaboration between the Chair of Laser Processing at the University of Twente and Philips in Drachten.

I would like to thank Martijn Stok-Van Houwelingen and Gert-Willem Römer for the periodic meeting to discuss different ideas. Also, a great contribution to my thesis was the availability of the laser setup at the University of Twente including all the help that was needed to get it working and calibrated according to the needs.

Without Philips, mainly Folkert Vrijburg and Jeroen Buitendijk, I would not have had the possibility to learn about the practical use of ultra-short pulse laser systems or the resources to manufacture the experimental setups. Many ideas were generated within our meetings on how to implement USP laser systems in the production process. Hereby, I would like to thank Folkert Vrijburg, Jeroen Buitendijk, and all other Philips employees who helped to make this research a success.

All-in all, it was incredible to work with the high-tech equipment and to broaden my knowledge on laser material processing.

8-2023
Jelmer Vis

SUMMARY

This study set out to investigate the feasibility of ultrashort pulsed (USP) laser ablation in a mass production environment. Achieving dimensional accuracy of small metal parts is among the biggest challenges in manufacturing. USP laser ablation can be used as a post-processing step to achieve this. However, the main driving factor in a mass production environment is the cost per part, so the ablation rate needs to be maximized while maintaining a proper surface finish and without overheating the part.

The existing literature on this subject is extensive, but a research gap was found for the optimum wavelength for AISI 420 steel and the way in which the heat input changes with different sets of laser settings. The quality of the ablated surface can be described by the roughness and cone-shaped defects induced by either too high or too low laser fluence. Studies on the heat input of USP laser ablation are limited, and typically only single laser settings are evaluated. These studies observed that the residual energy coefficient (REC), which is the fraction of the total incident laser energy that is converted to heat instead of ablation or reflection, is around 34% for stainless steels. Studies directed at optimizing the ablation efficiency ($mm^3/(W \cdot min)$) showed: a peak in ablation efficiency at a certain (optimum) laser fluence; an optimum of the pulse duration is approximately 1 ps; a wavelength around 517 nm is optimal; the pulse repetition rate shows particle shielding and heat accumulation; an increase in laser spot size lowers the ablation efficiency; and burst mode also lowers the ablation efficiency. A novel technique referred to as “ablation cooling” shows promising results, but the technique is not yet well understood. Studies aimed at high ablation rates showed ablation rates of up to 42.42 mm^3/min using a high average laser power of 312 W.

Besides a literature study, experiments were conducted to determine of the most efficient wavelength to ablate AISI 420 stainless steel and to determine the REC values for different laser fluence levels. Also, experiments were conducted to measure the surface roughness, to check for defects at different average laser powers, to measure the relative absorbance of AISI 420 stainless steel, and the performance of a forced air-cooling system for a small metal part. A sample and sample holder were designed for ablation efficiency and REC measurements, aiming at minimizing the heat losses during the process. A Z focus scan was used to find the focus location by ablating and analysing lines at different Z heights. A knife-edge measurement was used to measure the laser spot size in the focus location. Different laser fluence levels at 1028 nm, 514 nm, and 343 nm laser wavelengths were used in an ablation process using a constant average laser power of 0.1 W. The peak ablation efficiency for 1028 nm is 0.227 $mm^3/(W \cdot min)$, for 514 nm 0.259 $mm^3/(W \cdot min)$, and for 343 nm 0.259 $mm^3/(W \cdot min)$. The ablation efficiency results fit well with a theoretical model for the ablation efficiency. The increase in ablation efficiency, when using a wavelength of 514 nm instead of 1028 nm, could be explained by the increased laser absorption at this wavelength. Converting a common laser beam wavelength of 1028 nm to 514 nm by using a second harmonic generator results in pulse energy losses. For the three wavelengths, the REC has a peak at lower laser fluence levels and seems to stabilize around 27% at higher laser fluence levels. A derived equation from a model where laser fluence below the ablation threshold is converted to heat, shows similar behaviour to the presented results. The experiments aimed at assessing the surface quality at different average laser powers shows that the roughness and defects are not dependent on the average laser powers in the studied range. The surface quality issues can increase with an increasing ablation depth and so an ablation process of only a few µm depth could be less sensitive in terms of surface quality. Forced air cooling of a small metal part shows promising results, with the maximum temperature dropping from 267 °C to 74 °C when cooling is applied, enabling the use of higher average powers.

LIST OF ABBREVIATIONS

CLP	Cone like pillars
IIC	Inclusion induced cones
REC	residual energy coefficient
SEM	Scanning Electron Microscope
SHG	Second Harmonic Generation
THG	Third Harmonic Generation
USP	Ultra-Short pulse
UT	University of Twente

NOMENCLATURE

Variable	Definition	Unit
$\dot{V}/P_{av}$	(Theoretical) ablation efficiency	$mm^3/(W\cdot min)$
δ	Energy penetration depth	nm
F_0	Peak laser fluence	J/cm^2
$F_{0,th}$	Ablation threshold	J/cm^2
$F_{0,opt}$	Optimum peak laser fluence	J/cm^2
$F_{0,th}(N)$	Ablation threshold after N laser pulses	J/cm^2
$F_{0,th,1}$	Ablation threshold laser fluence without heat accumulation	J/cm^2
N	Number of laser pulses	-
s	Incubation coefficient	-
$\dot{Q}_{in}$	Ingoing heat flow	W
$\dot{Q}_{out}$	Outgoing heat flow	W
REC	Residual Energy Coefficient	-
P_{av}	Average laser power	W
H_c	Heat loss constant	W/K
ΔT	Temperature difference between sample and environment	K
E_{sample}	Internal energy	J
c_{av}	Average heat capacity of the material	$J/(kg\cdot K)$
m	Mass	kg
T_{av}	Average temperature	K
a	Temperature difference with environment at the start of the cooling cycle	K
r	Coefficient of heat transfer	-
T_{env}	Environment temperature	K
t	Time	s
$\dot{T}$	Temperature flow	K/s
Q_c	Power loss due to suspension arms	W
k	Average thermal conductivity AISI 420	$W/(m\cdot K)$
A_{arms}	Cross section of suspension arms	m^2
dT/dx	Temperature gradient in suspension arms	K/m
n	Number of suspension arms	-
Q_r	Heat flow due to radiation	W
σ	Stefan-Boltzmann constant	$W/(m^2\cdot K^{-4})$
ϵ	Emissivity coefficient of the material	-
$A_{radiation}$	Radiation area	m^2
ΔT	Temperature difference of the sample with the environment	K
A	Laser spot surface area	cm^2
f	Laser pulse repetition rate	kHz
E	Energy in a laser pulse	µJ
OL	Geometrical pulse-to-pulse overlap	%
w_0	Laser spot size radius	µm
v	Laser beam speed relative to workpiece	m/s
$P_{measured}$	Measured laser power after knife-edge	W
P_{offset}	Measured laser power with blocked laser	W
h	Location of knife-edge	µm
h_0	Centre location of laser beam	µm

TABLE OF CONTENTS

Summary ii
List of abbreviations iv
Nomenclature vi
1. Introduction 1
  1.1 Background 1
  1.2 Problem definition 1
  1.3 Research objectives 1
  1.4 Requirements 2
  1.5 Scope of this thesis 2
2. State-of-the-art 5
  2.1 Basics of USP laser ablation 5
  2.2 Processing Quality 6
  2.3 Residual Energy Coefficient and Surface Structures 7
    2.3.1 Residual Energy Coefficient 7
    2.3.2 Model/prediction of surface structures and heat accumulation 8
  2.4 Laser ablation Efficiency 10
    2.4.1 Laser fluence 10
    2.4.2 Pulse duration 11
    2.4.3 Wavelength 11
    2.4.4 Pulse repetition rate 13
    2.4.5 Laser spot size 15
    2.4.6 Burst mode 15
  2.5 High troughput USP ablation 18
    2.5.1 High throughput ablation 18
    2.5.2 Post processing to improve the surface quality after USP laser ablation 19
  2.6 Summary 20
3. Experimental setup & methodology 23
  3.1 Experimental setup 23
    3.1.1 Laser setups 23
    3.1.2 Material and samples 25
    3.1.3 Sample holder 27
    3.1.4 Knife-edge setup 28
    3.1.5 Integrating sphere 29
    3.1.6 Analysis tools 29
  3.2 Methodology 30
    3.2.1 Sample preparation 30
    3.2.2 Knife-edge method 30
    3.2.3 Integrating sphere 30

3.2.4 Surface finish at different average laser powers 30
3.2.5 Ablation efficiency method........ 31
3.2.6 Heat accumulation method 32
3.2.7 Cooling of a shaving head........ 33
3.2.8 Laser settings 34
3.3 Validity/error analysis 35
4. Results........ 37
4.1 Knife-edge spot size measurement 37
4.2 Surface finish at different laser powers. 39
4.3 Intergrating sphere........ 41
4.4 Ablation efficiency 42
4.5 Heat input 46
4.6 Cooling of a shavinghead 47
5. Conclusions & recommendations........ 49
5.1 Conclusions 49
5.2 Recommendations 50
Bibliography 51
Appendices........ 57

1. INTRODUCTION

1.1 BACKGROUND

Dimensional accuracy and precision of small metal parts at a scale of 10 µm are among the biggest challenges in manufacturing. Currently used techniques can produce the parts within specifications, but research is conducted to replace the sometimes chemical and power-hungry processes with more sustainable, cheaper, and more capable alternatives. These alternatives cannot always deliver the dimensional accuracy needed for small metal parts. Critical deviations in the dimensions are in the order of 10 µm and in some cases this inaccuracy can lead to lower performance or even reduced functionality of the part. Ultra-Short Pulsed (USP) laser ablation can be a suitable tool as a post-processing step for the parts to remove the deviations and make the products compliant which the requirements [1]. The use of USP laser ablation as a material processing technique is not yet widespread, especially in mass production environments.

USP laser ablation has five key benefits [1], [2]:

- high precision material removal at the scale of (sub) micrometers,
- it is a contact-free process, practically no forces are exerted on the part,
- it is possible to process a wide range of materials,
- the process typically induces a low thermal load,
- low surface roughness can be reached.

USP laser ablation is already used in industrial applications such as optoelectronics production (display cutting), in the medical field for devices (stents, surgical tools) [3], wafer dicing, black marking, intra-glass marking, and the cutting of composite materials [4]. Emerging applications are the production of hydrophobic surfaces, glass-to-glass and glass-to-metal welding, and waveguide writing in optical materials [4].

The main disadvantage of the USP laser ablation process for mass production is the low achievable ablation rate. Laser systems with a high ablation rate are in the order of magnitude of 1 mm^3/min. The ablation rate is low due to the small laser spot size and low average laser power [2]. Laser sources with increased pulse energies and/or higher pulse repetition rates are coming to the market [2]. The throughput of USP laser ablation could increase by increasing the laser spot size, laser fluence, or pulse repetition rate. These parameters and other influencing processing parameters have an influence on the ablation rate and resulting surface quality, therefore the parameters need to be set carefully. An increase in throughput could make the USP laser ablation process suitable for different industrial applications.

1.2 PROBLEM DEFINITION

The main problem addressed in this thesis is the low ablation rate of the USP laser ablation process. This research can be applied to all small metal parts, but to demonstrate practical applications and scope the research, cases from the company Philips are used. These cases are used to analyse and illustrate the findings of the thesis. This research is part of a bigger project at Philips aimed at the design of a testing platform to further develop a mass production USP laser ablation system. This thesis is aimed at the laser process requirements for this platform.

1.3 RESEARCH OBJECTIVES

The goal of this research is to establish knowledge and to gain insight in the dominant processing parameters determining the ablation rate, resulting surface quality, and heating of the part. To reach this goal, the following main research question is stated:

‘What processing settings can be used to create an USP laser ablation process with an ablation rate, quality, and heat input, sufficient for mass production of small metal parts of Philips?’

To answer the main question, the following sub-questions are used:

1. What processing parameters influence the ablation rate?
2. What processing parameters influence the surface quality?
3. What defines the quality of the surface after the ablation process?
4. What processing parameters influence the heat input in the part?
5. How is ablation efficiency defined?
6. How can the heat input and ablation efficiency of the ablation process be measured?
7. What is a sufficient ablation rate, quality, and heat input for the metal part?
8. What is the relationship between heat input, wavelength, and ablation efficiency?
9. What methods can be used to increase the ablation rate?
10. How is the surface quality affected by increasing the ablation rate?

1.4 REQUIREMENTS

Based on cases of Philips, requirements are listed in Table 1. The reasoning behind these requirements and a description of the part are discussed in Appendix A.

Table 1: Requirements cases of Philips.

No.	Requirement Description	Required value
1	Maximum time for production per part	< 6 s
2	Surface roughness of finished part	<Sa 0.6 µm
3	Maximum ablation volume	1.37 mm^3
4	Maximum ablation depth	20.8 µm
5	Minimum ablation rate	0.228 mm^3/s
6	Maximum tolerable material temperature	250 °C
7	Material	AISI 420 hardened steel

1.5 SCOPE OF THIS THESIS

The overall structure of this study takes the form of five chapters, including this introduction. In chapter 2, the state-of-the-art of laser ablation is presented. In this chapter, all relevant literature regarding the research objectives (Section 1.3) is summarized, and relevant sub-questions are answered. Not all sub-questions can be answered from the literature, therefore experiments were performed. In chapter 3, experimental setups and the methodology which were used for different experiments are presented. Next, in chapter 4, the results of the experiments are presented and discussed. Finally, in chapter 5, conclusions are drawn and recommendations for future work are discussed. An overview of the sub-questions and the chapter in which the sub-questions are elaborated is shown in Table 2.

Table 2: Sub-questions and the locations of their answers.

Sub-question	**Chapter**
1. What processing parameters influence ablation rate?	2,4
2. What processing parameters influence the surface quality?	2,4
3. What defines the quality of the surface after the ablation process?	2
4. What processing parameters influence the heat input in the part?	2,4
5. How is ablation efficiency defined?	2
6. How can the heat input and ablation efficiency of the ablation process be measured?	3
7. What is a sufficient ablation rate, quality, and heat input for the metal part?	1
8. What is the relation between heat input, wavelength, and ablation efficiency?	4
9. What methods can be used to increase the ablation rate?	2
10. How is the surface quality affected by increasing the ablation rate?	2

2. STATE-OF-THE-ART

This chapter summarises the relevant literature and elaborates on the first sub-questions from Section 1.3.

2.1 BASICS OF USP LASER ABLATION

The first principles of light amplification by stimulated emission of radiation date back to the early 20th century, but the first working laser was only built in 1960 [5]. After the first laser source was built, further development continued, and in 1985, a breakthrough was made on USP laser sources: chirped pulse amplification [6]. Due to this development, femtosecond (fs) and picosecond (ps) laser sources with high pulse energies, suitable of laser material processing, became available [6].

Short and ultrashort laser pulses can be used to increase the quality of the machined area in comparison to continuous-wave (CW) laser sources. This is due to fewer melt burrs and thermal damage to the material [7]. The increase in quality usually comes at the cost of a reduced ablation rate and ablation efficiency. Short laser pulses are defined as having a pulse duration in the microsecond (µs) and nanosecond (ns) ranges (10^{-6} - 10^{-9}s). Ultrashort laser pulses are in the range of ps and fs (10^{-12} - 10^{-15}s). Compared with short laser pulses, ultrashort laser pulses introduce even less thermal effects, allowing for higher precision manufacturing. In Figure 1, the differences between short and ultrashort laser pulses in laser material interaction are illustrated. For short laser pulses, classical thermal laser-matter interaction describes the material removal process. The incident laser energy heats, melts, and boils the material. The material is removed via melt expulsions, as a vapor, and as plasma. During the laser-material interaction, heat is conducted into the bulk material. The timescales of fs and ps pulses are close to the electron thermalization time of the atoms, leading to a different ablation mechanism. The electron thermalization time describes the coupling time for the heat energy of the electron gas in the material, which absorbed the photons of the laser light, to transfer to the phonons. Phonons are vibrations of the atoms in the metal matrix, which is in fact heat. For ultrashort laser pulses, the two-temperature model describes the ablation mechanism [8]. The two temperatures in this model are the temperature of the electrons and the temperature of the phonons. In the material, the photons of the laser beam are absorbed by the electrons, and their temperature increases rapidly. The energy of the electrons is transferred to the phonons (or temperature of the matrix) due to electron-phonon collisions. This transfer is not instantaneous but is described by the electron thermalization time and so the temperature of the electrons and the phonons are different. The temperature rise of the phonons should be sufficient for ablation to occur, so the laser intensity (J/cm^2) should be higher than the ablation threshold of the material. Below the ablation threshold, the material only heats without ablation occurring, whereas above the ablation threshold, the material is removed.

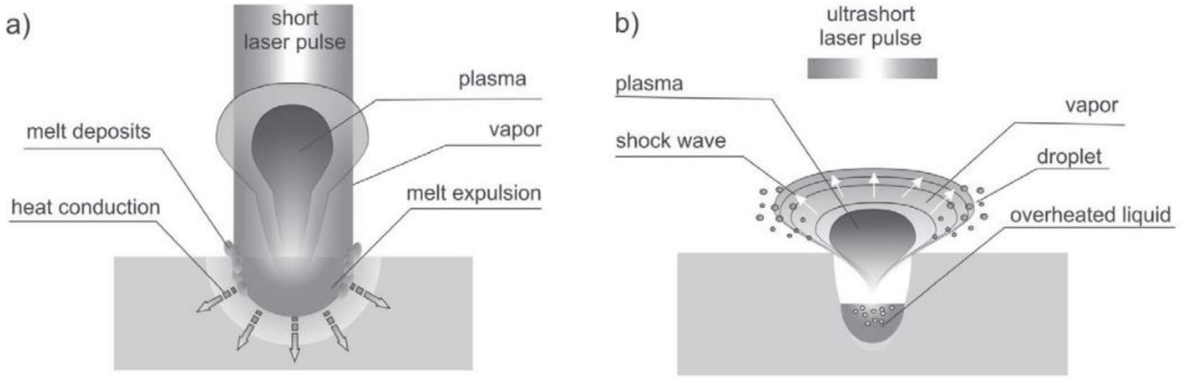

Figure 1: Laser material interaction of a) short laser pulses and b) ultrashort laser pulses. Adapted from [8].

The difference in processing quality when using µs, ns, ps, and fs laser pulses when drilling holes is shown in Figure 2. The short laser pulses of µs and ns duration show more ejected (molten) material due to the melt dominated process. The ultrashort laser pulses of ps and fs duration show only a low amount of ejected material and fewer burrs due to the different ablation mechanics [8]. Hence, ultrashort pulsed laser sources can produce higher-quality structures in comparison to short laser pulses [9].

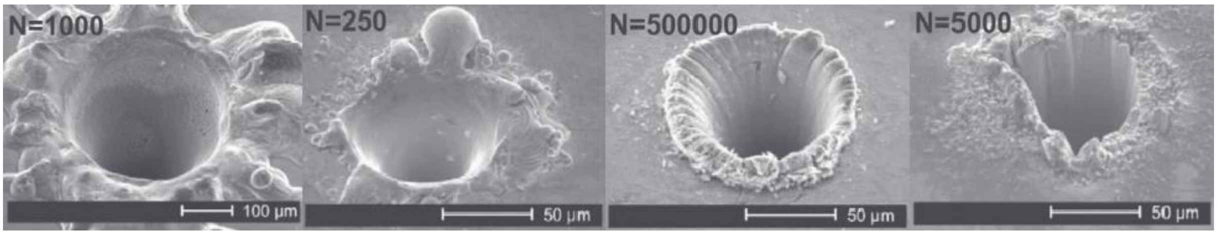

Figure 2: Quality of drilled holes for (from left to right) µs laser pulses, ns laser pulses, ps laser pulses, and fs laser pulses. Adapted from [8].

2.2 PROCESSING QUALITY

Depending on the laser settings, the resulting quality of the processed area can show different kinds of defects [10], [11]. One measure of quality is the roughness of the surface, commonly depicted as line roughness (R_a) or surface roughness (S_a) [2], [11]. Since R_a only uses a line, incidental defects in a surface can be missed. The S_a surface roughness measurement would take this incidental defect into account, but it is still an average value, and incidental defects do barely influence the resulting value. The downside of measuring quality with roughness measurements is that incidental defects are not considered. Therefore, quality cannot be well described by a roughness value. References to the quality of the surface structure in this thesis consider the requirement for R_a value, incidental defects, and holes in the microstructure.

In the milling process with short laser pulses, the ablation depth is several µm for a single pass of the laser beam over the surface of the substrate, depending on the processing settings and the material. This results in a high thickness per removed layer and thus a low Z-resolution, resulting in a staircase effect, which is unwanted for the cases of Philips (Appendix A). Brenner *et al.* [7] evaluated the use of ps laser pulses, ns laser pulses, and a combination of the two for milling pockets in AISI P20+Ni steel. The ns process showed roughness values varying between R_a 1.5 µm and 5 µm depending on the process settings. At the edges of the milled microstructures, melt protrusions were found that are 15 µm high, independent of the process settings. In their research, ps processing showed roughness values of R_a 0.6 µm without melt protrusions. This indicates that ultrashort pulsed laser ablation could be needed instead of short laser pulses to comply with the requirements for the quality of the small metal parts of Philips, see Table 1.

Some metals, for example, AISI 420, show cone-shaped defects, see Figure 3 (left), when the ablation laser fluence is low [10]. The cone shaped defects are initiated by a defect in the material, for example, inclusions of a foreign material like aluminium oxide in stainless steel due to the manufacturing process. The defect ablates at a higher laser fluence compared to the surrounding material, and when the laser fluence is not high enough, the defect does not ablate and initiates a cone shaped defect. For stainless steel, incidental cone shaped defects start to disappear around 0.4 J/cm^2 [11]. During the ablation process, the defect grows with each successive layer, and more defects can start the growth of more cones. Ling *et al.* [12] investigated these defects and concluded that deposited nanoparticles agglomerate on the surface, and these were the start of the cones. Once the cone shaped defects form, the cones do not ablate due to the low laser fluence on the slanted surfaces of the cones. Villerius *et al.* [10] further looked into these defects in AISI 301 and concluded that inclusions in the metal are the cause of the cones. The inclusions consisted of aluminium oxide, magnesium oxide, or a combination like spinel. The cones are thus referred to as Inclusion Induced Cones (IIC). The laser fluence on the surface of the cones is reduced by 35-52% due to the slanted surface, which is why the cones do not ablate as quickly and grow each layer. When the laser fluence was increased, the inclusions were also ablated, and IIC did not appear [10], [11].

On the other hand, increasing the laser fluence can result in a different quality issue. Cone Like Pillars (CLP) appear in the microstructure of stainless steels, see Figure 3 (right). CLP forms due to an increase in the surface temperature during the ablation process [13]. The formation of CLP structures depends on the laser fluence and the geometrical pulse-to-pulse overlap, and thus the scanning speed. USP laser sources can generate laser pulses with high frequency pulse repetition rates. The laser beam is scanned across the surface, and the new pulse is placed a distance next to the last pulse. For the micro-milling laser ablation process, this distance is usually less than the laser spot size, so the pulses overlap [14]. This geometrical pulse-to-pulse overlap is dependent on the pulse repetition rate and the scan speed of the laser system. Lower pulse overlaps and thus higher scanning speeds are beneficial for reducing CLP [9]. The CLP microstructure results in a higher roughness and cannot be used in the cases of Philips.

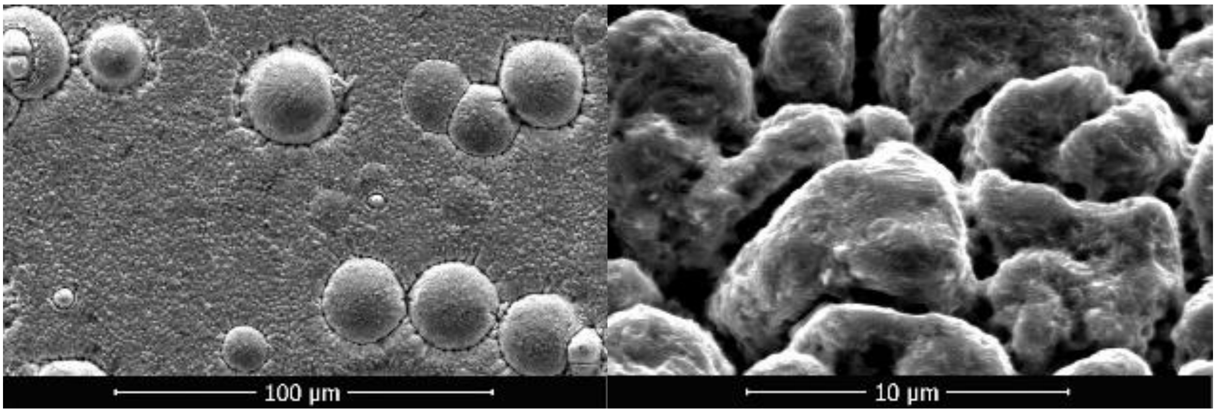

Figure 3: Scanning Electron Microscope (SEM) micrographs. Left: IIC structures typically occurring at low laser fluence ablation. Right: High laser fluence ablation shows a CLP microstructure.

2.3 RESIDUAL ENERGY COEFFICIENT AND SURFACE STRUCTURES

2.3.1 Residual Energy Coefficient

The molten phase in the USP laser ablation process is almost absent due to the short pulse duration and high laser intensity. Therefore, only a small amount of the absorbed laser energy is converted into a temperature increase in the part being processed [1]. The incident laser energy on the part is either absorbed by the part or reflected into the environment. A part of the absorbed laser energy is used for the ablation of material, and the remaining part is converted into heat energy, resulting in a temperature increase in the part being processed. Also, re-deposition of ablated material and exothermic reactions can increase the temperature of the part [15]. The formation of CLP structures and the bulk temperature of the part are dependent on the incident laser energy that is converted to heat [13]. In this thesis, the fraction of the incident laser energy that accumulates into heating of the substrate is defined as the Residual Energy Coefficient (REC) [15]–[17]. The REC is calculated as,

$$REC = \frac{\dot{Q}_{in}}{P_{av}}, \tag{2.1}$$

where $\dot{Q}_{in}$ is the laser heat energy flowing into the material and P_{av} is the average laser power. Bauer *et al.* [18] studied the REC for metals due to USP laser ablation. The spatial heat distribution of the laser pulse was found to be equal to the size and gaussian shape of the laser beam. Below the ablation threshold, where no ablation occurs, the REC is equal to the absorption coefficient [15], [16]. This is trivial because all absorbed energy is converted to heat and none to ablation. Vorobyev *et al.* [16] showed an increase in the REC for high laser fluence levels due to the redeposition of material. In a vacuum, this was not the case. Bartels *et al.* [19] presented a theoretical model for the percentage of the laser energy that is converted into heat. With increasing laser fluence, a higher percentage of the gaussian distribution is above the ablation threshold, and a lower percentage is converted into heat. Table 3 summarizes the REC values found in the literature for different materials. Only AISI 304 is a comparable material to AISI 420.

Table 3: Measured REC values found in literature.

REC	Material	Wavelength	Remarks	Reference
34 %	AISI 304	1030 nm	$F_{0,th}$ = 0.75 J/cm^2, 6 ps, P_{av} = 9.2 W, 20 kHz	[18]
31 %	Zinc	800 nm	$F_{0,th}$ = 0.45 J/cm^2, 65 fs	[15]
18 %	Copper	1064 nm	$F_{0,th}$ = 2.66 J/cm^2, 10 ps, independent of burst	[16]
23 %	Copper	1064 nm	Burst mode	[20]

2.3.2 Model/prediction of surface structures and heat accumulation

Multiple studies were conducted on the simulation and prediction of CLP structures, see Table 4. An analytical model for the prediction of the spatial temperature distribution was developed [21]. The laser-induced heat for each pulse dissipates three-dimensionally into the part [13]. As a result, the surface temperature increases due to a laser pulse and cools during the period until the next pulse, see Figure 4. After a certain number of pulses, the surface temperature just before the next pulse does not increase anymore, this is referred to as the saturated surface temperature (T_{sat}, see Figure 4). The model does not take an increase in bulk material temperature into account during the process. However, variations in the material, bulk temperature, and laser parameters such as scanning speed do result in a different T_{sat}. In Figure 4, the theoretical surface temperature is plotted for different scanning speeds. Each peak in the surface temperature is the result of a single laser pulse. Studies show that the surface temperature just before the next laser pulse is important for the formation of CLP, and this has been experimentally proven. This opens the possibility of optimizing the processing parameters to avoid CLP. A critical scanning speed is deduced for which T_{sat} stays below the critical surface temperature.

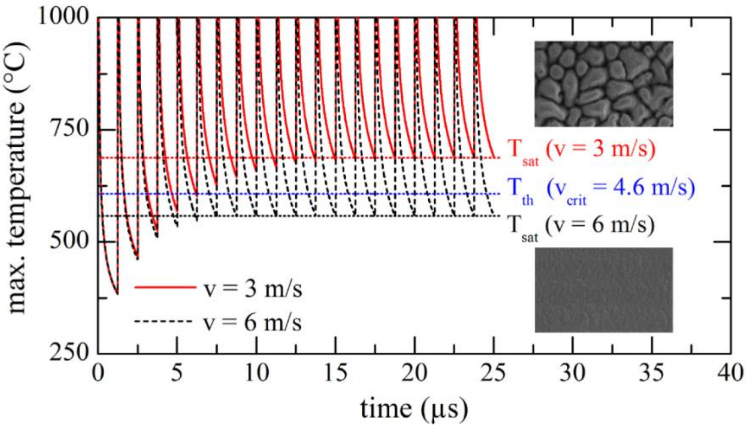

Figure 4: Surface heat prediction model maximum surface temperature as a function of time. The different lines show the temperature for different scan speeds. Adapted from [13].

Mikhaylov *et al.* [1] used the CLP prediction model to optimize the processing time of a small metal part without exceeding the critical temperature. In Figure 5, the result of their simulation is shown. The blue line shows the process duration, and the red line shows the critical pulse repetition rate. CLP structures could form at a pulse repetition rate higher than the critical pulse repetition rate because T_{sat} would be above the critical temperature. The lowest process time can be chosen, but to remain clear from the rapidly increasing left part of the blue line, an optimum laser fluence of 0.5 J/cm^2 was chosen instead of 0.2 J/cm^2. In the calculations, no cooling of the part was considered, which could further decrease the processing time.

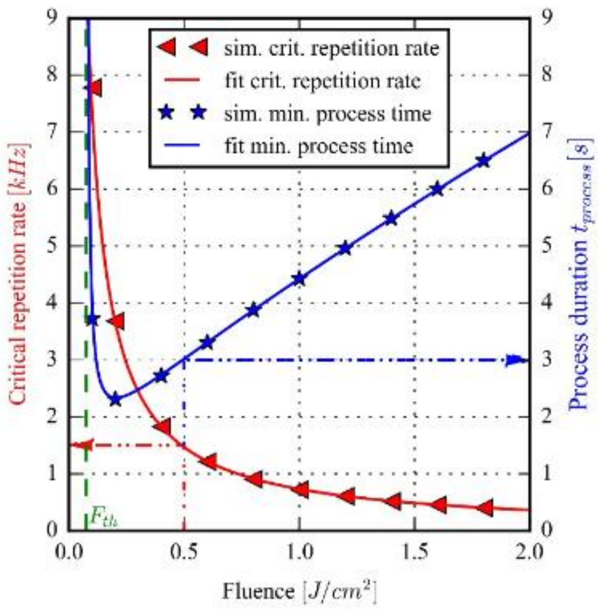

Figure 5: Results of a simulation showing the critical pulse repetition rate as a function of laser fluence in red. The blue line shows the process time when using the laser fluence and corresponding critical pulse repetition rate. Adapted from [1].

Another type of model was proposed by Rahaman *et al.* [22] using the total absorbed laser energy input into the workpiece instead of the temperature. The total absorbed laser energy model was validated for 316L stainless steel for the prediction of CLP [23]. Using the model, absorbed energy thresholds were determined, above which CLP started to form. These threshold values did vary with different pulse repetition rates and applied laser fluence levels.

Both the critical surface temperature model and the total absorbed laser energy model are not capable of precisely predicting the formation of CLP, but the models can help accelerate the optimization of the processing settings.

Table 4: Studies aimed at CLP prediction.

Author	**Model type**	**Remark**	**Reference**
Weber *et al.* (2014)	Spatial temperature distribution	Developed a spatial temperature distribution model due to multiple pulses.	[21]
Bauer *et al.* (2015)	Critical surface temperature	Developed a model for CLP prediction in steel using a critical surface temperature and the temperature distribution model of Weber *et al.* [21].	[13]
Faas *et al.* (2018)	Critical surface temperature	Developed a one-dimensional temperature model a successfully predicted CLP and roughness formation in steel.	[24]
Jaeggi *et al.* (2017)	Critical surface temperature	Successfully simulated the surface structure with the model developed by Bauer *et al.* [13].	[25]
Mikhaylov *et al.* (2018)	Critical surface temperature	Simulated the temperature in a small metal part to calculate the minimum production time without exceeding the critical surface temperature.	[1]
Rahaman *et al.* (2019)	Total absorbed laser energy input	Proposal of total energy input model for the prediction of the surface quality.	[22]
Cangueiro *et al.* (2021)	Critical surface temperature and total energy input	Simulation and experimental results of both the critical surface temperature model and total absorbed laser energy input model.	[23]

2.4 LASER ABLATION EFFICIENCY

Studies show different definitions of how fast or efficient the USP laser ablation process is [26], [27]. A highly efficient process is beneficial for mass production due to the lower average laser power that would be needed. The ablation depth per laser pulse, the ablation volume per time, and the ablation volume per time per W are used to define ablation efficiency in the literature [26], [27]. In this thesis, the ablation depth per pulse is not used as the definition of ablation efficiency because this is more relevant for laser drilling or nm precision manufacturing. The ablation volume per time in mm^3/min is used for absolute ablation rates for high power laser sources [25], [28]–[30]. The ablation efficiency in mm^3/(W·min) is used to easily compare different processing settings since it is normalized to the average laser power. The average laser power is the average power emission of the laser system over time in W. Usually this is measured after the focussing optics due to power losses in the optical components. The average laser power is calculated as,

$$P_{av} = E * f \ , \tag{2.2}$$

where P_{av} is the average laser power, E is the energy of the pulse, and f is the laser pulse repetition rate. An advantage of using this definition of ablation efficiency is that the time is linearly scalable. The average laser power also scales the process, but this is not always perfectly linear, so caution should be used when comparing widely different average laser powers. Using the amount of average laser power in the definition of ablation efficiency allows to compare the achieved efficiency with different processing settings that result in different average laser powers.

Gecys *et al.* [31] were one of the first to use a quantitative model for the ablation efficiency of USP laser ablation. Other authors also used this model, and it was found to match with the experimental results [11], [31]–[35]. Their definition of the ablation efficiency is [31]:

$$\frac{\dot{V}}{P_{av}} = \frac{1}{2} \cdot \frac{\delta}{F_0} \cdot \ln^2\left(\frac{F_0}{F_{0,th}}\right), \tag{2.3}$$

where $\dot{V}/P_{av}$ is the ablation efficiency, F_0 is the peak laser fluence of the laser beam, $F_{0,th}$ is the ablation threshold of the material in, and δ is the energy penetration depth. The energy penetration depth is the distance the laser energy penetrates the material, usually defined as the location where the laser intensity dropped to ≈37% of the initial value.

Using Equation (2.3), it is shown that the highest ablation efficiency takes place when the peak laser fluence is equal to [31],

$$F_{0,opt} = e^2 \cdot F_{0,th}, \tag{2.4}$$

where $F_{0,opt}$ is the optimal peak laser fluence to maximize the ablation efficiency and e is Euler's number.

The processing parameters such as laser fluence, laser pulse duration, wavelength, pulse repetition rate, laser spot size, and burst mode influence the ablation efficiency. In the following section, the influence of these various processing parameters on ablation efficiency are discussed.

2.4.1 Laser fluence

The peak laser fluence is calculated as,

$$F_0 = 2 \cdot \frac{E}{A}, \tag{2.5}$$

where F_0 is the peak laser fluence in J/cm^2, E is the energy in the laser pulse in J, and A is the surface area of the laser beam. For a gaussian beam, the radius is used where the intensity is dropped to 1/e^2 times the peak intensity, see Section 2.4.5. In studies, both the peak laser fluence and the average laser fluence of a gaussian beam were used. The average laser fluence is calculated using a laser spot size where the intensity is 1/e^2 times the peak intensity. The difference between the average laser fluence and peak laser fluence is a factor of two for a gaussian distribution [36]. The ablation efficiency is dependent on the laser fluence, and the ablation efficiency peaks for a certain laser fluence, see

Equations (2.3) and (2.4). In Figure 6, the measured ablation efficiency for different steels and different laser fluence levels is shown. Measurements were conducted by Lightmotif [11], a Dutch company supplying USP laser systems. All curves clearly show the optimum laser fluence for maximum ablation efficiency. In the case of the produced part at Philips, AISI 420 steel is used, which shows a peak ablation efficiency at a peak laser fluence of 0.4 J/cm^2. The hardness state of AISI 420 studied by Light motif is unknown.

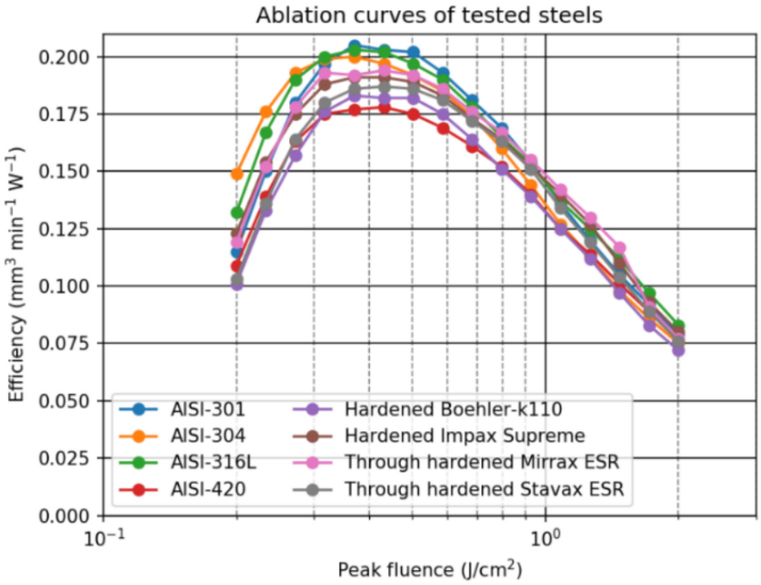

Figure 6: USP laser ablation efficiency as a function of peak laser fluence for different kind of steels. Adapted from [11].

2.4.2 Pulse duration

In USP laser ablation, the duration of the laser pulse affects the ablation efficiency. Multiple studies have shown an increase in ablation efficiency for lower pulse durations on stainless steel, see Table 5. Pulse durations shorter than 1 ps did not always show an increase in ablation efficiency. Lopez *et al.* [37] showed a peak ablation efficiency for stainless steel at 900 fs and a lower ablation efficiency at 500 fs. This decrease was only the case for a studied pulse repetition rate of 200 kHz and not for 2000 kHz. The results from the literature are shown in Table 5.

Table 5: Pulse duration and ablation efficiency on metals.

Pulse duration (ps)	Ablation efficiency (mm^3/(W·min))	Material	Wavelength (nm)	Reference
1 - 8	0.17 - 0.13	IN718	1030	[2]
10 - 50	0.15 - 0.03	AISI 304	532	[33]
0.5 - 50	0.4 - 0.05	Steel	1030	[35]
1 - 10	0.2 - 0.03	Stainless steel	1030	[37]
2 - 10	0.18 - 0.08	AISI P20+Ni	1030	[28]
0.4 - 18	0.22 - 0.1	Steel	1035	[38]
0.4 - 18	0.31 - 0.15	Steel	517	[38]
0.5 - 14	0.2 - 0.12	Steel	345	[38]
0.35 - 10	0.26 - 0.1	AISI 304	1030, 1064	[39]

2.4.3 Wavelength

The ablation efficiency depends on the wavelength of the laser beam. There was still a research gap relating the ablation efficiency to the wavelength of the laser beam for stainless steel. Hodgson *et al.* [38], [40] studied the ablation efficiency of a non-specified type of steel at three different wavelengths and at different pulse durations. The result of the study is shown in Figure 8. The results show a peak ablation efficiency of 517 nm and short pulse durations of 0.4 ps. A contributing factor in the difference in ablation efficiency could be the difference in absorptivity of the material at the different wavelengths. The reflectance of stainless steel AISI 304 at different wavelengths is shown in Figure 7. At lower wavelengths, stainless steel reflects less light and thus has a higher absorption. Schille *et al.* [41] showed comparable results for 515 nm and 1030 nm wavelengths. Most industrial high power USP laser sources have a wavelength near 1030 nm. The wavelength can be converted to different wavelengths via Second Harmonic Generation (SHG) or Third Harmonic Generation (THG), but the energetic efficiency of these devices is in the range of 50% to 30%. The energetic losses can be acceptable if, due to a much higher ablation efficiency, less laser power can be used.

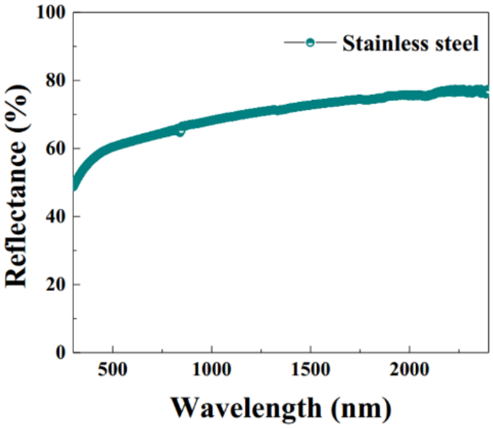

Figure 7: The reflectance of stainless steel AISI 304 as a function of wavelength. Adapted from [42].

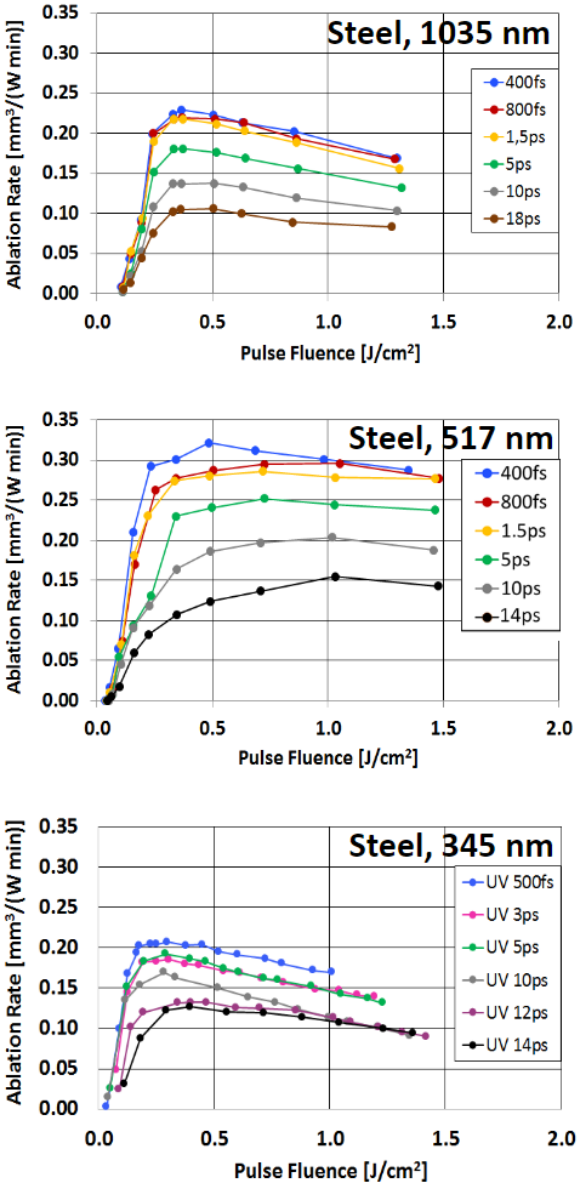

Figure 8: Ablation efficiency for steel as a function of laser fluence at different wavelengths and pulse durations. Adapted from [38].

2.4.4 Pulse repetition rate

One laser pulse only ablates a small amount of material in the order of $5\cdot10^{-8}$ mm^3, and many laser pulses are needed to remove larger volumes in the order of 1 mm^3 as required by the cases of Philips. Typical ultrashort pulsed laser sources can emit single laser pulses or a continuous pulse train of up to pulse frequencies of 40 MHz and even higher in laboratory setups [43]. The main ablation mechanics to consider when using high pulse repetition rates are plasma shielding and heat accumulation. A plasma occurs above the laser-material interaction zone after a laser pulse when the laser-induced material excitation is high, and the removed material becomes thermally ionized [44]. Plasma shielding occurs when the plasma generated by the last pulse absorbs the energy of the next pulse. This will lead to a drop in ablation efficiency because the laser energy cannot reach the surface of the substrate due to the plasma. An ablation efficiency decrease due to plasma shielding is observed at pulse frequencies of a few hundred kHz for steel, depending on the laser fluence, material, and other process parameters [45], [46]. With increased pulse repetition rates, for stainless steel >400 kHz, heat accumulation increases the ablation efficiency and can compensate for the decrease in ablation efficiency due to plasma shielding. This effect is shown in Figure 9, where the ablation efficiency decreases at 200 kHz due to plasma shielding and increases above 1000 kHz due to the increase in ablation efficiency due to heat accumulation. The heat accumulation effect is due to the fact that the surface does not have time to fully cool down before the next pulse, and the temperature of the substrate rises with each consecutive pulse, see Figure 4. Due to the higher surface temperature, the ablation threshold decreases, and the ablation efficiency increases [47]. The ablation threshold due to heat accumulation due to multiple pulses can be modelled as [47],

$$F_{0,th}(N) = F_{0,th,1} \cdot N^{s-1}\,, \tag{2.6}$$

where N is the pulse number, $F_{0,th,1}$ is the ablation threshold without heat accumulation (so due to N=1 pulses), $F_{0,th}(N)$ is the ablation threshold after N laser pulses, and s is the incubation coefficient. The incubation coefficient indicates the slope of the heat accumulation power law. For $s = 1$, incubation is absent, and the ablation threshold stays constant. A lower incubation coefficient indicates a decrease in ablation threshold with increasing number of laser pulses. The incubation coefficient for metal is typically between 0.8 and 0.9 [31].

Lopez *et al.* [37] showed an increase in ablation efficiency from 0.13 to 0.19 mm^3/(W·min) when increasing the pulse repetition rates from 200 kHz to 2 MHz. In contradiction, Kramer *et al.* [20] did not find a difference in ablation efficiency on stainless steel for repetition rates ranging from 200 kHz to 1.6 MHz. This difference might be due to other different process settings, such as the scan speed. Studies aimed at high laser power ablation showed that a higher repetition rate had a positive effect on the ablation efficiency [26]. Jaeggi *et al.* [29] showed the ablation efficiency for stainless steel for repetition rates of 50 kHz to 8.2 MHz. Their measurements are shown in Figure 9. The decrease in ablation efficiency could be due to plasma shielding. The increase in ablation efficiency for the MHz repetition rates could be due to heat accumulation.

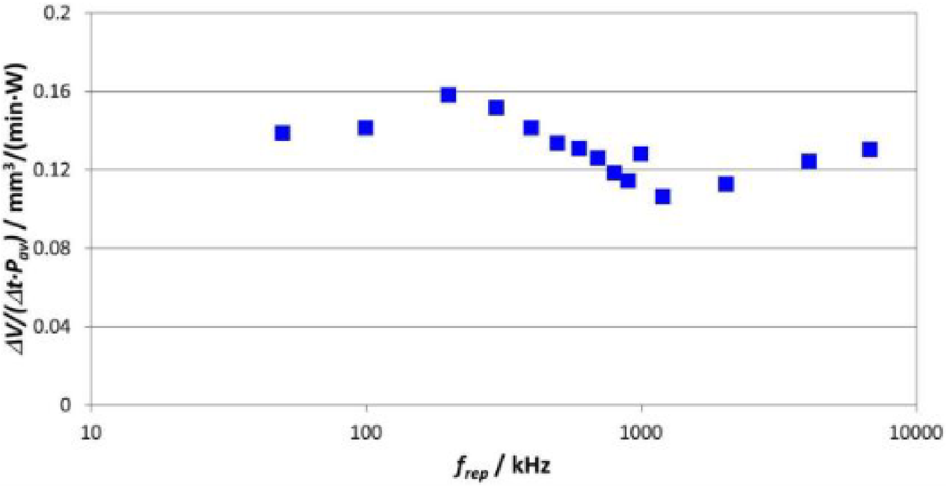

Figure 9: Ablation efficiency for stainless steel as function of laser pulse repetition rate. Adapted from [29].

The scan speed of the laser spot relative to the substrate and the pulse repetition rate defines the geometrical pulse-to-pulse overlap of laser pulses. This overlap (OL) is defined as,

$$OL = \left(1 - \frac{v}{2 \cdot w_0 \cdot f}\right) \cdot 100\%, \tag{2.7}$$

where OL is the overlap percentage, v is the velocity, w_0 is the spot radius, and f is the pulse repetition rate.

A lower scan speed and higher pulse repetition rate lead to more pulse overlap and therefore more heat accumulation. Jaeggi *et al.* [25] studied the effect of different geometrical pulse-to-pulse overlaps on ablation efficiency by changing the scan speed with a constant pulse repetition rate. The maximum ablation efficiency did not change further than the margin of measurement error when changing the geometrical pulse-to-pulse overlap between 85% and 12.5%. The resulting surface quality did change, a lower scan speeds showed CLP formation, whereas higher scan speeds showed a smooth surface, in line with the heat prediction model of Bauer *et al.* [13].

2.4.5 Laser spot size

Most USP laser sources are characterized by a gaussian beam intensity distribution. The diameter of the laser spot in a gaussian distribution can be defined in different ways. In most literature, the laser spot size is the location where the intensity is equal to $1/e^2$ times the peak laser fluence. Figure 10 shows the gaussian intensity distribution, the location where the intensity is $1/e^2$ times the peak laser fluence, and the resulting spot size 2w. This definition of the laser spot size is also used in this thesis. Care should be taken if the spot radius or spot diameter is used. The laser spot size is defined by the optical setup and can be changed by using a beam expander, a different focal length of the lens, or moving the beam out of focus.

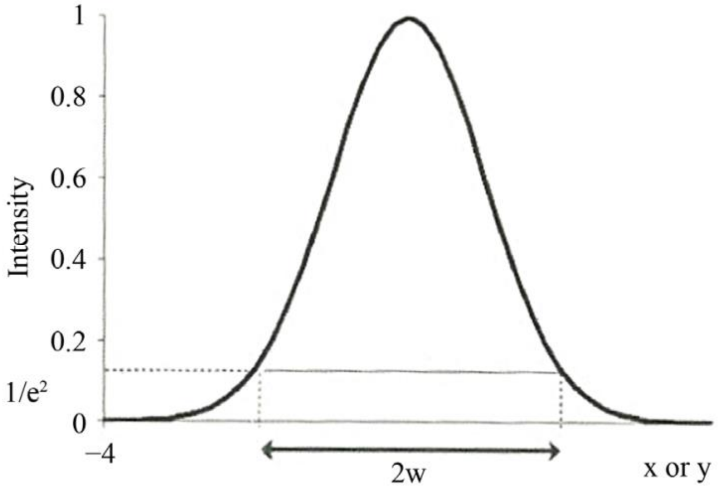

Figure 10: Gaussian intensity distribution and an indication of the laser spot size 2w resulting from the location where the intensity is equal to $1/e^2$ times the peak fluence. Adapted from [48].

Lauer *et al.* [49] measured the ablation efficiency for machining squares in AISI 304 steel and showed a decrease with increasing laser spot size. They found for spot radii of 15.5 µm, 32.4 µm, and 52.8 µm a respective removal rate of 0.13, 0.123, and 0.109 $mm^3/(W\cdot min)$. Chaja *et al.* [39] conducted experiments with spot radii ranging from 13.4 µm to 68.9 µm. They observed a 20%, almost linear, drop in ablation efficiency for the largest spot size. This effect is also observed in ns pulsed laser ablation [50], [51].

The gaussian beam can also be shaped into different intensity profiles. Neuenschwander *et al.* [32] theorised a higher ablation efficiency with the use of a top hat intensity profile. When compared to a gaussian distribution, this increase in ablation efficiency due to the top hat distribution could be due to the low intensity on the outside of the gaussian distribution, which is below the ablation threshold. Rung *et al.* [52] also theorized that the sides of the gaussian beam only contribute to heating. Experimental research conducted by Le *et al.* [53] and Chaja *et al.* [39] showed results of lower ablation efficiency with a top hat intensity profile compared to gaussian. The reason given by Chaja *et al.* [39] is a higher ablation threshold for top hat compared to gaussian ablation.

2.4.6 Burst mode

Some laser sources have the option for burst modes, which use a train of rapid consecutive laser pulses with very short inter pulse durations, instead of a single pulse. Burst mode can be beneficial for the ablation efficiency of some materials, but for steel, there are specific benefits and also downsides. The bursts are characterized by a burst pulse delay between the pulses and the number of laser pulses in the burst. The burst pulse delay/frequency range from 1 MHz (1 µs) up to 100 GHz (10 ps). The laser fluence is usually specified for the whole pulse train or per sub pulse. Burst pulse ablation shows a different mechanism when compared to single pulse ablation due to the short time between the laser pulses. Figure 11 shows the different physical mechanisms occurring in double pulse ablation (a pulse train of 2 pulses). Low burst pulse delay time (100 GHz or 10 ps) shows rarefaction wave interference. In the material, a laser induced shockwave is followed by a rarefaction wave, which is a wave through the material leading to dilution and ablation of the material. Due to the short inter-pulse duration of 10 ps, the shockwave induced by the second pulse interferes with the rarefaction wave of the first pulse, leading to a weaker rarefaction wave and a decrease in ablation efficiency. For most burst pulse delay times, a shielding of incident laser energy due to the first pulse is observed. Between certain pulse delay times (100 ps - 200 ps), material is redeposited on the sample [45]. Re-deposition of material for stainless steel ranges between 100 and 200 ps inter-pulse delay (5-10 GHz) at a peak laser fluence of 0.5 J/cm^2 [45]. Some materials show ablation efficiency dependencies for an even or odd number of laser pulses in the burst, this is not the case for stainless steels [54]. There is a differentiation between burst mode laser pulses with up to 30 laser pulses in the burst and high numbers (≫30) of laser pulses in the burst. One common reason to use burst laser pulses on steel is the increase in average laser power and ablation rate, although the maximum ablation efficiency decreases [16]. Burst laser pulses usually have a constant laser fluence per sub pulse, although the company Lumentum offers FlexBurst™ technology which makes it possible to alter the laser fluence per sub pulse [55].

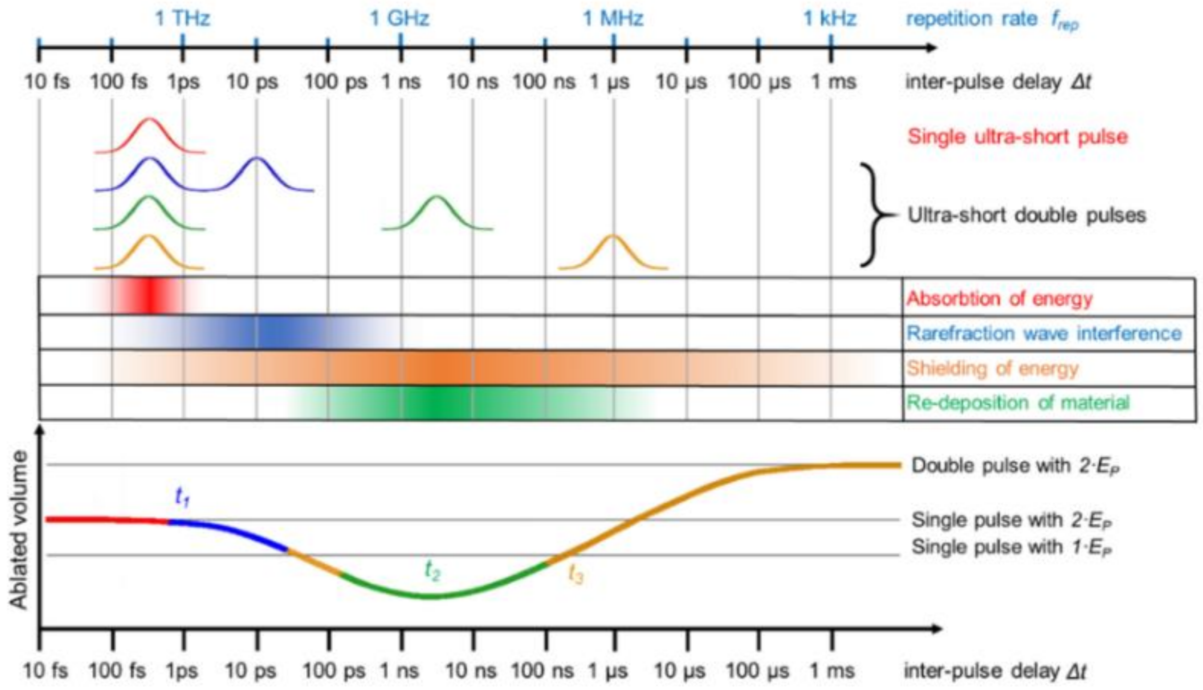

1 THz
1 GHz
1 MHz
1 kHz
repetition rate f_{rep}
10 fs
100 fs
1ps
10 ps
100 ps
1 ns
10 ns
100 ns
1 µs
10 µs
100 µs
1 ms
inter-pulse delay Δt
Single ultra-short pulse
Ultra-short double pulses
Absorbtion of energy
Rarefraction wave interference
Shielding of energy
Re-deposition of material
Ablated volume
t_1
t_2
t_3
Double pulse with $2 \cdot E_P$
Single pulse with $2 \cdot E_P$
Single pulse with $1 \cdot E_P$

Figure 11: Ablation mechanisms occurring in double pulse burst ablation as function of the inter-pulse delay time. Adapted from [45].

Studies [20], [56]–[58], as shown in Table 6, showed that when using a low number of laser pulses in the burst (maximum 30), the peak ablation efficiency is the highest when using single pulse ablation instead of bursts. At higher than optimal laser fluence levels, the ablation efficiency can be increased with these bursts. This is shown in Figure 12 [20]. So, the burst laser pulses could be beneficial for ablation efficiency with increased laser fluence. Also, burst mode can increase the surface quality. More details will be discussed in Section 2.5.2.

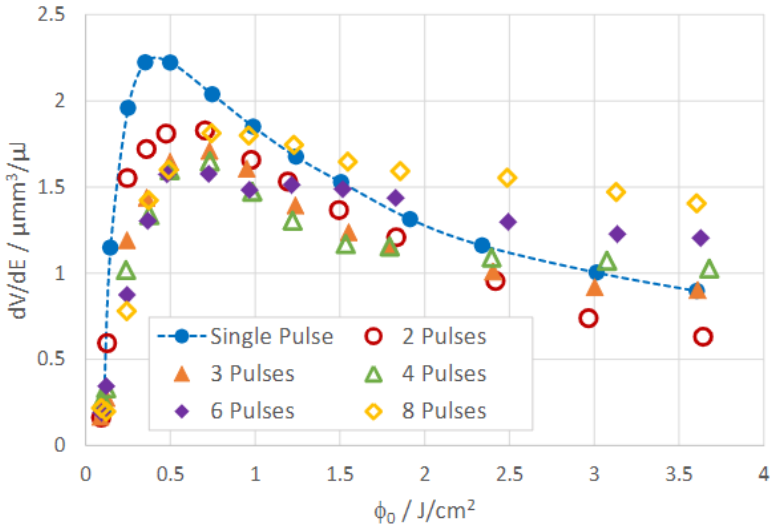

Figure 12: Ablation efficiency as a function of laser fluence. Burst pulse ablation of AISI 304 Stainless Steel with 200 kHz, 83 MHz burst frequency. Adapted from [20].

Other studies [3], [59]–[62] examined the use of a high number of pulses in the burst up to 3200, and this showed different ablation mechanics in comparison to a lower number of pulses in the burst. The laser ablation efficiency can increase using these GHz bursts for steel. Using low laser fluence pulses below the ablation threshold, a phenomenon called ablation cooling occurs, resulting in high ablation efficiency [61]. This technique is still new and not well understood. Förster *et al.* [45] even stated that the ablation cooling effect for metal processing appears highly questionable and has been partially disproven. Although the mechanism is not exactly understood, some studies have observed high ablation efficiencies.

The ablation cooling mechanism makes use of heat accumulation during the first laser pulses to lower the ablation threshold. Each pulse itself does not contain enough energy to ablate cold material, and so the ablation only starts after the first pulses in the burst have heated the surface [3], [60]–[62]. The fluence of the laser pulses in the burst should be lower than the cold ablation threshold, otherwise the ablation cooling mechanism will not occur. With too high laser fluence, the achieved ablation efficiency would be lower than single pulse ablation due to plasma shielding. Ablation cooling does not affect the bulk material temperature increase (REC), but rather is a self-sustained heating and ablation of the processed surface in the laser-material interaction zone. Typically, a minimum of 50 to 100 pulses are needed to heat the material, after which efficient ablation starts. A maximum ablation efficiency of 0.67 $mm^3/(W\cdot min)$ has been demonstrated on stainless steel for cavity milling [59]. The roughness of the resulting surface for stainless steel is above Sa 1 µm and increases with increasing ablation efficiency. The surface can be smoothed with the same laser setup; see Section 2.5.2 [59]. The GHz pulse repetition rate burst modes are in between ns laser ablation and single pulse ps ablation with respect to surface quality and ablation rate [63], [64].

Table 6: Burst mode ablation and ablation cooling literature.

Author	Burst type	Peak Ablation efficiency ($mm^3/(W\cdot min)$)	Remark/Findings	Reference
Jaeggi *et al.* (2017)	82 MHz. Up to 8 pulses.	0.16, single pulse, stainless steel.	A decrease in efficiency is observed for stainless steel and burst pulses. Fluences above 1.5 J/cm^2 are more efficient for bursts in some cases.	[56]
Kramer *et al.* (2017)	82 MHz. Up to 8 pulses.	0.14, single pulse, steel.	Similar results as Jaeggi *et al.* [56].	[20]
Hodgson *et al.* (2020)	60 - 1440 MHz. Up to 30 pulses.	Single pulse.	Using less than 5 pulses usually leads to a decrease in ablation efficiency.	[57]
Hirsiger *et al.* (2020)	5.4 GHz. Up to 25 pulses.	0.27, single pulse, steel.	Similar results as Obata *et al.* [65] are found. Theorized that there is no ablation cooling effect, but high removal rates are due to melt ejection.	[58]
Bonamis *et al.* (2020)	0.88, 1.76, 3.52 GHz. Up to 3200 pulses.	0.67, 0.88 GHz, 800 pulses, stainless steel.	High ablation efficiency is reached for high pulse numbers of 800, 1600, and 3200 pulses per burst. The quality is compared to ns pulses	[59]
E. Audouard and E. Mottay (2023)	1.76 GHz. Up to 1600 pulses.	0.3, 1.76 GHz, 1600 pulses, copper	GHz burst can be more efficient compared to single pulse ablation, but only for bursts with a long duration.	[60]
Povarnitsyn *et al.* (2018)	86.4 MHz to 3.46 GHz. Up to 200 pulses.		Simulation of multi-pulse ablation using a hydrodynamic two-temperature model.	[62]
Bonamis *et al.* (2019)	0.88, 1.76, 3.51 GHz. Up to 800 pulses.	1.4, 1.76 GHz, 200 pulses, steel.	Significant increase in ablation efficiency for drilling in the ablation cooling regime.	[3]
Kerse *et al.* (2016)	Up to 3.46 GHz. Up to 800 pulses.		Ablation cooling shows an increase in ablation efficiency for copper and silicon.	[61]
Gaudiuso *et al.* (2023)	0.67 THz. Up to 32 pulses.		Used a design of experiments to examine the influence of the main laser parameters.	[66]

2.5 HIGH TROUGHPUT USP ABLATION

High throughput is still a key factor for enabling USP laser ablation on a mass production scale [44]. Increasing the average laser can also increase the throughput, and high power USP laser sources are available today [28]. The average laser power of the laser source can be increased via the pulse repetition rate or the pulse energy, see Equations (2.2) and (2.5). For maximum ablation efficiency and quality, there is an optimum in pulse laser fluence, and so scaling the power via the pulse energy is limited to changes in the laser spot size (for more info about spot size, see Section 2.4.5) [29].

2.5.1 High throughput ablation

Different studies [2], [25], [28]–[30], [41], [59], [67], [68] demonstrated high ablation rates for stainless steels that comply with the requirements for the cases of Philips (see Section 1.4). A summary of the studies is shown in Table 7. Removal rates up to 42.42 mm^3/min were reached on stainless steel using average laser powers in the range of 300 W. All the studies used a laser beam wavelength near 1030 nm and pulse durations ranging from 310 fs to 15 ps. Both burst mode ablation as well as single pulse ablation were used, utilizing laser sources with pulse repetition rates up to 40 MHz to reach the high average power in single pulse ablation. The laser beam deflection systems used were galvo scanners [28] and polygon scanners [25]. The polygon scanner uses a rotating disk capable of reaching laser deflection speeds of the laser beam relative to the workpieces of 480 m/s. The high deflection speeds are needed to create enough geometrical pulse-to-pulse overlap to overcome surface quality issues such as those described in Sections 2.2 and 2.3. Bonamis *et al.* [59] demonstrated an ablation cooling process with a high ablation efficiency, resulting in an ablation rate of 33.5 mm^3/min for 50 W of average power. A low surface roughness was observed by Jaeggi *et al.* [29]. A roughness of $R_a < 0.2$ was demonstrated with an ablation rate of 5.2 mm^3/min.

Table 7: High throughput ablation literature.

Ablation rate (mm^3/min)	**Average laser power (W)**	**Material**	**Wavelength (nm)**	**Pulse duration (ps)**	**Remark**	**Reference**
35.3	306	AISI 304	1030	3	Single pulse 40 MHz	[25]
42.42	312	AISI P20+Ni	1030	2	Burst mode	[28]
13	-	AISI P20+Ni	1030	2		[28]
5.2	43.5	AISI 304	1064	10	$R_a < 0.2$ µm	[29]
15	90	IN718	1030	-		[2]
33.5	50	AISI 316L	1030	0.31	High efficiency ablation cooling	[59]
15	187	AISI 304	1064	10		[30]
6.8	32	Stainless steel	1030	0.35		[41]
11.5	50	Steel	1064	15		[67]
7.7	38.5	AISI 304	1030	0.8		[68]

Brenner *et al.* [28], Jaeggi *et al.* [25], and Bonamis *et al.* [59] used three different methods of increasing the ablation rate: increasing the average laser power by increasing the pulse repetition rate, increasing the average laser power by using a burst mode, and increasing the ablation rate by improving the ablation efficiency. Using a higher pulse energy is another way to increase the average laser power, but it can lead to high laser fluence levels. Studies showed a solution in which the pulse energy can be split over different beams and be used for simultaneous processing of a single part or multiple parts at once [69], [70]. The split beams can be used in multiple galvo scanners but also in a single scanner [71]. Also, a spatial light modulator can be used as an adaptive beam splitter [68], [72].

2.5.2 Post processing to improve the surface quality after USP laser ablation

A surface polishing step can be used to improve the surface quality after the USP laser ablation process. GHz (or even MHz) burst surface polishing uses the generation of a thin melt film due to heat accumulation. With GHz polishing, in comparison to MHz burst polishing, the solidified melt film shows fewer holes in the finished surface. The laser fluence should stay below the ablation threshold to avoid ablation. One of the main advantages of ultra-short polishing is the low thermal load on the bulk of the material while still creating a smooth melt film. The number of laser pulses in the burst should be high enough to create the melt film but low enough to avoid overheating, resulting in holes in the finished surface. When a lower laser fluence and a higher number of laser pulses are used, the surface quality increases. In Figure 13, a GHz polishing process on AISI 304 steel using 32 laser pulses in a burst is shown. The top of the figure shows the result of an ablation process consisting of CLP structures. The bottom shows the polished surface, decreasing the S_z by a factor of 33 [73]. Metzner *et al.* [74] show similar results with 4 pulses in a GHz burst. They improve the CLP structure of single laser pulse ablation from S_z = 16.2 µm to S_z = 1.1 µm. The S_a value is only 100 nm. Brenner *et al.* [28] showed a polishing rate up to 12.15 cm^2/min going from S_a = 0.38 µm to S_a = 0.19 µm.

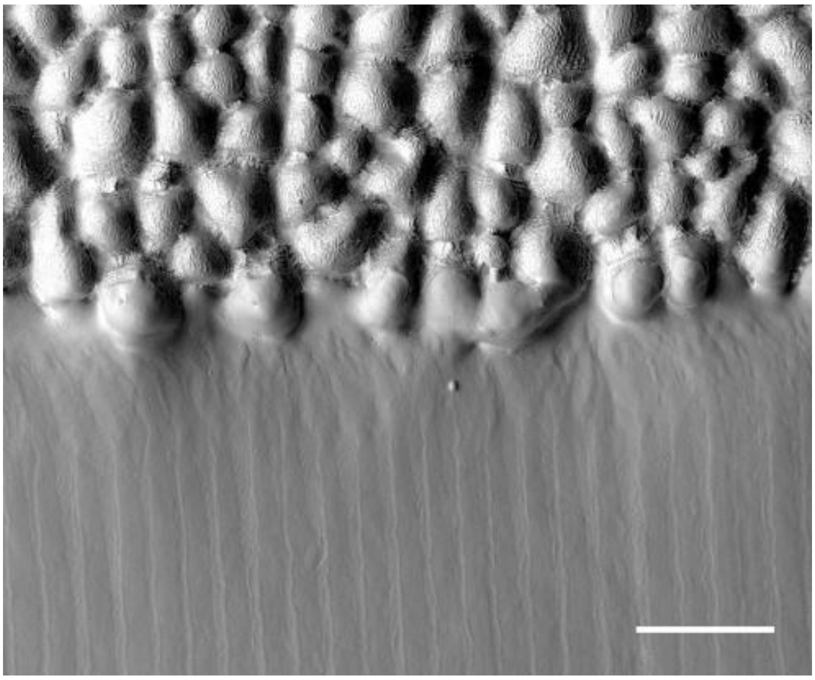

Figure 13: SEM micrograph of GHz surface polishing topological view. Scale bar is 40 µm. Adapted from [73].

2.6 SUMMARY

Extensive research has already been conducted on USP laser ablation on metals. The literature shows different processing parameters that influence the ablation rate and ablation efficiency. It was discussed in this chapter how different laser settings can result in a certain surface quality after USP laser ablation. Here the quality is defined by the roughness in R_a or S_a, inclusion induced cones, and cone like pillars. Cone like pillar formation can be predicted by a temperature or energy model. Both have shown success in accurately predicting surface quality.

The ablation efficiency in $mm^3/(W\cdot min)$ is chosen here as the definition for the ablation efficiency, but care should be taken that it does not always linearly scale with the average laser power of the laser source. Multiple different processing parameters of the laser system influence the ablation efficiency. Table 8 shows the parameters and their influence on the efficiency of the ablation process.

Table 8: Processing parameter and their influence on ablation efficiency.

Parameter	Influence on ablation efficiency
Laser fluence	An optimum laser fluence (0.4 J/cm^2) is found where the ablation efficiency peaks. Higher and lower laser fluence levels both show a decrease in ablation efficiency. This is quantitatively modelled, and the maximum ablation efficiency is theoretically reached when a laser fluence of e^2 times the ablation threshold laser fluence is used
Pulse duration	Lower pulse durations show an increase in ablation efficiency. There are differences between papers, but short laser pulses in the range of 1 ps can double the ablation efficiency in comparison to 10 ps laser pulses.
Wavelength	Different wavelength laser beams result in a different ablation efficiency. Only one source shows ablation efficiency results for a generic steel. Results show an ablation efficiency increase for 517 nm in comparison to 1035 nm. The ablation efficiency decreases again for 345 nm.
Repetition rate	The laser pulse repetition rate influences the ablation efficiency negatively via plasma shielding and positively via heat accumulation. For steel the tipping point, where the positive effects of heat accumulation overcome the negative effects of plasma shielding, is around 400 kHz to 1 MHz. The repetition rate together with the scan speed of the laser spot over the surface define the geometrical pulse-to-pulse overlap. The geometrical pulse-to-pulse overlap show little effect on the ablation efficiency but can affect the formation of CLP.
Laser spot size	Increasing the laser focal spot size decreases the ablation efficiency for gaussian and top hat intensity distributions. The ablation efficiency for gaussian is higher than the ablation efficiency for top hat.
Burst mode	Burst mode with up to 30 laser pulses usually has a negative effect on the ablation efficiency. At high laser fluence levels, burst mode can be beneficial. GHZ laser pulses in the ablation cooling regime show an increase in ablation efficiency. More research into the ablation cooling regime is still needed.

The ablation efficiency is found to not increase a lot, so to increase the ablation rate, the best option is to increase the average laser power of the laser source. This has its limitations due to the possible quality degradation of the surface after processing. The ablation cooling regime can be a usable method to increase the ablation rate and ablation efficiency, but more research is needed. There is still a research gap for the ablation efficiency of AISI 420 steel at different laser wavelengths. Also, the heat input due to changes in laser fluence and wavelength is not yet known. This is important for the cases of Philips due to the low heat capacity of the products considered. In the next chapters, this gap will be further studied.

3. EXPERIMENTAL SETUP & METHODOLOGY

In this chapter the experimental setup and the methodology of the experiments are presented. It elaborates on the laser setups and different other setups that were used in this research. Different experiments were conducted: The surface finish at different average laser powers was investigated, the relation between the wavelength, ablation efficiency, and heat accumulation was investigated, and a solution for cooling a Philips shaving head was investigated.

3.1 EXPERIMENTAL SETUP

3.1.1 Laser setups

Two different experimental laser setups were used. One setup is located at Philips in Drachten, and one is located at the University of Twente (UT). Both setups were used to conduct experiments. Due to its ease of use, availability, and higher average power, the laser setup at Philips was used. The laser setup located at the UT is equipped with a SHG and THG to convert the laser beam to different wavelengths and has the possibility to tune the pulse duration including 1 ps pulse duration, around the optimum for steel. The UT setup was used for experiments in which the wavelength is varied. Table 9 lists the specifications of the laser setups.

Table 9: Experimental laser setups.

	Philips	**UT**
System	Lightmotif OP3	Optical table
Laser source	Lumentum Picoblade 2	Light Conversion Carbide
Pulse duration	8 ps	Tuneable between 0.29 ps and 20 ps
Wavelength	532 nm	1028, 514, 343 nm
Max average laser power	25 W	6.7 W
Max repetition rate	8 MHz	2 MHz
Max pulse energy	100 µJ	111 µJ
Beam shape	TEM_{00}, $M^2<1.3$	TEM_{00}, $M^2<1.2$
Polarisation	Circular polarized	Linear polarized
Scanner	Scanlab Intelliscan 10	Scanlab Intelliscan 14
Objective	Telecentric f-theta 100 mm	Telecentric f-theta, 80 mm (1028 nm), 100 mm (514 nm), 103 mm (343 nm)
Spot diameter	20 µm	Wavelength dependent

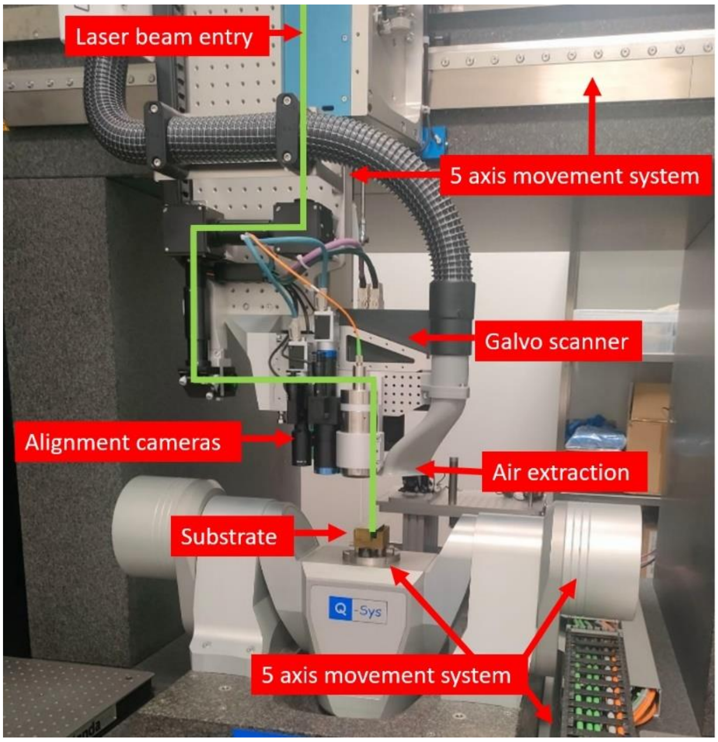

Figure 14: Laser setup located at Philips. The green line indicates the path of the laser beam.

The laser setup at Philips, as shown in Figure 14, is an advanced setup which makes use of automation. For example, the laser power is automatically calibrated, and the focus can be easily determined via the alignment cameras. The laser setup at the UT, as shown in Figure 15, is less automated in comparison to the one at Philips. The power of the attenuator can only be set as a percentage, and this is neither calibrated nor linear to the pulse energy. The pulse energy was therefore set by measuring the average laser output power after the focussing lens. This way, all losses due to optic components were considered in pulse energy measurement. Using the repetition rate of the laser source, which was set in the software of the laser source, the pulse energy can be calculated by measuring the average laser power and Equation (2.2).

The laser spot size and focus location of the laser beam relative to the surface of the substrate were not known. To determine the focus location, the sample was ablated with several lines at different Z heights of the focusing lens. Via a microscope, the lines were analysed, and the location with the smallest and deepest ablation trench was selected as the Z-location of the focusing lens. This corresponds to the location of the focus on the surface of the sample.

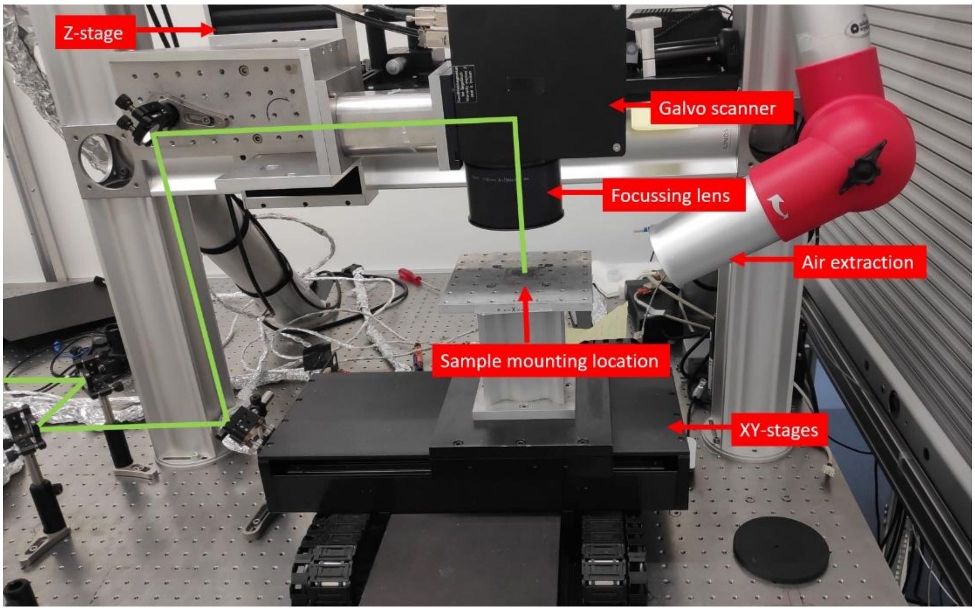

Figure 15: Laser setup located at the UT. The green line indicates the path of the laser beam.

3.1.2 Material and samples

Multiple laser ablation experiments were performed, all using the same material, but in different shapes. The used material was Sandvik 6C27 martensitic stainless chromium steel with a low carbon content (AISI 420). The elements in the material are shown in Table 10.

Table 10: Element properties of Sandvik 6C27 martensitic stainless chromium steel (AISI 420).

Element	Percentage
Carbon, C	0.32 %
Chromium, Cr	13.5 %
Iron, Fe	85.6 %
Manganese, Mn	0.30 %
Phosphorus, P	<= 0.025 %
Silicon, Si	0.20 %
Sulfur, S	<= 0.010 %

For the surface finish experiments, a hardened strip of 0.3 mm thickness was used. The experiments which study the temperature of a Philips shaving head, use the same material but shaped as a shaving head. A specific sample was created for the wavelength, ablation efficiency, and heat input experiments. The sample was designed to minimize heat losses through the fixtures due to conduction so that the temperature increase of the sample was sufficient for the measurement setup. The sample was laser assisted water cut out of 0.3 mm AISI 420 hardened stainless steel. A thermocouple was laser welded to the bottom side of the sample. Due to the low heat input power and high conductivity of the material, the temperature distribution can be assumed uniform in the sample. The location accuracy of the thermocouple is thus not critical, although on all samples it was approximately welded in the centre. The mass of the thermocouple is negligible compared to the mass of the sample. The dimensions of the sample, and the sample with a thermocouple attached to it, are shown in Figure 16.

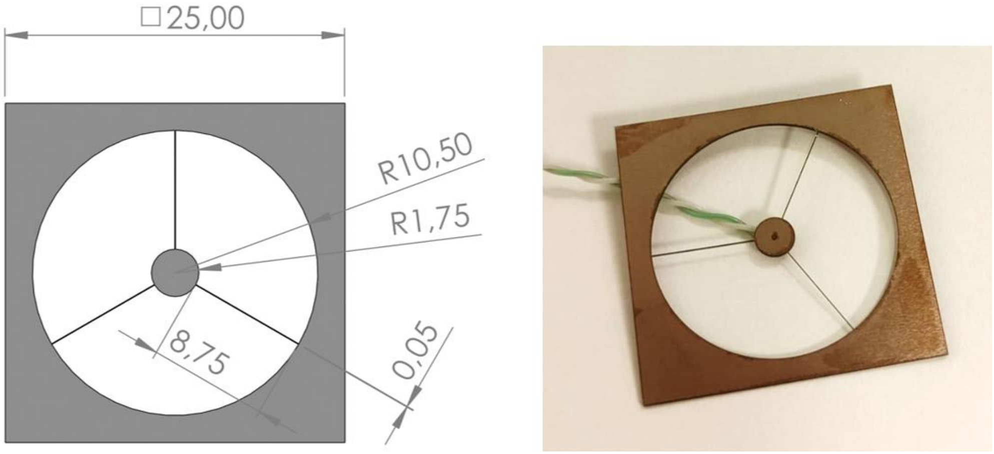

Figure 16: Sample made out of 0.3 mm AISI 420 hardened steel. Left: dimensions of the sample in mm, right: physical sample with attached thermocouple with green-white wire.

The sample was designed so that the outgoing heat flow during the experiment is minimized. By minimizing the outgoing heat flow, the heat accumulation can be calculated as precisely as possible. The mechanics contributing to the outgoing heat flow are conduction, convection, and radiation.

Convective heat flow is due to natural or forced airflow over the sample. The possibility for airflow across the sample was minimized by reducing the air volume around the sample. Below the sample a piece of PIR foam was inserted in the sample holder and on top of the sample a removable lid was placed. This is shown in Figure 18.

Conductive heat flow is the heat flow through the suspension arms of the sample. The suspension arms holding the sample were made long and thin (0.05 × 0.3 × 8.75 mm) to reduce conductive heat flow. The heat loss through the suspension arms, with a temperature difference between the sample and the sample holder of 30 °C, is calculated with the following equation:

$$Q_c = nkA_{arms}\frac{dT}{dx}\,. \tag{3.1}$$

Table 11: Definitions of variables and values for the calculation of the heat loss through the suspension arms.

Variable	Definition	Value	Unit
Q_c	Power loss due to conduction	-	W
k	Thermal conductivity	25	W/(m·K)
A_{arms}	Cross section of the arms	0.000000015	m^2
$\frac{dT}{dx}$	Temperature gradient	3428.6	K/m
n	Number of arms	3	

Using Equation (3.1) and Table 11, the heat loss due to conduction in the arms is 0.0039 W. This is 3.9% of the laser power and approximately 10% of the expected heating power. Another mechanism for heat loss is via radiation. Heat losses due to radiation are calculated via the following equation:

$$Q_r = \sigma * \epsilon * A_{radiation} * \Delta T^4. \tag{3.2}$$

Table 12: Definition and values for radiation calculation.

Variable	Definition	Value	Unit
Q_r	Heat flow due to radiation	-	W
σ	Stefan-Boltzmann constant	$5.67 \cdot 10^{-8}$	$W/(m^2 \cdot K^{-4})$
ϵ	Emissivity coefficient	1	-
$A_{radiation}$	Radiation area	$2.254 \cdot 10^{-5}$	m^2
ΔT	Temperature difference of the sample with the environment	30	K

Using Equation (3.2) and Table 12 results in a radiative heat flow of $1.035 \cdot 10^{-6}$ W. This shows that the radiation losses are several orders of magnitude lower compared to the expected heat input. Radiation losses can be neglected at the temperatures that were reached during the experiment. The emissivity coefficient of the sample is not known, so the worst case is calculated using an emissivity coefficient of 1.

3.1.3 Sample holder

As a part of this thesis, a sample holder was designed and manufactured specifically for the experiments, see Figure 17. The sample holder is multi-functional and used for the knife-edge measurement, heat input experiments, and for the experiment with heating of a shaving head. A forced air-cooling solution was designed and incorporated in the sample holder for the experiments for cooling a shaving head.

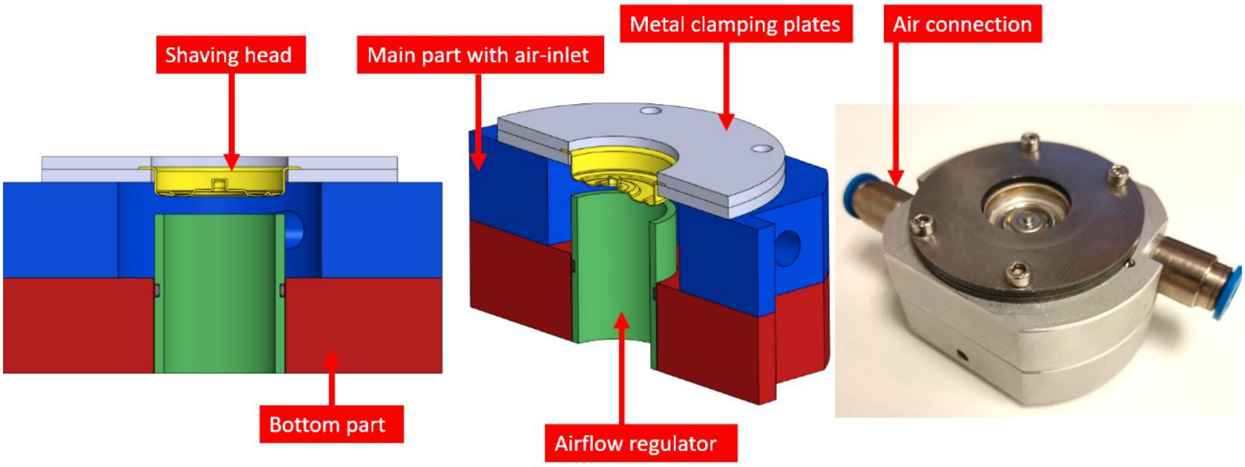

Figure 17: Sample holder with a shaving head. Colours represent different parts of the sample holder. Blue: main part with air-inlet, red: bottom part, green: airflow regulator, grey: metal clamping plates, yellow: shaving head.

All parts, directly or indirectly, attach to the blue main part with M3 bolts. The blue part incorporates two compressed air inlets for forced air-cooling of the shaving head. For tests with a shaving head, the bottom red part and green airflow regulator were used. The function of these parts is to direct the airflow across the bottom of the outer track of the yellow shaving head. The air comes in through the sides of the blue part, tangential to its inner radius. The air flows, from between the bottom of the shaving head and the green part, to the middle section. Here the air leaves the system through the bottom middle. During the heating experiments with the round suspended sample, the sample was clamped between the two grey metal plates. The red and green parts were removed, and the space in the blue part was filled with PIR foam. On top of the metal plates a lid was placed with a small opening for the laser beam to counteract the convective heat flow. The setup configurated for the heating experiments are shown in Figure 18. The lid is displayed in red, the PIR isolation foam in beige, and the sample in yellow.

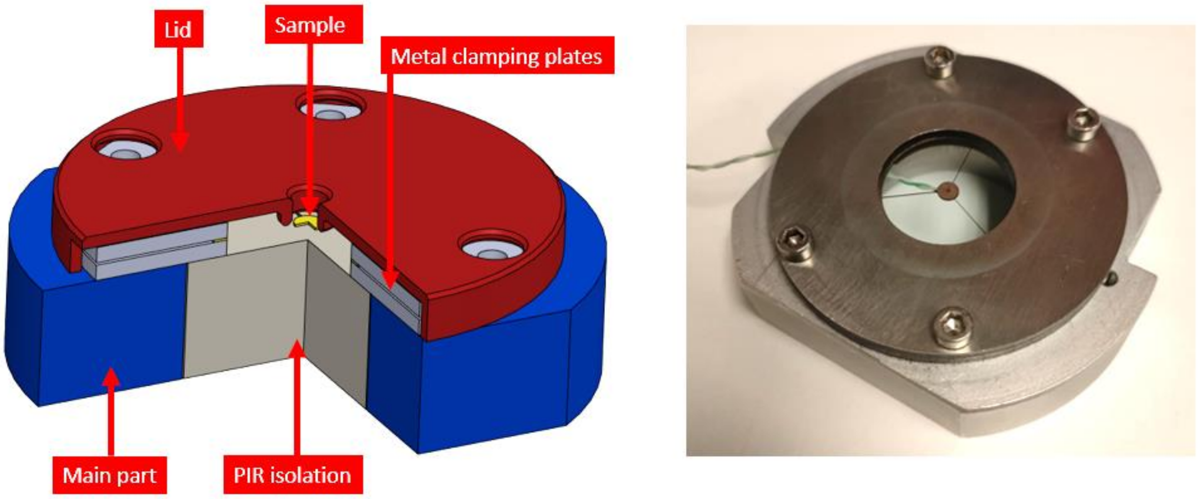

Figure 18: Sample holder sectioned view configured for heating experiments. Red: lid, beige: PIR isolation, yellow: sample. On the right: the suspended sample (without lid and PIR isolation).

3.1.4 Knife-edge setup

The laser beam spot size was not known for the laser setup at the UT. After determining the focus location, the laser spot diameter was measured via a knife-edge spot size measurement [75], see Figure 19. This method assumes a gaussian laser intensity profile, which is the case for the laser setup [76]. By moving the knife-edge, that partly blocks the laser beam, the measured power decreased following a complementary error function. The gaussian beam diameter was calculated from the fitted complementary error function. Inaccuracies due to the knife-edge measurements are elaborated in Section 3.3. The knife-edge measurement and Z focus determination were conducted with the same sample holder and material as the experiment. The knife edge is made of a 0.3 mm AISI 420 sharpened plate. Measuring in the same setup and at the same Z height made sure that there were fewer inaccuracies.

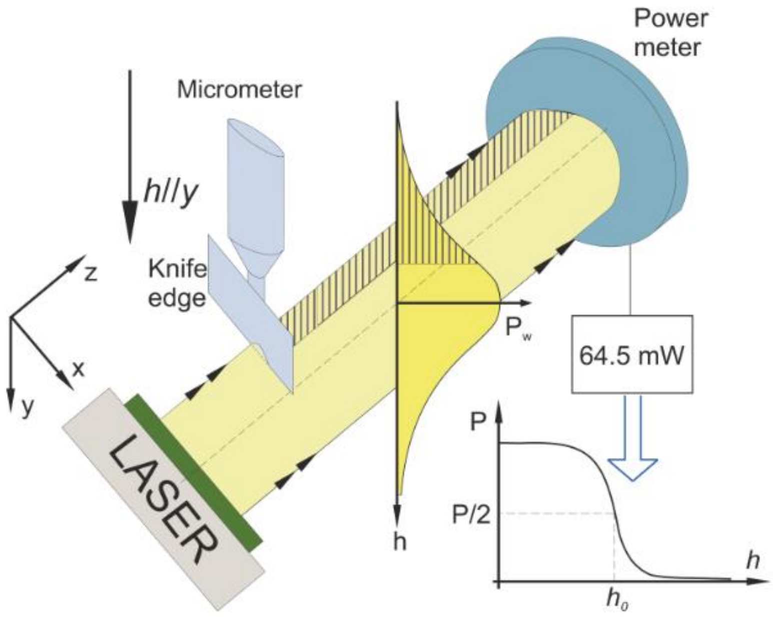

Figure 19: Principle of the knife-edge method to determine the laser beam diameter. Adapted from [75].

3.1.5 Integrating sphere

An integrating sphere was used to measure the relative absorptivity of AISI 420 samples. The integrating sphere is a sphere-shaped device that collects all light on its inside, which is reflected from a sample location. Figure 20 shows the integrating sphere setup. The measured light intensity spectrum of an AISI 420 sample was compared to the light intensity when the sphere was closed. To illuminate the sample with polychromatic light, an *Avalight-HAL-S-Mini Tungsten-Halogen light source* was used. The light was guided by an *Ocean optics QP600-VIS-BX optic fibre* to an *OZ Optics 74 series collimating lens*. In this experiment, the sample location for transmission was not used and was removed. The collimated polychromatic light bundle was directed in the *Gigahertz-Optik GmbH UPB-150-ARTA* integrating sphere, towards the sample location for reflection. The inside of the sphere is coated with *Gigahertz-Optik ODP97*, a Barium sulfate white powder with a relatively flat spectral reflectance response and diffuse reflection. The collimated light bundle was reflected at the sample location, and via diffuse reflections, the light was collected at the bottom optical fibre. Both a *QP600-VIS-BX* and *QP600-2-UV-BX* fibre were used to observe differences in measured light intensity. The reflected light intensity spectrum was measured with an *Ocean optics HR4000* spectrometer. The whole setup was placed in a dark box to prevent interference from other light sources.

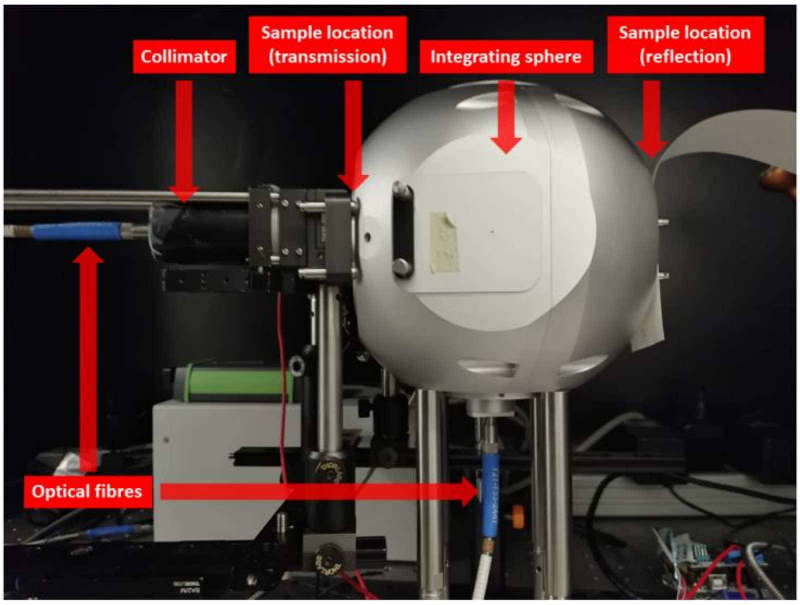

Figure 20: Integrating sphere setup for the relative reflectance measurement. Adapted from [80].

3.1.6 Analysis tools

This section shows all tools that were used for the analysis of results.

- Surface roughness values and pocket volumes were measured with an *Alicona InfiniteFocus G5* [77]. The Alicona uses Advanced Focus-Variation to create a 3D image of the surface and can calculate the surface roughness via ISO 4288. The accuracy for the measurements is estimated at 2 µm.
- A SEM was used for the analysis of the surface finish at different laser powers. The manufacturer is *FEI*, and the model is *QUANTA FEG 650*.
- A *Zeiss Axiotech 100 HD* Microscope was used to analyse the samples resulting from the ablation efficiency and heat accumulation experiments.
- Python 3.9 was used for the processing of data. The source code is included in Appendix E.
- The temperature of the sample was measured with a *RS PRO K-type 2 mm thermocouple*. An *Agilent 34970A* datalogger with *34908A* multiplexer was used to log the temperature with a timestep of 200 ms [78]. The data was further post-processed with Microsoft Excel and Python.
- The average laser power of the UT laser source was measured with a C*oherent PM10 power meter* and *FieldMax II TO* [79], [80].

An error analysis due to inaccuracies in the analysis tools is shown in Section 3.3.

3.2 METHODOLOGY

There still was a research gap in USP laser ablation for AISI 420 steel. To fill this gap, the following experiments were conducted:

- Determine the ablation efficiency with different wavelengths.
- Determine a relation between heat input and ablation efficiency.
- Gain further insight in the resulting quality of USP laser ablation relevant for the presented cases.
- Gain further insight in the heating of a shaving head and the effectiveness of forced air-cooling.

3.2.1 Sample preparation

The sample material for the surface finish experiments was cleaned with acetone as preparation. The heat accumulation experiment samples were cleaned in an ultrasonic cleaner in 40 °C demineralized water after manufacturing. Directly after, they were cleaned with acetone. Samples for the cooling of a shaving head experiment were semi-finished shaving heads. Before the experiment, the shaving heads were cleaned with acetone.

3.2.2 Knife-edge method

After the focus height was determined, the knife edge method was used to measure the laser beam diameter. The knife edge was placed just next to the laser beam, perpendicular to the X-axis, such that all laser energy was reaching the power meter. The knife edge was moved in steps of 1 µm with an *Aerotech ALS20020 series* stage. For every step, the average laser power was documented. When the measured average laser power has dropped close to zero, the beam is fully blocked. The location of the knife edge and the resulting power were analysed with a Python script (see Appendix E). A complementary error function,

$$P_{measured} = P_{offset} + 0.5 \cdot P_{av} \cdot erfc\left(\frac{(h-h_0)}{w_0/\sqrt{2}}\right), \tag{3.3}$$

was fitted where $P_{measured}$ is the measured average laser power, P_{offset} is the measured power when the laser beam is blocked, P_{av} is the average laser power before the knife-edge, $erfc$ is the complementary error function, h is the location of the knife edge, h_0 is the centre location of the laser beam, and w_0 is the beam radius. Equation (3.3) was fitted to the measured data, and the resulting complementary error curve was analysed to see if it correctly fits the data. The laser settings were chosen so that the average laser power is high enough for accurate measurements, but no laser ablation takes place. The settings are shown in Table 13 in Section 3.2.8.

3.2.3 Integrating sphere

The integrating sphere measurements were conducted in three steps. Firstly, a dark spectrum was measured. This is the measured light intensity spectrum when there is no light in the sphere. The dark spectrum was used to calibrate the setup for environmental influences. Secondly, the white spectrum was measured. In this measurement, no sample was placed, but the sphere was closed with a lid with the same coating. The white spectrum is a measurement where all light is reflected at the sample location. Lastly, the light reflection of the AISI 420 metal sample was measured. The metal sample absorbs more light at certain wavelengths in comparison to the white-coated part. This results in a lower reflected light intensity for those wavelengths. For the final result, the dark spectrum was subtracted from both the white spectrum and the metal spectrum. The relative reflection was calculated by dividing the metal spectrum by the white spectrum.

3.2.4 Surface finish at different average laser powers

The R_a roughness of the laser ablated area should be adequate for the cases of Philips. The R_a value for the cases of Philips is required to be less than 0.6 µm. Experiments were conducted with different laser powers and settings to analyse the effect on the surface roughness of 10 µm deep pockets. A pocket depth of 10 µm is comparable with the depth that is required in the cases of Philips. A hypothesis is that roughness increases with pocket depth. In a 10 µm deep pocket, the roughness might not be able to increase compared to the base material. Different average laser powers of 1 W, 10 W, and 25 W were used. The laser spot size was increased to allow higher pulse energies with a constant laser fluence of 0.5 J/cm^2 and a constant pulse repetition rate of around 1 MHz. A constant geometrical pulse-to-pulse overlap of 90% was used. Three experiments were conducted by ablating a 4x4 mm, 10 µm deep, square pocket. A total of three R_a values were measured per pocket to average and review the precision of the measurement. The OP3 laser system at Philips was used with the processing settings shown in Table 13 in Section 3.2.8. The laser spot size was varied by moving the beam out of the focus plane.

3.2.5 Ablation efficiency method

The ablation efficiency is the amount of volume divided by the amount of time it took to ablate and normalized to one W of average laser power. For measuring the ablation efficiency, a milling process was used, which can be compared to what is needed in the cases of Philips. A square pocket of 1 mm, with a depth of 20 µm was ablated. To reach this depth, the laser settings were calculated with an ablation efficiency of 0.2 mm^3/(W·min), the actual resulting depth can vary due to a different ablation efficiency. The outer dimension of 1 mm is a compromise between measurability, energy input for heating, and processing duration. The average laser power, close to the location of the sample and after the optics, was measured with a *Coherent PM10 power meter*. This average laser power was used for two different steps: setting the pulse energy when the laser was constantly on and to measure the average laser power during the ablation of the square. During ablation of the square, the average laser power during the process was lower due to the repositioning of the laser beam by the galvo scanner. The power meter was set to average the incident power over 60 s. The samples were cleaned in ethanol after the ablation process, and the resulting ablated volume was measured using an *Alicona InfiniteFocus*. The Alicona uses Advanced Focus-Variation to create a 3D image of the surface. The software can calculate the volume of the pockets. Using these values, the ablation efficiency was calculated with,

$$\frac{\dot{V}}{P_{av}} = \frac{V}{P_{av} \cdot t}, \tag{3.4}$$

where $\dot{V}/P_{av}$ is the ablation efficiency, V is the volume of the removed material as measured by the Alicona, P_{av} is the average power during the process including laser off time, t is the total time the process takes.

The laser settings were chosen so that the temperature increase as well as the ablation efficiency could be measured at different laser fluence levels. This section will explain the choices made for the wavelengths, laser fluence, pulse energy, scan speed, geometrical pulse-to-pulse overlap, repetition rate, average laser power, over scans, and hatch distance. The laser settings per experiment are shown in Table 13 in Section 3.2.8.

The studied wavelengths were chosen based on the availability of the laser setup. The Light Conversion Carbide laser has a wavelength of 1028 nm. Via a second and third harmonic generator, the light can be converted into 514 nm and 343 nm. All three wavelengths were used for the experiments to compare the results for the different wavelengths.

The peak laser fluence was varied to measure the change in ablation efficiency and heat input at different laser fluence levels. The used laser fluence values were around the expected optimum laser fluence for AISI 420 steel [11]. Peak laser fluence levels ranging from 0.2 to 4 J/cm^2 were used and were divided in 14 steps. The steps were not divided equally, more steps were located around the expected optimum laser fluence.

The lengths of the ablation lines in the square were 1 mm. Due to this short path, the speed was limited by the acceleration of the galvo scanner. Measurements for the actual acceleration of the scanner showed that a maximum scan speed of 70 mm/s can be used. Using this maximum makes sure that 90% of the ablated surface was processed with the correct scanning speed. A pulse pitch of the spot diameter divided by 100 or overlap of 99.4% is used. The pulse overlap percentage is constant for all fluence levels and wavelengths. With a change in repetition rate, the scan speed was changed accordingly.

For a fair comparison of heat input and ablation efficiency between experiments, the repetition rate is low. A low repetition rate leaves out the pulse-to-pulse interaction due, for example, plasma shielding [46]. The repetition rate is chosen so the average laser power is constant at 100 mW. The constant average laser power is beneficial for an accurate REC measurement. Not all experiments using the 343 nm wavelength could be tested due to the power limitations of the laser source.

The processing settings of the experiments were aimed at an ablated volume depth of 20 µm. This was achieved by using multiple over scans or repeats. The hatch distance was chosen so that a maximum of 8 over scans were needed to reach this depth. To achieve smooth results, a maximum hatch distance of spot diameter divided by 3 or pulse overlap of 58% was used. The hatch distance is the distance between the lines that form the square. If there is too much distance between the lines, they will form separate trenches. In some cases, the number of over scans was lowered because otherwise the hatch distance would be too large. In that case, the total amount of energy used for the pocket stays equal, but more energy per layer is deposited.

3.2.6 Heat accumulation method

The heat input measurements were conducted via a calorimetric method [18]. Due to laser radiation, the ablated sample will heat up during laser processing, and due to its temperature difference with the environment, it will also cool in general. The temperature during the laser ablation process was measured every 200 ms and logged. The temperature measurements were used to calculate the REC. The cooling heat flow of the sample was separated from the heating heat flow for the calculation of the REC. The cooling mechanisms of a body can be split up into convection, conduction, and radiation. Conduction and radiation can be neglected in this experiment, as shown in Section 3.1.2. The following equations were used for the calculation of the ingoing and outgoing heat flow and were needed for the calculation of the REC. The ingoing and outgoing heat flow are equal to

$$\dot{Q}_{in} = REC \cdot P_{av}, \tag{3.5}$$

$$\dot{Q}_{out} = H_c \cdot \Delta T, \tag{3.6}$$

where $\dot{Q}_{in}(t)$ is the ingoing heat flow, $\dot{Q}_{out}$ is the outgoing heat flow, The REC is the Residual Energy Coefficient, P_{av} is the average laser power of the laser incident on the workpiece. H_c is the heat loss constant, $\Delta T(t)$ is the temperature difference between the sample and its environment. For the REC calculation the internal energy of the sample is needed. The internal energy is equal to

$$E_{sample} = c_{av} \cdot m \cdot T_{av}, \tag{3.7}$$

where E_{sample} is the internal energy in the sample, c_{av} is the average heat capacity of AISI 420 steel, m is the mass of the sample, T_{av} is the average temperature of the sample. With the help of Equations (3.5), (3.6), and (3.7), the REC was calculated. For the calculation of the REC, $\dot{Q}_{in}(t)$ needs to be isolated, and the cooling behaviour of the sample was needed. Since radiation is negligible, it cools according to newtons law of cooling [81],

$$T = a \cdot e^{-r \cdot t} + T_{env}, \tag{3.8}$$

where T is the temperature of the sample, a represents the temperature difference with the environment at the start of the cooling cycle, r is the coefficient of heat transfer, T_{env} is the environment temperature, and t is the time. The rate of heat loss is a linear function dependent on the coefficient of heat transfer, the temperature of the sample, and the environment temperature,

$$\dot{T} = -r \cdot (T - T_{env}), \tag{3.9}$$

where $\dot{T}$ is the temperature flow. The linear function from Equation (3.9) was fitted to the measured cooling data using a least squares fit. The deviation of the linear fit with the measured data was analysed. The cooling rate, dependent on the temperature of the sample, is shown in Appendix D. This calculated temperature flow due to heat loss was added to the measured data from the heating period so that the temperature during heating is compensated. This resulted in a theoretical temperature during the heating period, with the cooling compensated. The slope of the fitted linear increase in temperature is a measure for $\dot{Q}_{in}$. The heating curve, heating curve without cooling, and fitted linear heating are shown in Appendix D.

3.2.7 Cooling of a shaving head

Small metal parts, such as shaving heads, only have a low heat capacity. Increasing the laser power will also increase the heat load on the part. The temperature of a shaving head was measured during ablation of a donut shaped area, as can be seen in case 2 in Appendix A. The sample holder, as shown in Figure 17, was used to actively air cool the shaving head. The results of the experiment show the capabilities of forced air-cooling, which can be used to enable higher laser powers.

Two K-type thermocouples were used to measure the temperature of the shaving head during the laser ablation process. The thermocouples were welded to the shaving head at the red positions, as seen in Figure 21. The inner thermocouple was placed at the left position and the outer on the right position. Material was removed on the inside of the shaving head at the outer groove, displayed as a red surface in the blue oval.

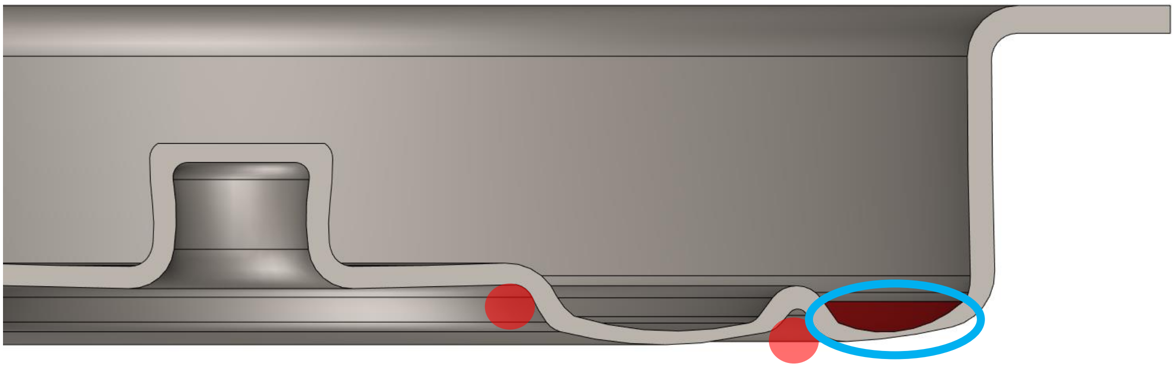

Figure 21: Cross section of a shaving head. The red circles indicate the locations of thermocouples. The blue oval indicates the location of the outer groove that is processed.

The laser settings that were used for the experiment were the same as in experiment 3 for the surface finish experiments, as shown in Section 3.2.8. The total duration of the process was 65 s. Due to skywriting, the laser was on for 46 seconds, resulting in an average laser power of $46/65 \cdot 25 = 17.7$ W. In the first experiment, no force cooling was used. During the second experiment, compressed air was used in the sample holder, as seen in Figure 17, to actively cool the shaving head.

3.2.8 Laser settings

In this section all laser settings are summarized in Table 13. The spot size of the UT laser setup was determined via the knife-edge spot size measurements.

Table 13: Laser process settings for all experiments.

Exp no.	Spot size (μm)	Wavelength (nm)	Peak fluence (J/cm^2)	Average laser power (W)	Repetition rate (kHz)	Pulse distance (μm)	Hatch distance (μm)	Scanning speed (mm/s)	Over scans
Surface finish experiments (Philips laser setup):									
1	20	532	0.5	1	1261	2	4	2530	20
2	80	532	0.5	10	788	8	16	6300	20
3	112	532	0.5	25	1012	7.5	22.4	7540	20
Heat accumulation and ablation efficiency experiments (UT laser setup):									
1	28.4	1028	0.2	Constant 0.1	158.1	0.284	2.97	44.9	8
2	28.4	1028	0.25		126.5	0.284	3.71	35.9	8
3	28.4	1028	0.3		105.4	0.284	4.46	29.9	8
4	28.4	1028	0.35		90.3	0.284	5.20	25.6	8
5	28.4	1028	0.4		79.0	0.284	5.94	22.4	8
6	28.4	1028	0.5		63.2	0.284	7.43	18.0	8
7	28.4	1028	0.6		52.7	0.284	8.92	15.0	8
8	28.4	1028	0.8		39.5	0.284	8.92	11.2	6
9	28.4	1028	1		31.6	0.284	9.29	9.0	5
10	28.4	1028	1.5		21.1	0.284	8.36	6.0	3
11	28.4	1028	2		15.8	0.284	7.43	4.5	2
12	28.4	1028	2.5		12.7	0.284	9.29	3.6	2
13	28.4	1028	3		10.5	0.284	5.57	3.0	1
14	28.4	1028	4		7.9	0.284	7.43	2.2	1
15	19.9	514	0.2		322.9	0.199	2.08	64.1	8
16	19.9	514	0.25		258.3	0.199	2.60	51.3	8
17	19.9	514	0.3		215.2	0.199	3.12	42.7	8
18	19.9	514	0.35		184.5	0.199	3.64	36.6	8
19	19.9	514	0.4		161.4	0.199	4.16	32.1	8
20	19.9	514	0.5		129.1	0.199	5.20	25.6	8
21	19.9	514	0.6		107.6	0.199	6.24	21.4	8
22	19.9	514	0.8		80.7	0.199	6.24	16.0	6
23	19.9	514	1		64.6	0.199	6.50	12.8	5
24	19.9	514	1.5		43.0	0.199	5.85	8.6	3
25	19.9	514	2		32.3	0.199	5.20	6.4	2
26	19.9	514	2.5		25.8	0.199	6.50	5.1	2
27	19.9	514	3		31.5	0.199	3.90	4.3	1
28	19.9	514	4		16.1	0.199	5.20	3.2	1
29	25.9	343	0.35		108.5	0.259	4.75	28.1	8
30	25.9	343	0.4		94.9	0.259	5.42	24.6	8
31	25.9	343	0.5		75.9	0.259	6.78	19.7	8
32	25.9	343	0.6		63.3	0.259	8.14	16.4	8
33	25.9	343	1		38.0	0.259	8.48	9.8	5
Knife edge method laser settings (UT laser setup):									
1	28.4	1028	0.02	62.7	1000	-	-	-	-
2	19.9	514	0.04	61.4	1000	-	-	-	-
3	25.9	343	0.01	31.5	1000	-	-	-	-

3.3 VALIDITY/ERROR ANALYSIS

Measurements are never perfect and show deviations from reality. For each origin of inaccuracies, the effect on the result was analysed. In the final results, this is shown in the graphs as error bars. Table 14 shows the results of the analysis and the expected accuracy.

Laser fluence was the parameter most affected by inaccuracies. It was not possible to determine the exact focus with the Z focus scan, but the focus was determined within the theoretical Rayleigh length. The laser spot size was measured after determining the focus. Not using the exact focus location of the laser beam does not result in laser fluence inaccuracies because the laser spot size was measured in the same setup after the Z-scan. The knife-edge measurements show a good similarity between the fitted error curve and the measured data. A 5% error in the measured beam radius is estimated. The knife-edge measurement was conducted in a single direction. Astigmatism in the beam could result in a different radius in the other direction due to ellipticity. In previous measurements, the ellipticity in the 343 nm beam had a maximum of 0.8 around the focus location. In the worst-case scenario, the minimum or maximum radius was measured. The area of an ellipse is $A = \pi \cdot a \cdot b$, where A is the surface area and a and b are the minimum and maximum radii. The maximum error in laser fluence due to the ellipticity in the beam is thus estimated at 20%. The pulse energy was measured with a power meter, which, according to the datasheet, has a 1% calibration uncertainty. This results in a 1% deviation for the pulse energy and laser fluence. The sample was supported by three small suspension arms. A thermocouple was attached to the sample, and this can exert a force on the sample, leading to inaccuracies in the Z-height. It is estimated that the sample can move 0.05 mm out of focus due to the force of the thermocouple, and in that case, the laser spot size can deviate by up to 5%. The total uncertainty in laser fluence due to measurement and positional errors is estimated to be: $(20 \cdot 1.05) + 1 + 5 = 27\%$. The highest contribution of the deviation is mostly due to the beam size measurement error and is consistent within a wavelength.

The ablation efficiency was calculated based on the volume of the ablated pockets. The pocket depths were measured with 2 µm precision. The precision is dependent on the depth of the pocket and, thus, also on the achieved ablation efficiency. An ablation efficiency of 0.2 mm^3/(W·min) will result in 20 µm deep pockets and 5% uncertainty in volume measurement. The power was set within 1% error. The inaccuracy in ablation efficiency is estimated to be equal to $2/(\text{ablation efficiency}) + 1\%$.

The REC was calculated using the average laser power during the process and the temperature of the sample. The average laser power was set within 1% error. The temperature measurements are estimated to result in an uncertainty of ±0.04 on the REC.

Table 14: Uncertainty in results for the wavelength, ablation efficiency, and heat input experiment.

Parameter	**Uncertainty**	**Remark**
Laser fluence	$(20 \cdot 1.05) + 1 + 5 = 27\%$	21% is constant within a wavelength
Ablation efficiency	$\frac{2}{\text{ablation efficiency}} + 1\%$	
REC	± 0.04	

4. RESULTS

In this chapter the results of the experiments are presented and discussed. The chapter consists of a section for each experiment including a discussion.

4.1 KNIFE-EDGE SPOT SIZE MEASUREMENT

Figure 22, Figure 23, and Figure 24 show the measurements for the laser spot diameter of the laser setup at the UT. The measured spot diameter was 28.4 µm for 1028 nm wavelength, 19.9 µm for 514 nm wavelength, and 25.9 µm for 343 nm wavelength. The first two wavelengths show good similarity with the theoretical complementary error curve, whereas the 343 nm wavelength shows more deviation, especially at lower average laser powers. An estimated error in the spot diameter is 5%, as can be seen in Section 3.3. The spot diameter results were used in further experiments with the UT laser setup.

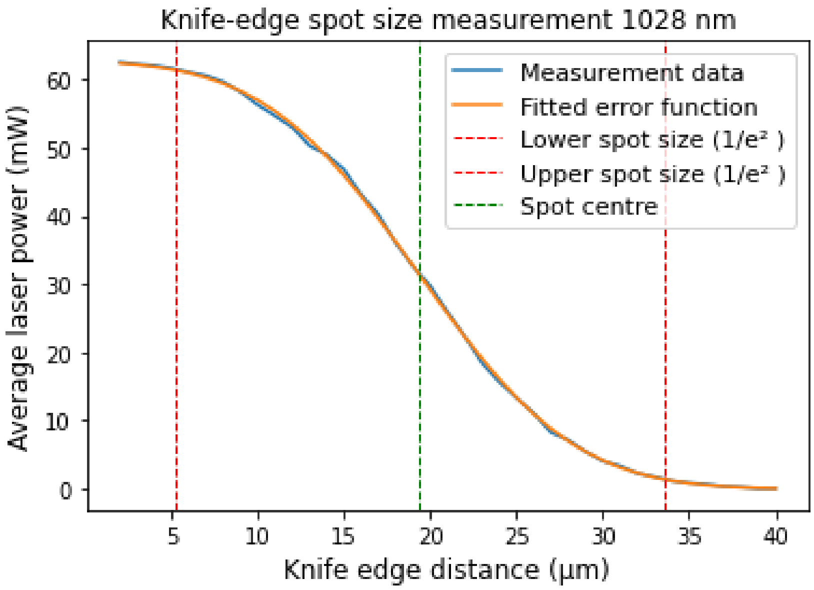

Figure 22: Measured power as function of the location of the knife edge. Spot diameter measurement for 1028 nm wavelength. Spot diameter 28.4 ± 1.4 µm.

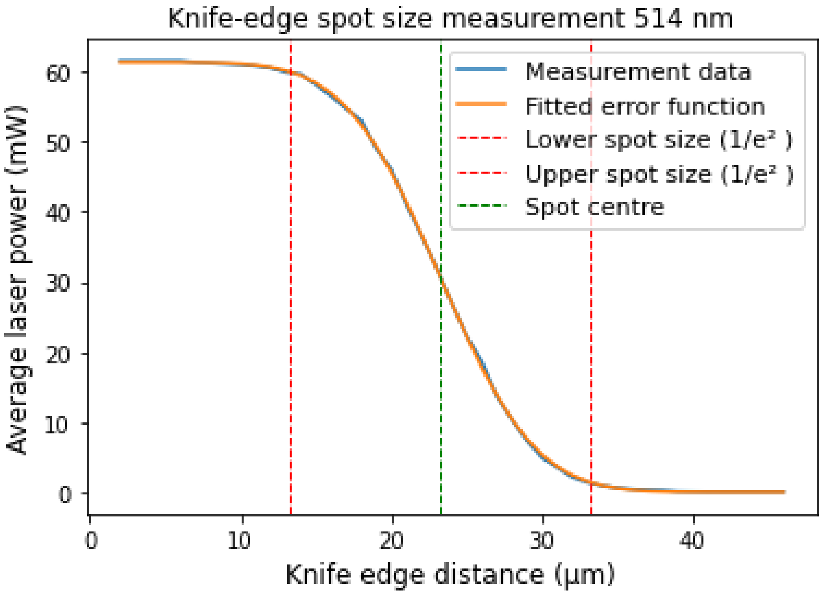

Figure 23: Measured power as function of the location of the knife edge. Spot diameter measurement for 514 nm wavelength. Spot diameter 19.9 ± 1 µm.

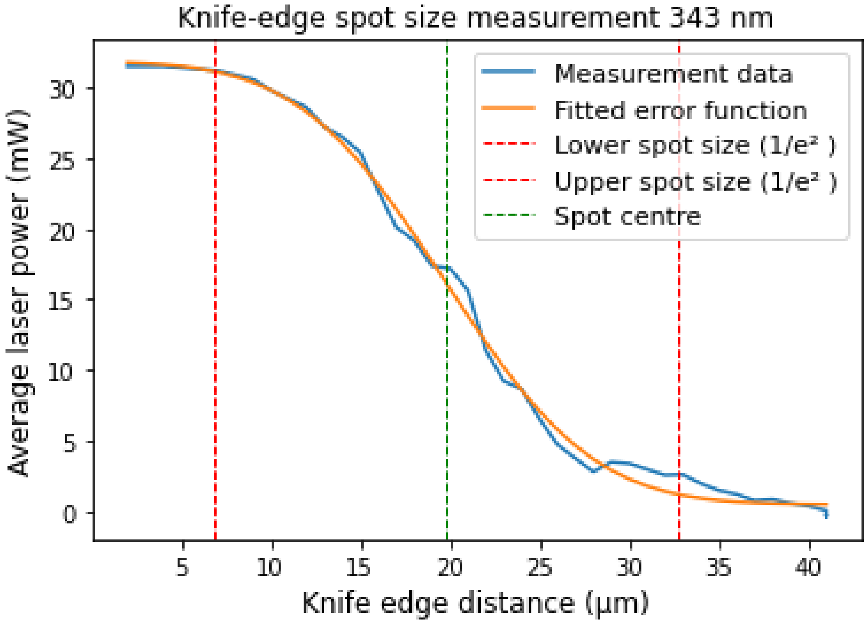

Figure 24: Measured power as function of the location of the knife edge. Spot diameter measurement for 343 nm wavelength. Spot diameter 25.9 ± 1.3 µm.

4.2 SURFACE FINISH AT DIFFERENT LASER POWERS.

SEM micrographs of the base material and of the resulting pockets with different processing settings are shown in Figure 25. Table 15 shows the measured R_a values of the resulting surfaces. All three USP laser-ablated surfaces show similar resulting surface structures, independent of the average laser power (1 W, 10 W, 25 W). The base material has the highest R_a value but is already well within the requirements. All experiments show similar improvements in surface roughness. The low roughness values might be due to the low pocket depth, where roughness cannot yet form. The results of this experiment show that the roughness due to high laser powers might only appear in deeper pockets. This could be beneficial for the cases of Philips since they use a similar ablation depth.

Table 15: R_a values of the experiments.

Experiment	R_a average (µm)
Base	0.353 ± 0.08
1	0.283 ± 0.1
2	0.286 ± 0.1
3	0.277 ± 0.1

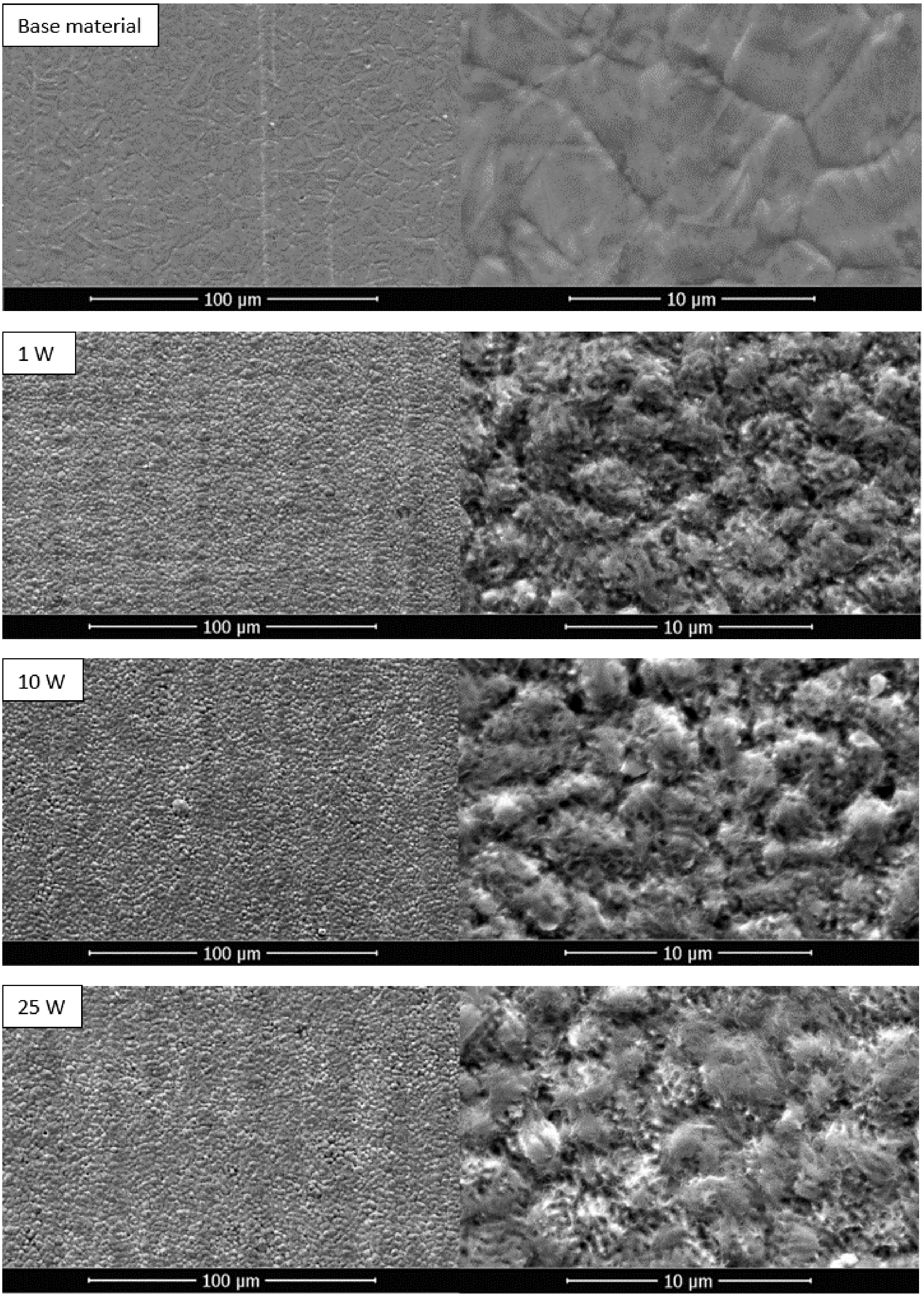
Base material
100 µm
10 µm
1 W
100 µm
10 µm
10 W
100 µm
10 µm
25 W
100 µm
10 µm

Figure 25: SEM micrographs of the base material and resulting 10 µm pockets with different process settings (1W, 10 W, 25 W). Left: 600x magnification, right: 5000x magnification.

4.3 INTERGRATING SPHERE

Figure 26 shows the measured spectra for the integrating sphere measurements. Figure 27 shows the processed data where the dark spectrum is subtracted from the white and metal spectrums, and the metal spectrum is divided by the white spectrum. The data above 900 nm and below 500 nm shows a high noise level due to the low light intensity in these wavelength regions. Three measurements were conducted: two equal measurements and one using the visible fibre. The results between 900 nm and 500 nm are similar for each measurement. The trend shows that, at a lower wavelength, less light is reflected. This would mean that AISI 420 absorbs more light at lower wavelengths. The results are similar to the observations of Jyothi *et al.* [42] for AISI 304 stainless steel, see Figure 7. The results could mean that the ablation efficiency for 514 nm is higher due to more absorption of the laser beam. This is consistent with the results of Hodgson *et al.* [38], [40] and the results in this thesis.

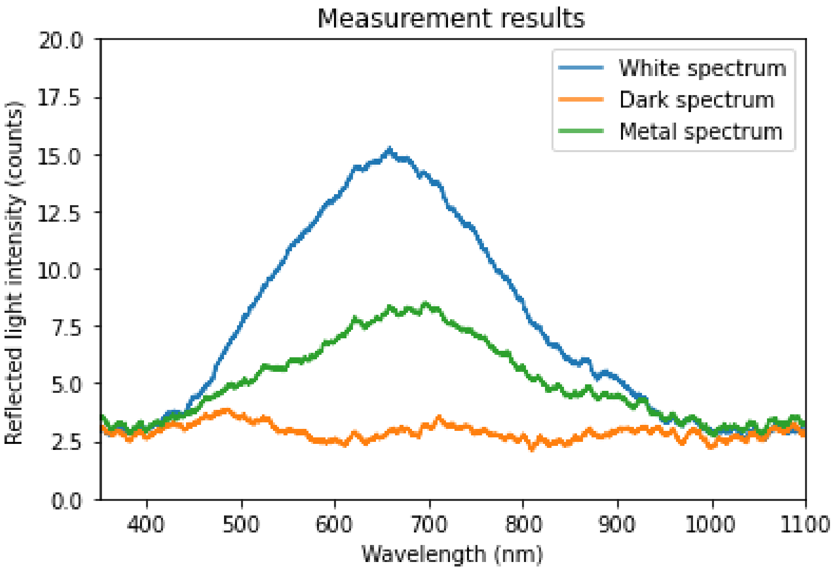

Figure 26: Reflected light spectra for the integrating sphere measurements.

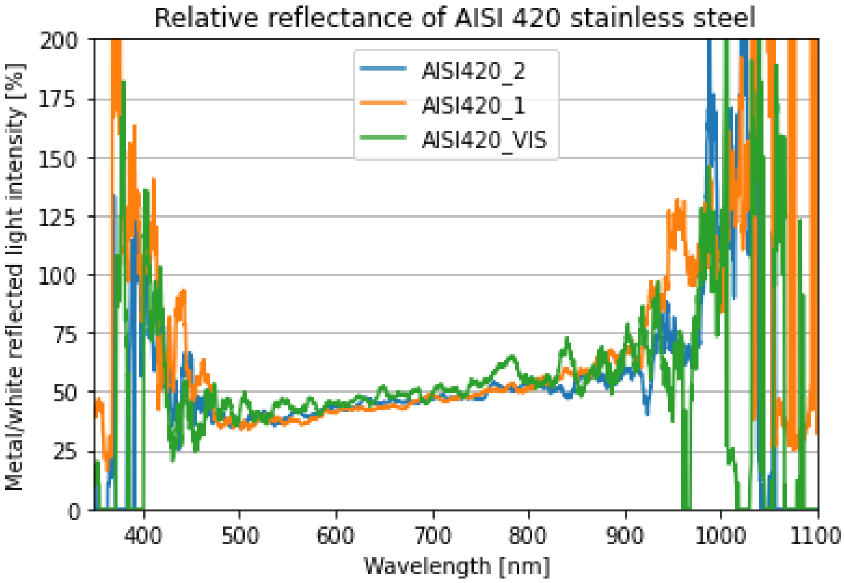

Figure 27: Relative reflection of AISI 420 compared to a white reference measurement as a function of wavelength. For two equal measurements with a UV optimized fibre and one measurement with a fibre optimized for visible light.

4.4 ABLATION EFFICIENCY

The dependence of the ablation efficiency on the laser fluence was assessed for three different wavelengths: 1028 nm, 514 nm, and 343 nm. The efficiency was calculated with Equation (3.4), and the numerical results are shown in Appendix B. Different laser fluence levels were used, but a constant average laser power of 0.1 W was maintained. The results of the experiments are plotted with laser fluence on the horizontal axis and the REC and ablation efficiency on the vertical axis. The theoretical model of Equation (2.3) was fitted via a least squares fit to the ablation efficiency data to compare the measured data with the theoretical model. Figure 28 shows the results for all wavelengths.

The ablation efficiency results for 1028 nm show a good fit with the theoretical model. The fit of the model results in an energy penetration depth of 16.2 nm and an ablation threshold of 0.12 J/cm^2. The maximum ablation efficiency was measured at 0.227 mm^3/(W·min) at 0.8 J/cm^2. The fit of the theoretical model and Equation (2.4) results in a peak ablation efficiency of 0.89 J/cm^2 with a corresponding maximum ablation efficiency of 0.219 mm^3/(W·min).

The results for the 514 nm wavelength are also consistent with the theoretical model. The peak ablation efficiency at this wavelength is higher compared to 1028 nm. The peak ablation efficiency is 0.259 mm^3/(W·min) at a laser fluence of 0.6 J/cm^2. The theoretical model was fitted, resulting in an energy penetration depth of 14.8 nm and an ablation threshold of 0.094 J/cm^2. Equation (2.4) results in a peak ablation efficiency of 0.256 mm^3/(W·min) at a peak laser fluence of 0.695 J/cm^2.

Not all laser fluence levels could be studied for the 343 nm wavelength due to high third harmonic conversion losses in the carbide laser. The theoretical model could not be fitted due to the few data points. The highest measured ablation efficiency was 0.259 mm3/(W·min) at 0.4 J/cm2.

Table 16 shows a summary of the ablation efficiencies for different wavelengths. The measured efficiencies, energy penetration depth, and ablation threshold are in line with the values seen in the literature [11], [82]. As expected, the highest ablation efficiency was reached at the 514 nm wavelength. The ablation efficiency for 1028 nm is 12% lower compared to 514 nm. Converting 1028 nm to 514 nm via a SHG would not be beneficial for the ablation rate if the losses in the SHG are higher than 12%. Results from the literature review showed that laser sources with a wavelength around 1030 nm are mostly used to reach the highest ablation rates. The experiments conducted with the 343 nm wavelength showed no increase in ablation efficiency compared to 514 nm, but the dataset is not complete. The conversion losses in a THG can make the use of 343 nm less viable.

The peak ablation efficiencies at 1028 nm and 514 nm were reached at higher laser fluence levels in comparison to most literature. Inaccuracies in laser spot size measurement and average laser power measurements could introduce these differences. Also, different processing settings were used. This shows that when a process is created, the optimum laser fluence for peak ablation efficiency for that process needs to be researched.

Figure 29, Figure 30, and Figure 31 show micrographs of the resulting surfaces of the samples. The top images show microscope images, and the bottom images show a heightmap created by the Alicona measurements. Low fluence levels show IIC and higher fluence levels tend to show a darker surface, which can indicate CLP formation.

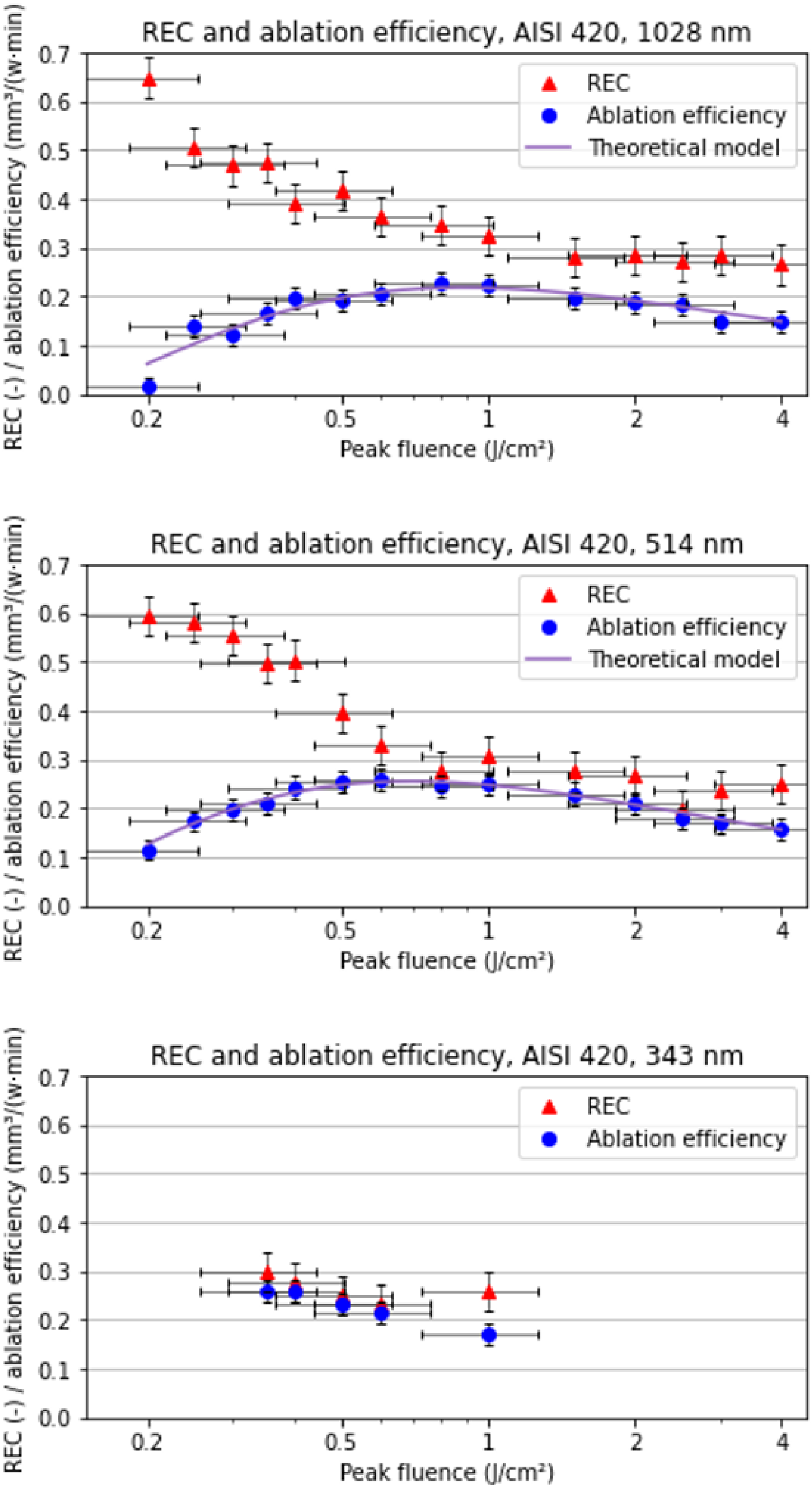

Figure 28: The ablation efficiency and the REC on AISI 420 stainless steel as a function of laser fluence. Wavelengths 1028 nm,514 nm, and 343 nm.

Table 16: Summary of ablation efficiency measurements for different wavelengths.

Wavelength (nm)	Max ablation efficiency (mm^3/(W·min))	Peak laser fluence (J/cm^2)	Modelled Ablation threshold (J/cm^2)	Modelled Energy penetration depth (nm)
1028	0.227	0.8	0.12	16.2
514	0.259	0.6	0.094	14.8
343	0.259	0.4	-	-

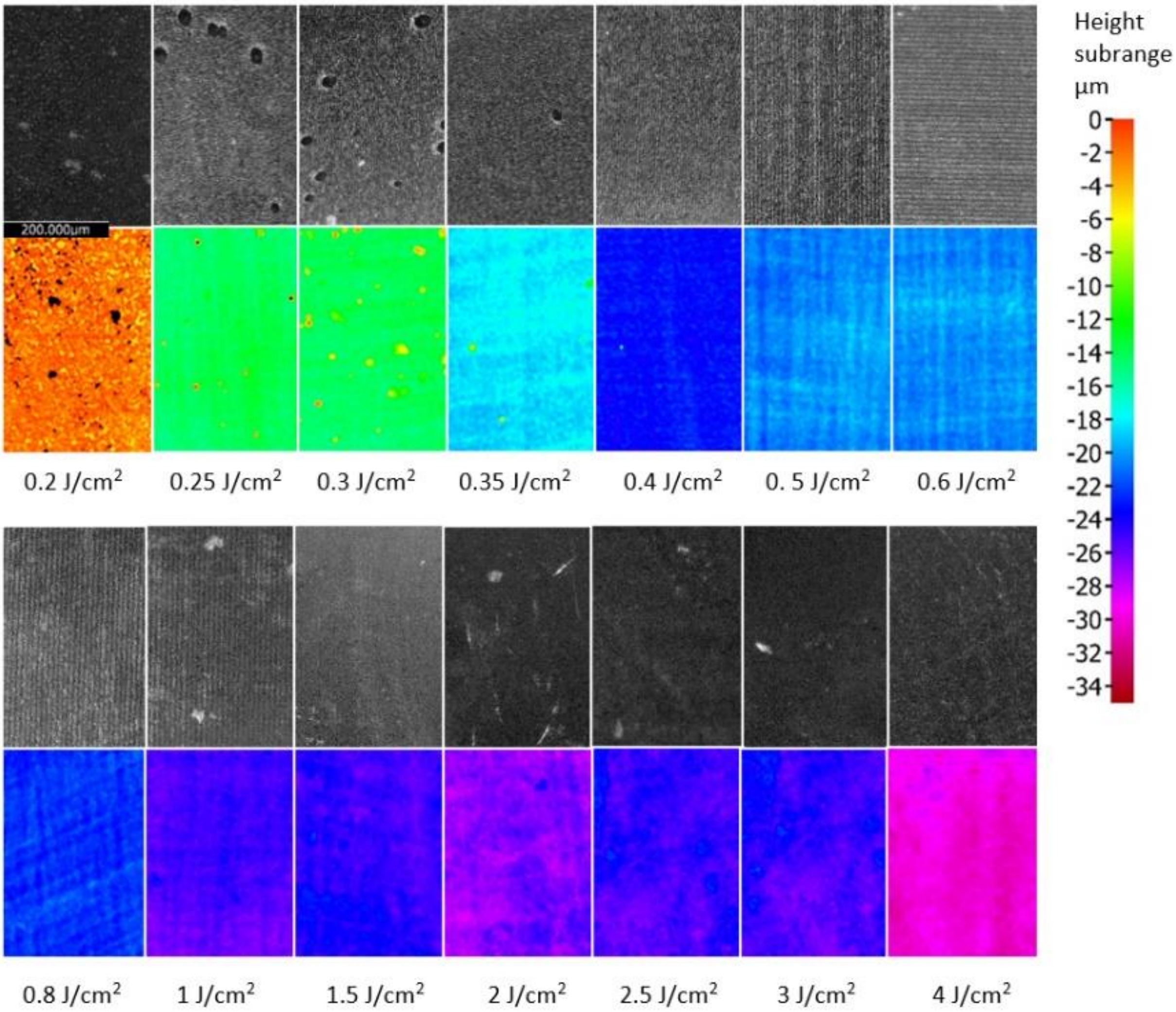
200.000µm
Height subrange µm
0
-2
-4
-6
-8
-10
-12
-14
-16
-18
-20
-22
-24
-26
-28
-30
-32
-34

0.2 J/cm^2 0.25 J/cm^2 0.3 J/cm^2 0.35 J/cm^2 0.4 J/cm^2 0. 5 J/cm^2 0.6 J/cm^2

0.8 J/cm^2 1 J/cm^2 1.5 J/cm^2 2 J/cm^2 2.5 J/cm^2 3 J/cm^2 4 J/cm^2

Figure 29: Micrographs and Alicona height map images. 1028 nm wavelength. Range 0-35 µm.

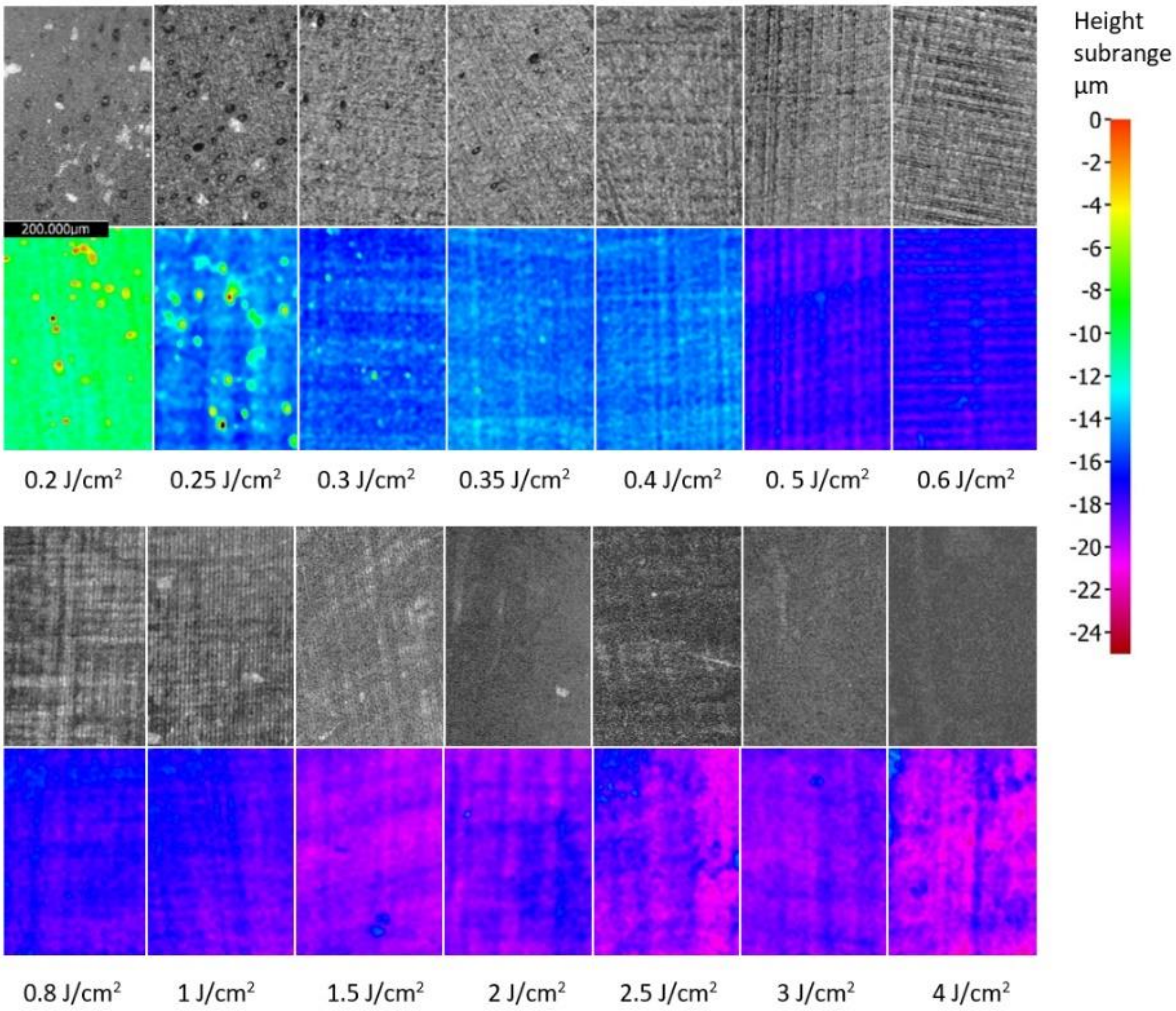
200.000µm
Height subrange µm
0
-2
-4
-6
-8
-10
-12
-14
-16
-18
-20
-22
-24
0.2 J/cm²
0.25 J/cm²
0.3 J/cm²
0.35 J/cm²
0.4 J/cm²
0. 5 J/cm²
0.6 J/cm²
0.8 J/cm²
1 J/cm²
1.5 J/cm²
2 J/cm²
2.5 J/cm²
3 J/cm²
4 J/cm²

Figure 30: Micrographs and Alicona height map images. 514 nm wavelength. Range 0-25 µm.

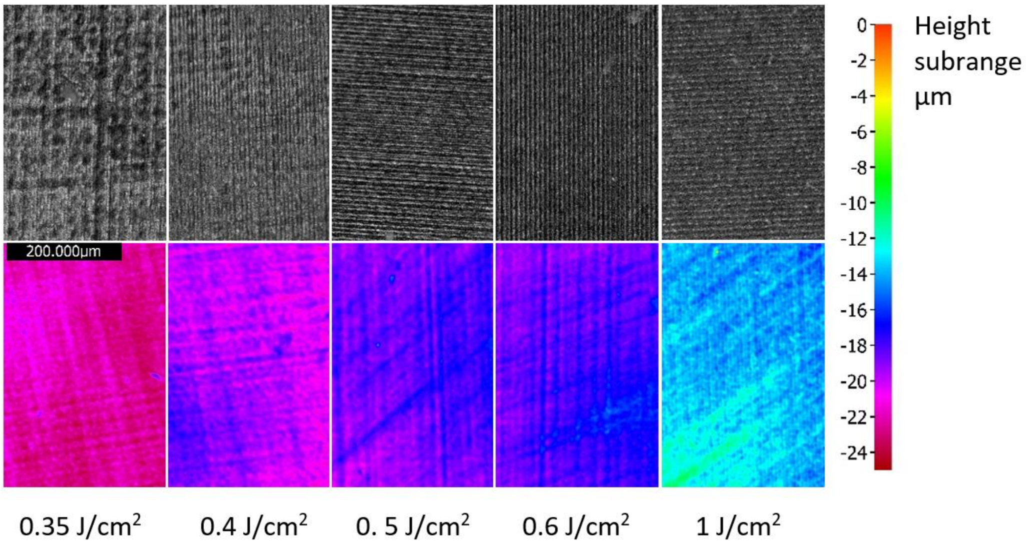
200.000µm
0
-2
-4
-6
-8
-10
-12
-14
-16
-18
-20
-22
-24
Height subrange µm
0.35 J/cm²
0.4 J/cm²
0. 5 J/cm²
0.6 J/cm²
1 J/cm²

Figure 31: Micrographs and Alicona height map images. 343 nm wavelength. Range 0-25 µm.

4.5 HEAT INPUT

In Figure 28, the heat input (REC) is shown, corresponding to the wavelength and laser fluence used. The graphs of the temperature of each experiment are shown in Appendix E. The REC for both 1028 nm and 514 nm shows a clear trend where the REC decreases with increasing laser fluence. The REC seems to stabilize around 0.27 independent of the wavelength in the studied fluence level range. The results for the heat input at 343 nm are similar, but due to the lack of experimental data, a trend cannot be observed. So, independent of the studied wavelengths, the REC is higher for laser fluence levels below the optimum laser fluence. Above the optimum laser fluence, the REC shows only little change.

Recent work on the heat input measurement of USP laser ablation showed similar results to those observed here, around 30% [18]. This experiment shows that this is only valid for a certain range of laser fluence levels. A. Y. Vorobyev and C. Guo [15] showed an increase in REC in air for higher laser fluence levels up to 10 J/cm^2. This research does not show this effect in the studied range. They conclude that the difference in REC was due to redeposited material. In their research, different materials and a drilling process were used, which could explain the differences. Mikhaylov *et al.* [1] used a constant heat input of 30%, independent of the laser fluence, for their calculations. This research shows a different insight, and therefore, their results might be different in practice.

Via a simple model that was derived from the model of Bartels *et al.* [19], the heating energy in relation to the total energy in the pulse was calculated. The equation for REC is derived from the model, and the derivation steps for the equation are shown in Appendix C. Via this simple model, the REC was calculated as,

$$REC = a * \frac{F_{0,th}}{F_0}\left(1 - \ln\left(\frac{F_{0,th}}{F_0}\right)\right), \tag{4.1}$$

where a is the absorption coefficient without unit, $F_{0,th}$ is the threshold peak laser fluence, F_0 is the peak laser fluence. In Figure 32, a = 0.8 was used, and the model shape partly represents the measured REC curve for 1028 nm.

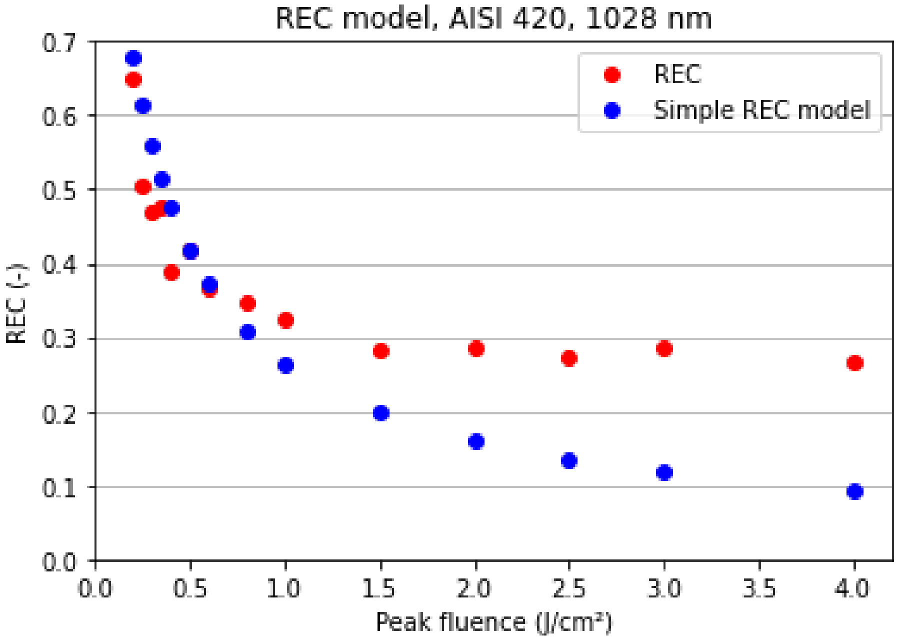

Figure 32: REC as a function of the peak fluence. Simple REC model. a = 0.8.

4.6 COOLING OF A SHAVINGHEAD

Figure 33 and Figure 34 show the temperature of the shaving head during the ablation process. Without cooling, the temperature reached 267 °C directly under the ablation area (outer thermocouple, see Section 3.2.7). The temperature difference with the environment was 245 °C. There was a difference in measured temperature between the inner and outer thermocouples due to a non-homogenous temperature distribution in the part. Forced air-cooling shows a big drop in temperature. The temperature difference between the shaving head and the environment, with cooling, was 74 °C. For forced air-cooling, the ingoing heat flow and outgoing heat flow were equal after 10 s.

The results of this experiment show that a (non-optimized) forced air-cooling solution is capable of substantially reducing the temperature of the shaving head. A cold part could produce a better surface quality, as discussed in Section 2.3, and the material properties, such as hardness, are less likely to change.

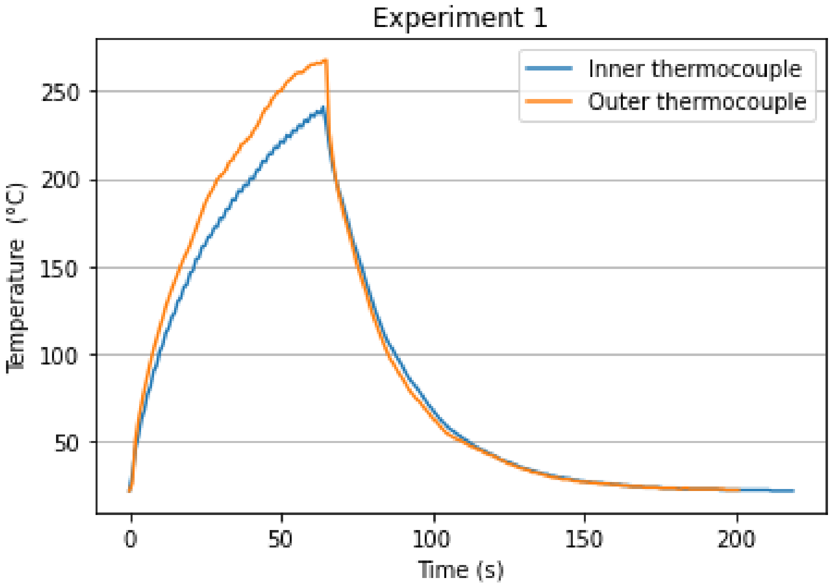

Figure 33: Temperature increase of a shaving head as a function of time. 17.7 W no forced cooling.

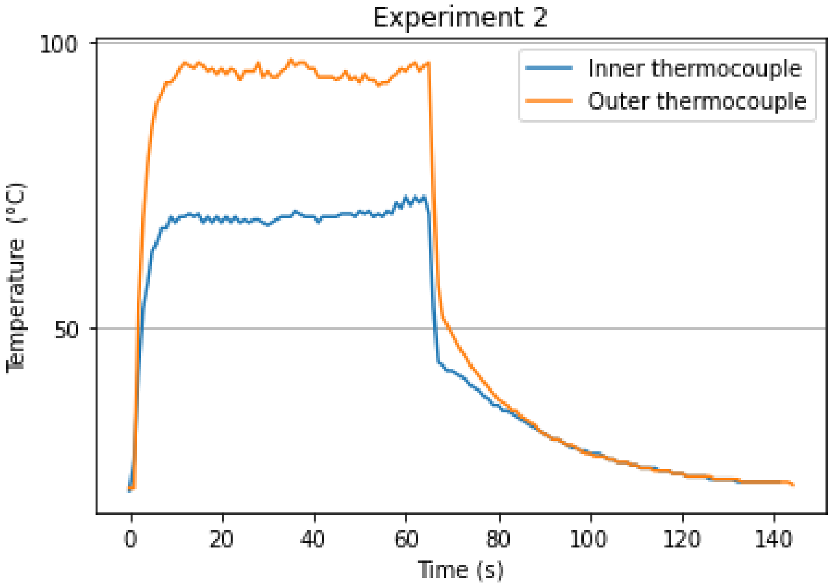

Figure 34: Temperature of a shaving head as a function of time. 17.7 W forced air-cooling.

5. CONCLUSIONS & RECOMMENDATIONS

5.1 CONCLUSIONS

In this thesis, through literature research, most of the processing parameters of Ultrashort pulsed (USP) laser ablation and their effects on the ablation efficiency, heat input, and surface quality are described. The research gap for the specific cases for Philips was further investigated via experiments aimed at the ablation efficiency at different wavelengths, the heat input as a function of laser fluence, and the cooling of a shaving head.

The surface quality after ablation can show different issues, such as a rough surface, cone like pillars, and inclusion induced cones. The laser fluence and surface temperature during the laser ablation process have the greatest impact on the surface quality. To increase the ablation rate (mm^3/min), the most important parameter is the average laser power of the laser source, but this can also have an adverse effect on the surface roughness. Literature shows good-quality surfaces with high average laser power using high scanning speeds to reduce the surface temperature just before the next pulse.

The heat input and ablation efficiency were analysed for wavelengths of 1028 nm, 514 nm, and 343 nm. The temperature was measured during the ablation process using a thermocouple and a sample holder that was specifically designed to minimize external heat losses. The ablated volume, average power during the process, and duration of the process were used to calculate the ablation efficiency. The ablation efficiency for 1 ps pulse duration, 0.1 W average laser power, and the different wavelengths shows similar results as found in the literature and fits with a theoretical model. The maximum ablation efficiency of 0.259 $mm^3/(W \cdot min)$ was reached in experiments with 514 nm wavelength, 19.9 µm spot diameter, 0.6 J/cm^2 peak fluence, 107.6 kHz pulse repetition rate, and 21.4 mm/s scan speed. The maximum ablation efficiency for 1028 nm was 0.227 $mm^3/(W \cdot min)$ with a 28.4 µm spot diameter, 0.8 J/cm^2 peak fluence, 39.5 kHz pulse repetition rate, and 11.2 mm/s scan speed. The difference in ablation efficiency can be explained by the difference in absorption at the respective wavelengths.

This thesis shows a new insight into the behaviour of the Residual Energy Coefficient (REC) as a function of the laser fluence. For a low laser fluence of close to twice the ablation threshold, the REC is relatively high. For laser fluence levels around the optimum for ablation efficiency, the REC decreases to an asymptote of approximately 27%. A limitation of this study is that high average laser powers could not be studied for ablation efficiency and REC, and it might show different results. For the cases in Philips, an ablation rate of 0.228 mm^3/s (or 13.7 mm^3/min) is required due to the maximum processing time per part and the required volume which needs to be removed. Research showed that current laser ablation systems are capable of reaching this ablation rate using 306 W average laser power, 1030 nm wavelength, 3 ps pulse duration, 40 MHz pulse repetition rate, and a high-speed polygon scanner with scan speeds up to 480 m/s.

A high average power laser source, that is needed to reach a high ablation rate, could be used for the mass production ablation process at Philips. The USP laser ablation process seems to be able to comply with all requirements for the cases of Philips as stated in Table 1. More research needs to be conducted on the temperature of the part for high average laser powers. One of the main challenges is to ensure a high-quality finish with the high ablation rate process. The heat input for different laser settings was observed, and with this knowledge, an adequate cooling solution can be designed for the small metal part. This can enable a high average power laser source without exceeding the maximum bulk material temperature of 250 °C of the part.

5.2 RECOMMENDATIONS

USP laser ablation shows promising results to incorporate in the mass production process of Philips, although further, more case specific research is needed.

The ablation rate that is needed in the cases of Philips can be reached, and even more powerful laser sources are still being developed. The quality of the resulting surface and the temperature of small parts at high average laser powers are topics for further research. Polygon scanners that can reach high scanning speeds were used for high average laser power ablation. However, they cannot deliver high duty cycles in the case of Philips due to the donut shape of the ablation area. Research into high-speed rotational scanning systems could help enable high average laser powers by using high repetition rate laser sources for the cases of Philips.

Only relatively low average laser powers were used in this thesis, with a maximum of 0.1 W for the heat input and ablation efficiency experiments, and 25 W for the surface quality experiments. The surface quality, ablation efficiency, heat input, and part temperature at high average laser powers for AISI 420 stainless steel are not studied. It is recommended that high average laser powers up to 300 W will be studied to analyse the limits of the process. This would require a powerful laser source, an active cooling solution, and a solution to reach high scanning speeds.

For a broader overview of the heat input and ablation efficiency for AISI 420 stainless steel, it is recommended to conduct research with a wider range of process settings. The heat input for higher average laser powers is important to study because the temperature of the part could be a bottleneck for the process speed.

As seen in the literature, GHz burst laser pulses with a high number of laser pulses in the burst can increase the ablation efficiency of the laser ablation process. The ablation cooling mechanism could be useful to further increase the ablation rate. The surface finish after the ablation cooling process is not yet known for small stainless-steel parts, and this can be further researched.

BIBLIOGRAPHY

[1] D. Mikhaylov, T. Kiedrowski, and A. F. Lasagni, ‘Heat accumulation effects during ultrashort pulse laser ablation with spatially shaped beams’, *Journal of Laser Micro/Nanoengineering*, vol. 13, no. 2, pp. 95-99 2018, doi: 10.2961/jlmn.2018.02.0008.

[2] J. Finger, C. Kalupka, and M. Reininghaus, ‘High power ultra-short pulse laser ablation of IN718 using high repetition rates’, *J Mater Process Tech*, vol. 226, pp. 221-227, 2015, doi: 10.1016/j.jmatprotec.2015.07.014.

[3] G. Bonamis, K. Mishchick, E. Audouard, C. Hönninger, E. Mottay, J. Lopez, I. Manek-Hönninger, ‘High efficiency femtosecond laser ablation with gigahertz level bursts’, *J Laser Appl*, vol. 31, no. 2, 2019, doi: 10.2351/1.5096087.

[4] N. Hodgson, A. Steinkopff, S. Heming, H. Allegre, H. Haloui, T. S. Lee, M. Laha, J. VanNunen, ‘Ultrafast laser machining: process optimization and applications’, In Proc. SPIE LASE, 2021, doi: 10.1117/12.2584178.

[5] T.H.Maiman, ‘Stimulated optical radiation in ruby’, *Nature, 187(4736):493-494* , 1960.

[6] D. Strickland and G. Mourou, ‘Compression of amplified chirped optical pulses’, Optics Communications, vol. 55, no 6, 1985.

[7] A. Brenner, F. Kurzidim, C. Fornaroli, and A. Gillner, ‘Combination of short and ultrashort pulse laser processing for productive large scale structuring of 3D plastic mould steel’, *J Laser Appl*, vol. 30, no. 3, 2018, doi: 10.2351/1.5040621.

[8] K. H. Leitz, B. Redlingshöer, Y. Reg, A. Otto, and M. Schmidt, ‘Metal ablation with short and ultrashort laser pulses’, in *Physics Procedia*, pp. 230-238, 2011, doi: 10.1016/j.phpro.2011.03.128.

[9] K. Du, S. Brüning, and A. Gillner, ‘High-power picosecond laser with 400W average power for large scale applications’, in *Laser-based Micro- and Nanopackaging and Assembly VI*, p. 82440P., 2012, doi: 10.1117/12.915676.

[10] V. Villerius, H. Kooiker, J. Post, and Y. T. Pei, ‘Ultrashort pulsed laser ablation of stainless steels’, *Int J Mach Tools Manuf*, vol. 138, pp. 27-35, 2019, doi: 10.1016/j.ijmachtools.2018.11.003.

[11] Lightmotif, Appl. Note, ‘Micro-milling processes introduction’ page 13, 22.

[12] E. J. Y. Ling, J. Saïd, N. Brodusch, R. Gauvin, P. Servio, and A. M. Kietzig, ‘Investigating and understanding the effects of multiple femtosecond laser scans on the surface topography of stainless steel 304 and titanium’, *Appl Surf Sci*, vol. 353, pp. 512-521, 2015, doi: 10.1016/j.apsusc.2015.06.137.

[13] F. Bauer, A. Michalowski, T. Kiedrowski, and S. Nolte, ‘Heat accumulation in ultra-short pulsed scanning laser ablation of metals’, *Opt Express*, vol. 23, no. 2, 2015, doi: 10.1364/oe.23.001035.

[14] G. Raciukaitis, ‘Ultra-Short Pulse Lasers for Microfabrication: A Review’, *IEEE Journal of Selected Topics in Quantum Electronics*, vol. 27, no. 6, 2021, doi: 10.1109/JSTQE.2021.3097009.

[15] A. Y. Vorobyev and C. Guo, ‘Enhanced energy coupling in femtosecond laser-metal interactions at high intensities’, *Opt Express*, vol. 14, no. 26, 2006.

[16] B. Jäggi, D. J. Förster, R. Weber, and B. Neuenschwander, ‘Residual heat during laser ablation of metals with bursts of ultra-short pulses’, *Advanced Optical Technologies*, vol. 7, no. 3, pp. 175-182, 2018, doi: 10.1515/aot-2018-0003.

[17] A. Y. Vorobyev and C. Guo, ‘Direct observation of enhanced residual thermal energy coupling to solids in femtosecond laser ablation’, *Appl Phys Lett*, vol. 86, no. 1, 2005, doi: 10.1063/1.1844598.

[18] F. Bauer, A. Michalowski, and S. Nolte, ‘Residual heat in ultra-short pulsed laser ablation of metals’, *Journal of Laser Micro/Nanoengineering*, vol. 10, no. 3, pp. 325-328, 2015, doi: 10.2961/jlmn.2015.03.0016.

[19] T. Barthels, M. Niessen, M. Reininghaus, and Y. Wang, ‘High-precision ultrashort pulsed laser processing of metal foils using an advanced multibeam optic’, In Proc. SPIE LASE vol 11267, 2020, doi: 10.1117/12.2551994.

[20] T. Kramer, Y. Zhang, S. Temund, B. Jaeggi, A. Michalowski, L. Grad, B. Neuenschwander, ‘Increasing the specific removal rate for ultra short pulsed laser-micromachining by using pulse bursts’, *Journal of Laser Micro/Nanoengineering*, vol. 12, no. 2, pp. 107-114, 2017, doi: 10.2961/jlmn.2017.02.0011.

[21] R. Weber, T. Graf, P. Berger, V. Onuseit, M. Wiedenmann, C. Freitag, A. Feuer, ‘Heat accumulation during pulsed laser materials processing’, *Opt Express*, vol. 22, no. 9, 2014, doi: 10.1364/oe.22.011312.

[22] A. Rahaman, A. Kar, and X. Yu, ‘Thermal effects of ultrafast laser interaction with polypropylene’, *Opt Express*, vol. 27, no. 4, 2019, doi: 10.1364/oe.27.005764.

[23] L. Cangueiro, J. A. Ramos-De-campos, and D. Bruneel, ‘Prediction of thermal damage upon ultrafast laser ablation of metals’, *Molecules*, vol. 26, no. 21, 2021, doi: 10.3390/molecules26216327.

[24] S. Faas, U. Bielke, R. Weber, and T. Graf, ‘Prediction of the surface structures resulting from heat accumulation during processing with picosecond laser pulses at the average power of 420 W’, *Appl Phys A Mater Sci Process*, vol. 124, no. 9, 2018, doi: 10.1007/s00339-018-2040-4.

[25] B. Jaeggi, S. Remund, R. Streubel, B. Goekce, S. Barcikowski, and B. Neuenschwander, ‘Laser Micromachining of Metals with Ultra-Short Pulses: Factors Limiting the Scale-Up Process’, *Journal of Laser Micro/Nanoengineering*, vol. 12, no. 3, pp. 267–273, 2017, doi: 10.2961/jlmn.2017.03.0016.

[26] J. Lopez, G. Mincuzzi, R. Devillard, Y. Zaouter, C. Hönninger, E. Mottay, R. Kling, ‘Ablation efficiency of high average power ultrafast laser’, *J Laser Appl*, vol. 27, no. S2, 2015, doi: 10.2351/1.4906479.

[27] B. Sallé, O. Gobert, P. Meynadier, M. Perdrix, G. Petite, and A. Semerok, ‘Femtosecond and picsosecond laser microablation: ablation efficiency and laser microplasma expansion’, *Appl. Phys. A*, pp. 381-383, 1999, doi: 10.1007/s003399900230.

[28] A. Brenner, M. Zecherle, S. Verpoort, K. Schuster, C. Schnitzler, M. Kogel-Hollacher, M. Reisacher, B. Nohn, ‘Efficient production of design textures on large-format 3D mold tools’, *J Laser Appl*, vol. 32, no. 1, 2020, doi: 10.2351/1.5132401.

[29] B. Jaeggi, B. Neuenschwander, M. Zimmermann, L. Penning, R. deLoor, K. Weingarten, A. Oehler, ‘High Throughput and High Precision Laser Micromachining with ps-Pulses in Synchronized Mode with a fast Polygon Line Scanner’, In Proc. SPIE vol. 8967, doi: 10.24451/arbor.11329.

[30] J. Schille, L. Schneider, A. Streek, S. Kloetzer, and U. Loeschner, ‘High-throughput machining using a high-average power ultrashort pulse laser and high-speed polygon scanner’, *Optical Engineering*, vol. 55, no. 9, p. 096109, 2016, doi: 10.1117/1.oe.55.9.096109.

[31] P. Gecys, B. Voisiat, G. Raciukaitis, G. Račiukaitis, M. Brikas, and P. Gečys, ‘Use of High Repetition Rate and High Power Lasers in Microfabrication: How to Keep the Efficiency High?’, in *Journal of Laser Micro/Nanoengineering Vol. 4 No. 3*, 2009.

[32] B. Neuenschwander, G. F. Bucher, C. Nussbaum, B. Joss, M. Muralt, U. W. Hunziker, P. Schuetz, ‘Processing of metals and dielectric materials with ps-laserpulses: results, strategies, limitations and needs’, in *Laser Applications in Microelectronic and Optoelectronic Manufacturing XV*, 2010, doi: 10.1117/12.846521.

[33] B. Neuenschwander, B. Jaeggi, and M. Schmid, ‘From fs to sub-ns: Dependence of the material removal rate on the pulse duration for metals’, in *Physics Procedia*, pp. 794-801, 2013, doi: 10.1016/j.phpro.2013.03.150.

[34] B. Neuenschwander, B. Jaeggi, M. Schmid, and G. Hennig, ‘Surface structuring with ultra-short laser pulses: Basics, limitations and needs for high throughput’, in *Physics Procedia*, pp. 794-801, 2014, doi: 10.1016/j.phpro.2014.08.017.

[35] B. Neuenschwander, B. Jaeggi, M. Schmid, V. Rouffiange, and P.-E. Martin, ‘Optimization of the volume ablation rate for metals at different laser pulse-durations from ps to fs’, In Proc. SPIE vol. 8243, doi: 10.24451/arbor.11318.

[36] H. Feitsma, ‘Research project, high power ultrashort pulsed laser ablation’, M. S. thesis, University of Groningen, Groningen, 2020.

[37] J. Lopez, R. Kling, R. Torres, A. Lidolff, M. Delaigue, S. Ricaud, C. Hönninger, E. Mottay, ‘Comparison of picosecond and femtosecond laser ablation for surface engraving of metals and semiconductors’, in *Laser Applications in Microelectronic and Optoelectronic Manufacturing (LAMOM) XVII*, 2012, doi: 10.1117/12.907792.

[38] N. Hodgson, H. Haloui, T. S. Lee, E. Rea, ‘Laser wavelength selection for optimized ultrafast laser micromachining applications’, presented at UPK-Workshop ILT, Aachen, 2021.

[39] M. Chaja, T. Kramer, and B. Neuenschwander, ‘Influence of laser spot size and shape on ablation efficiency using ultrashort pulse laser system’, in Proc. CIRP, pp. 300-304, 2018, doi: 10.1016/j.procir.2018.08.119.

[40] N. Hodgson, S. Heming, A. Steinkopff, H. Haloui, and T. S. Lee, ‘Ultrafast laser ablation at 1035 n, 517 and 345 nm as a Function of Pulse Duration and Fluence’, In Proc. Lasers in Manufacturing, 2019.

[41] J. Schille, L. Schneider, and U. Loeschner, ‘Process optimization in high-average-power ultrashort pulse laser microfabrication: how laser process parameters influence efficiency, throughput and quality’, *Appl Phys A Mater Sci Process*, vol. 120, no. 3, pp. 847-855, 2015, doi: 10.1007/s00339-015-9352-4.

[42] J. Jyothi, A. Biswas, P. Sarkar, A. Soum-Glaude, H. S. Nagaraja, and H. C. Barshilia, ‘Optical properties of TiAlC/TiAlCN/TiAlSiCN/TiAlSiCO/TiAlSiO tandem absorber coatings by phase-modulated spectroscopic ellipsometry’, *Appl Phys A Mater Sci Process*, vol. 123, no. 7, 2017, doi: 10.1007/s00339-017-1103-2.

[43] Amplitude, ‘Tangor 300 laser’, 2022. [Online]. Available: https://amplitude-laser.com/products/lasers-for-industry/tangor-300/ [Accessed: Aug. 2, 2023].

[44] P. Gecys, B. Voisiat, G. Raciukaitis, G. Račiukaitis, M. Brikas, and P. Gečys, ‘Use of High Repetition Rate and High Power Lasers in Microfabrication: How to Keep the Efficiency High?’, *Journal of Laser Micro/Nanoengineering*, vol. 4, no. 3, 2009.

[45] D. J. Förster, B. Jäggi, A. Michalowski, and B. Neuenschwander, ‘Review on experimental and theoretical investigations of ultra-short pulsed laser ablation of metals with burst pulses’, *Materials*, vol. 14, no. 12, 2021, doi: 10.3390/ma14123331.

[46] J. König, S. Nolte, A. Tünnermann, 'Plasma evolution during metal ablation with ultrashort laser pulses', *Opt Express*, vol. 13, no. 26, 2005.

[47] O. Armbruster, A. Naghilou, M. Kitzler, and W. Kautek, 'Spot size and pulse number dependence of femtosecond laser ablation thresholds of silicon and stainless steel', *Appl Surf Sci*, vol. 396, pp. 1736-1740, 2017, doi: 10.1016/j.apsusc.2016.11.229.

[48] E. I. Ugwu, J. E. Ekpe, E. Nnaji, and E. H. Uguru, 'Theoretical Study of Electromagnetic Wave Propagation: Gaussian Bean Method', *Appl Math (Irvine)*, vol. 04, no. 10, pp. 1466-1470, 2013, doi: 10.4236/am.2013.410198.

[49] B. Lauer, B. Jaeggi, Y. Zhang, and B. Neuenschwander, 'Measurement of the maximum specific removal rate: unexpected influence of the experimental method and the spot size', ICALE, Paper M701, 2015, doi: 10.2351/1.5063162.

[50] M. Eyett and D. Bäuerle, 'Influence of the beam spot size on ablation rates in pulsed-laser processing', *Appl Phys Lett*, vol. 51, no. 24, pp. 2054-2055, 1987, doi: 10.1063/1.98290.

[51] M. E. Shaheen, J. E. Gagnon, and B. J. Fryer, 'Excimer laser ablation of aluminum: Influence of spot size on ablation rate', *Laser Phys*, vol. 26, no. 11, 2016, doi: 10.1088/1054-660X/26/11/116102.

[52] S. Rung, J. Barth, and R. Hellmann, 'Characterization of laser beam shaping optics based on their ablation geometry of thin films', *Micromachines*, vol. 5, no. 4, pp. 943-953, 2014, doi: 10.3390/mi5040943.

[53] H. Le, P. Penchev, A. Henrottin, D. Bruneel, V. Nasrollahi, J. A. Ramos-de-Campos, S. Dimov, 'Effects of top-hat laser beam processing and scanning strategies in laser micro-structuring', *Micromachines*, vol. 11, no. 2, 2020, doi: 10.3390/mi11020221.

[54] A. Žemaitis, M. Gaidys, P. Gečys, M. Barkauskas, and M. Gedvilas, 'Femtosecond laser ablation by bibursts in the MHz and GHz pulse repetition rates', *Opt Express*, vol. 29, no. 5, p. 7641, 2021, doi: 10.1364/oe.417883.

[55] Lumentum, 'Pulse-bursts in ultrashort-pulsed lasers FlexBurst^{TM} technology', white paper, 2022. [Online]. Available: https://www.lumentum.com/en/forms/flex-burst [accessed: Jan. 1, 2023].

[56] B. Jaeggi, S. Remund, Y. Zhang, T. Kramer, and B. Neuenschwander, 'Optimizing the specific removal rate with the burst mode under varying conditions', *Journal of Laser Micro/Nanoengineering*, vol. 12, no. 3, pp. 258-266, 2017, doi: 10.2961/jlmn.2017.03.0015.

[57] N. Hodgson, H. Allegre, A. Starodoumov, and S. Bettencourt, 'Femtosecond Laser Ablation in Burst Mode as a Function of Pulse Fluence and Intra-Burst Repetition Rate', *Journal of Laser Micro/Nanoengineering*, vol. 15, no. 3, pp. 236-244, 2020, doi: 10.2961/jlmn.2020.03.2014.

[58] T. Hirsiger, M. Gafner, S. Remund, M. V. Chaja, A. Urniezius, S. Butkus, B. Neuenschwander, 'Machining metals and silicon with GHz bursts: Surprising tremendous reduction of the specific removal rate for surface texturing applications', In Proc. LAMON XXV, doi: 10.24451/arbor.11707.

[59] G. Bonamis, E. Audouard, C. Hönninger, J. Lopez, K. Mishchik, E. Mottay, M. Hönninger, 'Systematic study of laser ablation with GHz bursts of femtosecond pulses', *Opt Express*, vol. 28, no. 19, 2020, doi: 10.1364/oe.400624.

[60] E. Audouard and E. Mottay, 'High efficiency GHz laser processing with long bursts', *International Journal of Extreme Manufacturing*, vol. 5, no. 1, 2023, doi: 10.1088/2631-7990/aca79f.

[61] C. Kerse, H. Kalaycioglu, P. Elahi, B. Cetin, D. K. Kesim, Ö. Akcaalan, S. Yavas, M. D. Asik, B. Öktem, H. Hoogland, R. Holzwarth, F. Ömer Ilday, ‘Ablation-cooled material removal with ultrafast bursts of pulses’, *Nature*, vol. 537, no. 7618, pp. 84-88, 2016, doi: 10.1038/nature18619.

[62] C. Kerse, H. Kalaycioglu, P. Elahi, B. Cetin, D. K. Kesim, Ö. Akcaalan, S. Yavas, M. D. Asik, B. Öktem, H. Hoogland, R. Holzwarth, F. Ömer Ilday, ‘Simulation of ultrafast bursts of subpicosecond pulses: In pursuit of efficiency’, *Appl Phys Lett*, vol. 112, no. 5, 2018, doi: 10.1063/1.5012758.

[63] S. Bruening, K. Du, and A. Gillner, ‘Micro processing with ultrafast bursts of pulses’, in Proc. CIRP, pp. 856-862, 2020, doi: 10.1016/j.procir.2020.09.110.

[64] S. M. Remund, M. Gafner, M. V. Chaja, A. Urniezius, S. Butkus, and B. Neuenschwander, ‘Milling applications with GHz burst: Investigations concerning the removal rate and machining quality’, in Proc. CIRP, pp. 850-855, 2020, doi: 10.1016/j.procir.2020.09.111.

[65] K. Obata, F. Caballero-Lucas, and K. Sugioka, ‘Material Processing at GHz Burst Mode by Femtosecond Laser Ablation’, *Journal of Laser Micro/Nanoengineering*, vol. 16, no. 1, pp. 1-5, 2021, doi: 10.2961/jlmn.2021.01.2004.

[66] C. Gaudiuso, B. Stampone, G. Trotta, A. Volpe, and A. Ancona, ‘Investigation of the micro-milling process of steel with THz bursts of ultrashort laser pulses’, *Opt Laser Technol*, vol. 162, 2023, doi: 10.1016/j.optlastec.2023.109301.

[67] R. Knappe, H. Haloui, A. Seifert, A. Weis, and A. Nebel, ‘Scaling ablation rates for picosecond lasers using burst micromachining’, in *Laser-based Micro- and Nanopackaging and Assembly IV*, 2010, doi: 10.1117/12.842318.

[68] C. Lutz, C. Esen, and R. Hellmann, ‘Ultrashort-pulsed laser processing with spatial and temporal beam shaping using a spatial light modulator and burst modes’, *IOP Conf Ser Mater Sci Eng*, vol. 1135, no. 1, 2021, doi: 10.1088/1757-899x/1135/1/012026.

[69] J. Finger and M. Hesker, ‘High power ultrashort pulse laser processing using a flexible multibeam approach’, *J Phys Photonics*, vol. 3, no. 2. 2021. doi: 10.1088/2515-7647/abf24f.

[70] M. El-Khoury, B. Voisiat, T. Kunze, and A. F. Lasagni, ‘Utilizing a Diffractive Focus Beam Shaper to Enhance Pattern Uniformity and Process Throughput during Direct Laser Interference Patterning’, *Materials*, vol. 15, no. 2, 2022, doi: 10.3390/ma15020591.

[71] Cailabs, ‘The CANUNDA-SPLIT solution’, 2023. [Online]. Available: https://www.cailabs.com/en/product/canunda-split/ [Accessed: Aug. 2, 2023].

[72] Z. Kuang, D. Liu, W. Perrie, S. Edwardson, M. Sharp, E. Fearon, G. Dearden, K. Watkins, ‘Fast parallel diffractive multi-beam femtosecond laser surface micro-structuring’, *Appl Surf Sci*, vol. 255, no. 13–14, pp. 6582-6588, 2009, doi: 10.1016/j.apsusc.2009.02.043.

[73] F. Nyenhuis, A. Michalowski, and J. A. L’huillier, ‘Surface treatment with GHz-bursts’, In Proc. SPIE LASE 11268, 2020, doi: 10.1117/12.2544337.

[74] D. Metzner, P. Lickschat, and S. Weißmantel, ‘High-quality surface treatment using GHz burst mode with tunable ultrashort pulses’, *Appl Surf Sci*, vol. 531, 2020, doi: 10.1016/j.apsusc.2020.147270.

[75] M. M. Rashad, ‘Measurements of Laser Beam Using Knife Edge Technique’, Thesis, Polytechnic University of Milano, Milan.

[76] M. Raškauskas, T. Jonavičius, ‘Carbide C20519 factory test certificate’, Light Conversion, Lithuania, Tech. Report. P4-F1 v.1.

[77] Alicona, ‘Alicona InfiniteFocus G5’, 2023. [Online]. Available: https://www.ems-benelux.com/producten/alicona-infinite-focus-g5 [Accessed: Aug. 2, 2023].

[78] K. Technologies, ‘Keysight 34970A/34972A Data Acquisition / Switch Unit User’s Guide’, 2009. [Online]. Available: www.keysight.com/find/34970A [Accessed: Aug. 2, 2023].

[79] Coherent, ‘Coherent PM10’, 2021. [Online]. Available: *https://coherentinc.my.site.com/Coherent/laser-measurement/power-energy-sensors/thermopile-power-sensors/1097901?cclcl=en_US%7CPM10* [Accessed: Aug. 2, 2023].

[80] Coherent, ‘FieldMaxII-TO Laser power meter’, 2021. [Online]. Available: *https://coherentinc.my.site.com/Coherent/laser-measurement/power-energy-meters/1098579?cclcl=en_US%7CFieldMax* [Accessed: Aug. 2, 2023].

[81] C. T. O’Sullivan, ‘Newton’s law of cooling—A critical assessment’, *Am J Phys*, vol. 58, no. 10, pp. 956-960, 1990, doi: 10.1119/1.16309.

[82] P. Lickschat, D. Metzner, S. Weibmantel, ‘Fundamental investigations of ultrashort pulsed laser ablation on stainless steel and cemented tungsten carbide’, *Int J Adv Manuf Technol 109, p. 1167-1175, 2020, doi: 10.1007/s00170-020-05502-8*

APPENDICES

APPENDIX B

The attenuator power and pulse repetition rate were set in the software of the laser source. The average laser power is measured after the focussing lens. The measured average power during the process is the average process power. The average process power is lower due to repositioning of the laser beam where the laser source is off. The removed volume is measured with an *Alicona* measurement system. The efficiency is calculated with,

$$\frac{\dot{V}}{P_{av}} = \frac{V}{P_{av} \cdot t},$$

where $\dot{V}/P_{av}$ is the ablation efficiency, V is the volume of the removed material as measured by the Alicona, P_{av} is the average power during the process including laser off time, t is the total time the process takes. For details see Section 3.2.8 (Laser settings) and Section 3.2.5 (Ablation efficiency method).

Figure B. 1: Results of the laser ablation experiments for different wavelengths.

Exp no.	Peak fluence (J/cm^2)	Attenuator power (%)	Average laser power (mW)	Average process power (mW)	Time (s)	Removed volume (mm^3)	Efficiency (mm^3/(W·min))
Wavelength 1028 nm							
1	0.2	12.1	99.9	62.3	117.2	0.00184	0.015
2	0.25	12.1	100	67.4	102.3	0.01613	0.140
3	0.3	12.1	100	71.9	96.4	0.01407	0.122
4	0.35	12.2	100.6	75.1	92.6	0.01914	0.165
5	0.4	12.2	100.7	77.8	90.2	0.02335	0.200
6	0.5	12.0	99.7	79.5	86.1	0.02182	0.191
7	0.6	16.2	100.3	83.2	83.8	0.02389	0.206
8	0.8	16.2	99.7	87.0	83.2	0.02732	0.227
9	1	16.2	101	89.8	82.2	0.02765	0.225
10	1.5	19.0	99.9	92.7	88.8	0.02715	0.198
11	2	21.5	100	94.8	97.6	0.02899	0.188
12	2.5	23.8	99.7	94.4	93.7	0.02698	0.183
13	3	25.2	100.7	97.5	127.1	0.03054	0.148
14	4	28.7	100	97.1	124.0	0.03007	0.150
Wavelength 514 nm							
15	0.2	51.1	100.3	57.5	126.8	0.01406	0.116
16	0.25	50.2	100.0	58.7	155.4	0.01958	0.173
17	0.3	47.0	100.0	62.9	107.8	0.02251	0.199
18	0.35	45.0	100.0	68.2	102.6	0.02465	0.211
19	0.4	43.5	99.9	71.5	98.3	0.02855	0.244
20	0.5	41.5	99.6	75.4	92.5	0.02978	0.256
21	0.6	39.8	100.4	87.0	89.3	0.03005	0.259
22	0.8	35.3	100.0	82.2	85.3	0.02880	0.246
23	1	33.3	99.5	85.2	84.4	0.03018	0.252
24	1.5	42.6	100.4	90.8	88.5	0.03088	0.231
25	2	39.6	100.4	93.1	97.4	0.03169	0.210
27	2.5	46.3	100.0	94.3	96.2	0.02718	0.180
26	3	44.1	99.6	94.9	126.9	0.03398	0.169
28	4	48.1	100.1	96.6	124.6	0.03155	0.157

Wavelength 343 nm							
29	0.35	81.3	100.0	75.5	92.3	0.03001	0.259
30	0.4	69.2	100.0	76.4	89.8	0.02965	0.259
31	0.5	60.8	100.0	79.7	84.9	0.02617	0.232
32	0.6	55.7	100.0	80.0	84.8	0.02448	0.216
33	1	78.4	100.3	89.2	80.7	0.02049	0.171

APPENDIX C

Barthels *et al.* [1] used a simple ablation model to calculate the temperature due to laser ablation. They used only the part of the laser fluence which is above the ablation threshold for ablation and the rest of the energy goes toward heating up the substrate. This is shown in Figure D. 1. With a lower peak laser fluence compared to the threshold fluence (right), the blue ablation area decreases in comparison to the orange heating area. This would result in an increase of the REC with a lower peak laser fluence. The theoretical REC can be calculated by analysing the volume of the heating part in comparison to the total volume underneath the 3D gaussian distribution. Figure D. 1 shows a cross section of the 3D gaussian distribution. The following calculations are used to come to a simple theoretical model for the heat input of USP laser ablation.

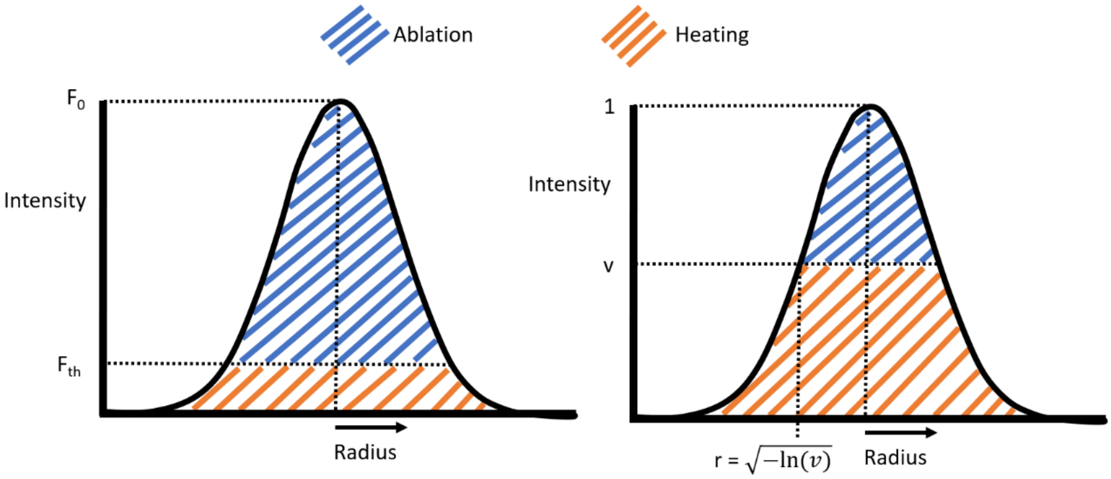

Figure D. 1: Simplified theoretical heat input model. Right shows when a relatively high peak fluence compared to the fluence threshold is used. Left shows when a relatively low peak fluence compared to the fluence threshold is used.

The total volume underneath a 3D gaussian distribution in polar coordinates is,

$$Volume = \int_0^{2\pi}\int_0^{\infty} e^{-r^2} r dr\, d\theta,$$

where r is the radius and θ in the angle. This is intersected by a plane at height v, where 0<v<1. The r coordinate of the intersection of the plane and the 3D gaussian distribution is,

$$e^{-r^2} = v,$$

$$r = \sqrt{-\ln(v)}. \qquad \text{Where } r > 0,\ v < 1.$$

The volume of the blue part is calculated by calculating the volume of the 3D gaussian up to the intersection point in r direction (II) and subtracting the volume of the orange part up to the intersection point in r direction (JJ). Working out the integral for II, the following result is obtained:

$$II = -v\pi + \pi.$$

Working out the integral for JJ, the following result is obtained:

$$JJ = \pi * \sqrt{-\ln(v)}^{2} * v = -\pi * v * \ln(v).$$

The volume used for heating (VH) is the total volume of the 3D gaussian distribution (π) minus the volume of the blue part:

$$VH = \pi - II - JJ = v\pi - \pi * v * \ln(v).$$

Since the total volume of the 3D gaussian distribution is π, the percentage of the total energy which is used for heating is,

$$\frac{VH}{\pi} = \ v - v * \ln(v).$$

REC is dependent on what amount is absorbed, so it is scaled with a factor (a),

$$REC = a * (v - v * \ln(v)).$$

v is the threshold peak laser fluence divided by the applied peak laser fluence,

$$v = \frac{F_{0,th}}{F_0}.$$

And thus, according to this simplified model, the REC is equal to,

$$REC = a * \frac{F_{0,th}}{F_0}\left(1 - \ln\left(\frac{F_{0,th}}{F_0}\right)\right).$$

Sources

[1] T. Barthels, M. Niessen, M. Reininghaus, and Y. Wang, “High-precision ultrashort pulsed laser processing of metal foils using an advanced multibeam optic,” SPIE-Intl Soc Optical Eng, 2020, p. 23. doi: 10.1117/12.2551994.

APPENDIX D

The temperature and cooling behaviour graphs of the heat input experiments are shown. The cooling behaviour is plotted as the temperature flow (K/s) as a function of the temperature of the sample. The cooling rate is fitted with a linear function. The temperature graphs show the measured temperature, the temperature compensated for cooling and a linear temperature increase fit as a function of time.

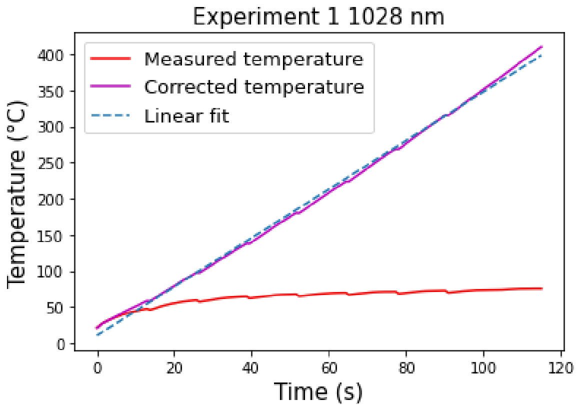

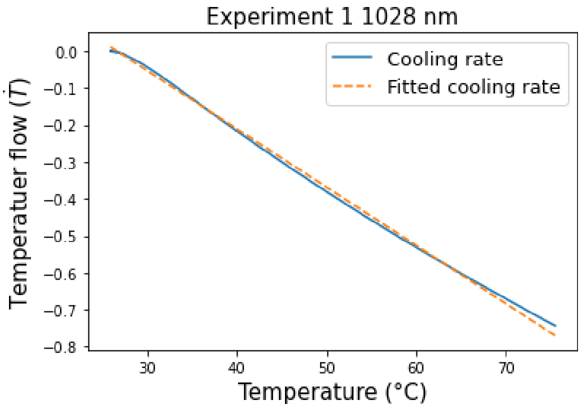

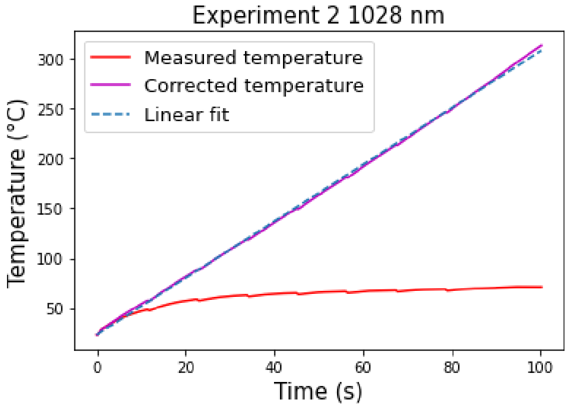

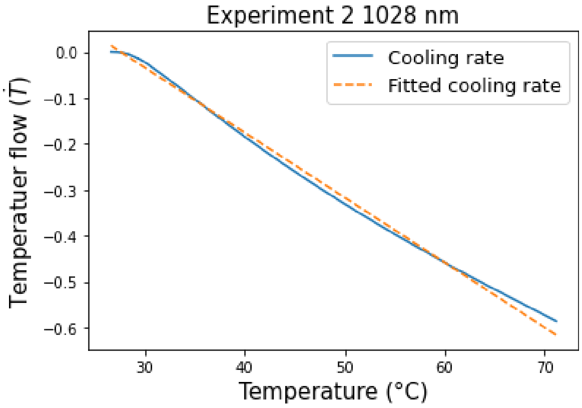

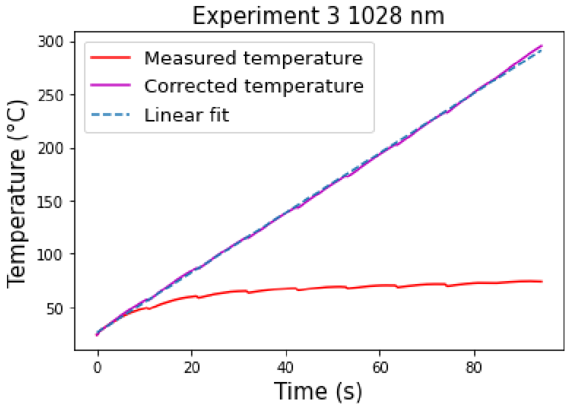

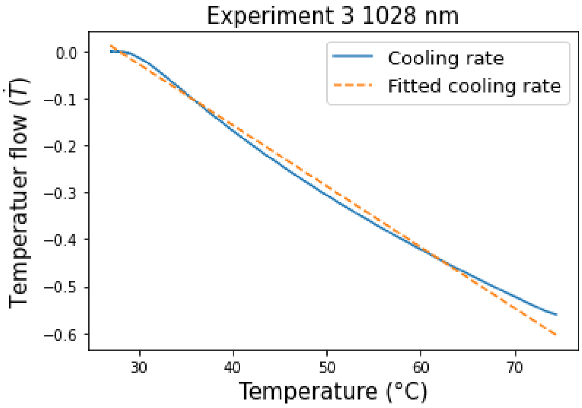

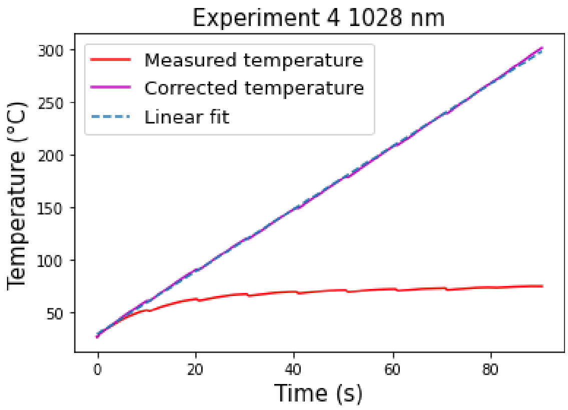
Experiment 4 1028 nm
Measured temperature
Corrected temperature
Linear fit
Temperature (°C)
300
250
200
150
100
50
0
20
40
60
80
Time (s)

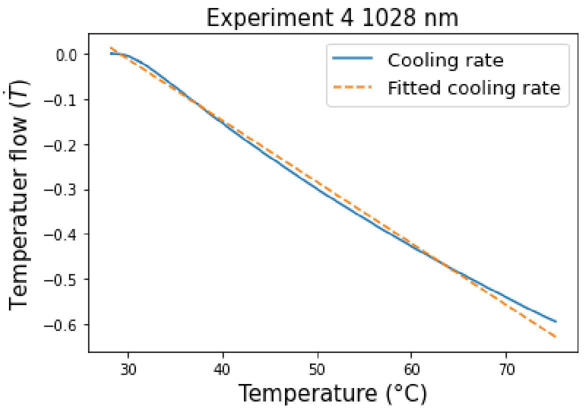
Experiment 4 1028 nm
Cooling rate
Fitted cooling rate
Temperatuer flow ($\dot{T}$)
0.0
−0.1
−0.2
−0.3
−0.4
−0.5
−0.6
30
40
50
60
70
Temperature (°C)

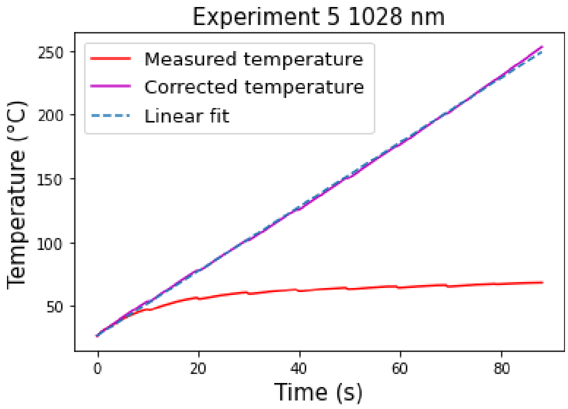
Experiment 5 1028 nm
Measured temperature
Corrected temperature
Linear fit
Temperature (°C)
250
200
150
100
50
0
20
40
60
80
Time (s)

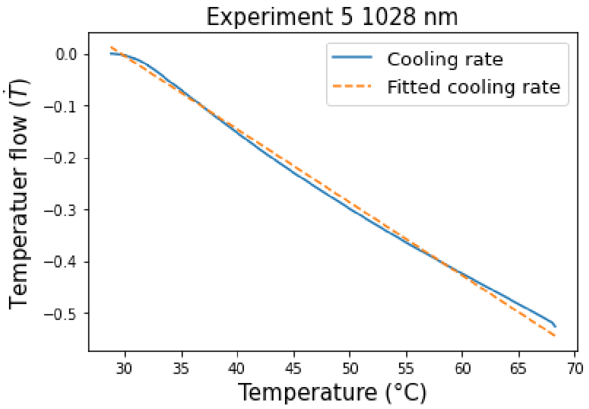
Experiment 5 1028 nm
Cooling rate
Fitted cooling rate
Temperatuer flow ($\dot{T}$)
0.0
−0.1
−0.2
−0.3
−0.4
−0.5
30
35
40
45
50
55
60
65
70
Temperature (°C)

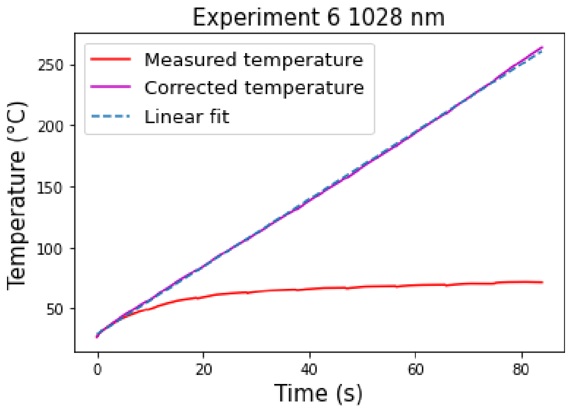
Experiment 6 1028 nm
Measured temperature
Corrected temperature
Linear fit
Temperature (°C)
250
200
150
100
50
0
20
40
60
80
Time (s)

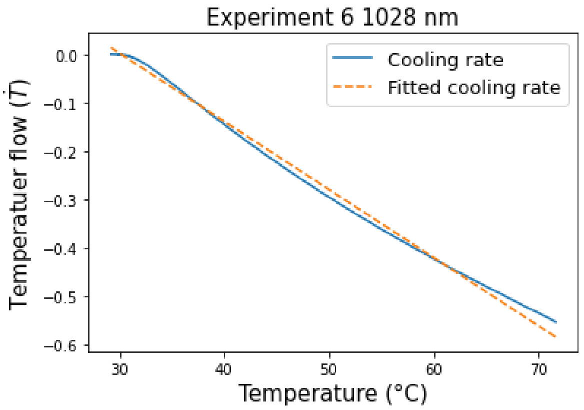
Experiment 6 1028 nm
Cooling rate
Fitted cooling rate
Temperatuer flow ($\dot{T}$)
0.0
−0.1
−0.2
−0.3
−0.4
−0.5
−0.6
30
40
50
60
70
Temperature (°C)

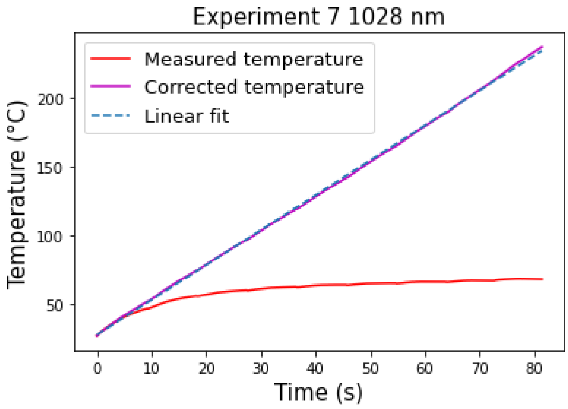
Experiment 7 1028 nm
Measured temperature
Corrected temperature
Linear fit
Temperature (°C)
200
150
100
50
0
10
20
30
40
50
60
70
80
Time (s)

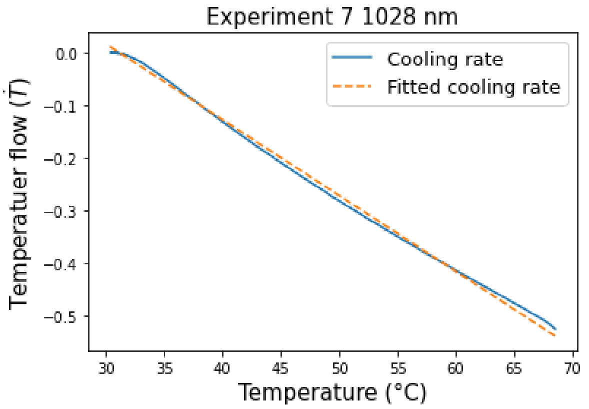
Experiment 7 1028 nm
Cooling rate
Fitted cooling rate
Temperatuer flow ($\dot{T}$)
0.0
−0.1
−0.2
−0.3
−0.4
−0.5
30
35
40
45
50
55
60
65
70
Temperature (°C)

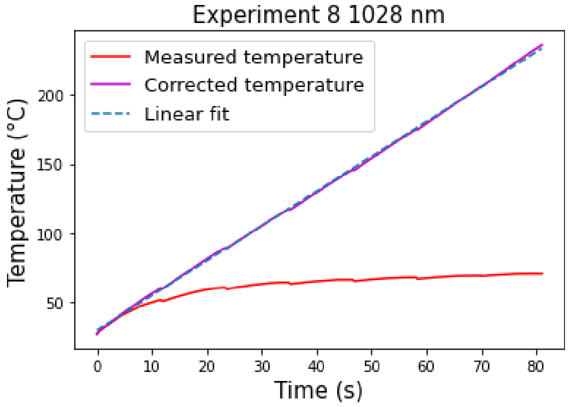
Experiment 8 1028 nm
Measured temperature
Corrected temperature
Linear fit
Temperature (°C)
50
100
150
200
0
10
20
30
40
50
60
70
80
Time (s)

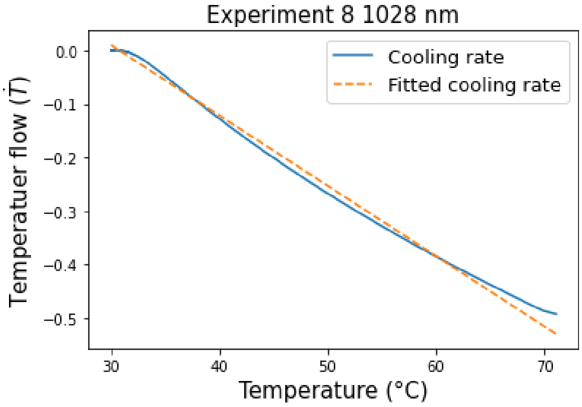
Experiment 8 1028 nm
Cooling rate
Fitted cooling rate
Temperatuer flow ($\dot{T}$)
0.0
−0.1
−0.2
−0.3
−0.4
−0.5
30
40
50
60
70
Temperature (°C)

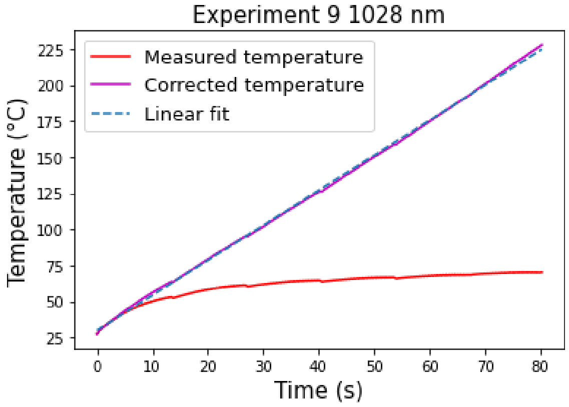
Experiment 9 1028 nm
Measured temperature
Corrected temperature
Linear fit
Temperature (°C)
25
50
75
100
125
150
175
200
225
0
10
20
30
40
50
60
70
80
Time (s)

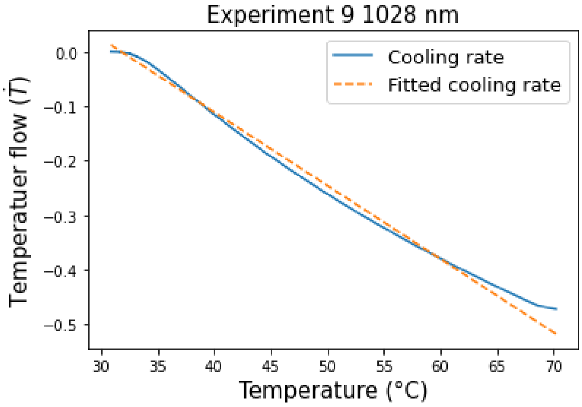
Experiment 9 1028 nm
Cooling rate
Fitted cooling rate
Temperatuer flow ($\dot{T}$)
0.0
−0.1
−0.2
−0.3
−0.4
−0.5
30
35
40
45
50
55
60
65
70
Temperature (°C)

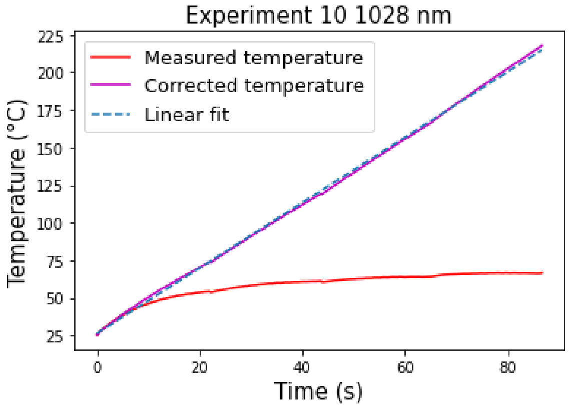
Experiment 10 1028 nm
Measured temperature
Corrected temperature
Linear fit
Temperature (°C)
25
50
75
100
125
150
175
200
225
0
20
40
60
80
Time (s)

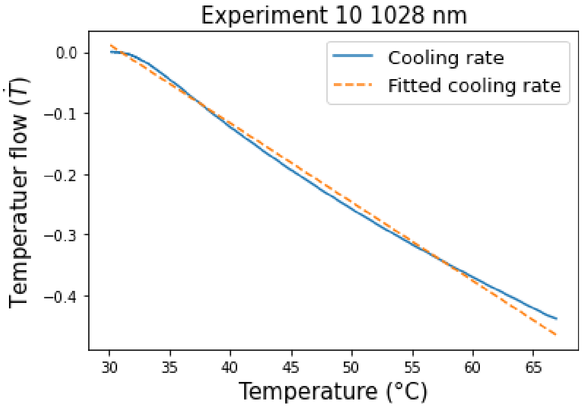
Experiment 10 1028 nm
Cooling rate
Fitted cooling rate
Temperatuer flow ($\dot{T}$)
0.0
−0.1
−0.2
−0.3
−0.4
30
35
40
45
50
55
60
65
Temperature (°C)

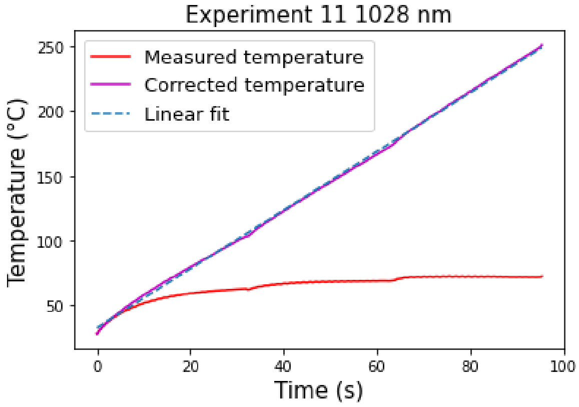
Experiment 11 1028 nm
Measured temperature
Corrected temperature
Linear fit
Temperature (°C)
50
100
150
200
250
0
20
40
60
80
100
Time (s)

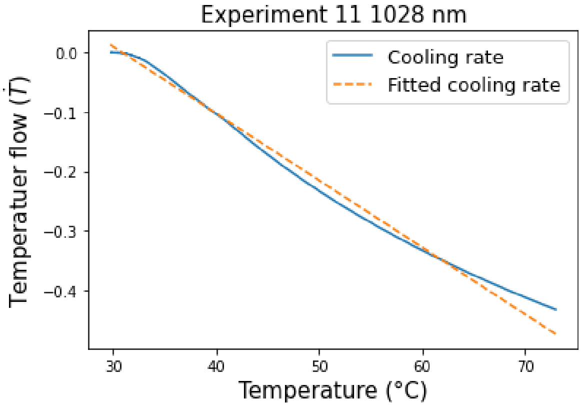
Experiment 11 1028 nm
Cooling rate
Fitted cooling rate
Temperatuer flow ($\dot{T}$)
0.0
−0.1
−0.2
−0.3
−0.4
30
40
50
60
70
Temperature (°C)

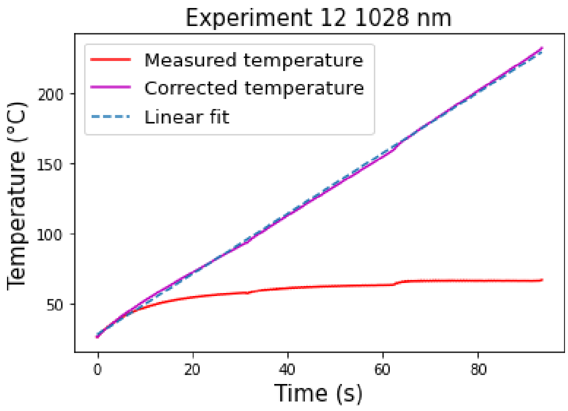
Experiment 12 1028 nm
Measured temperature
Corrected temperature
Linear fit
Temperature (°C)
50
100
150
200
Time (s)
0
20
40
60
80

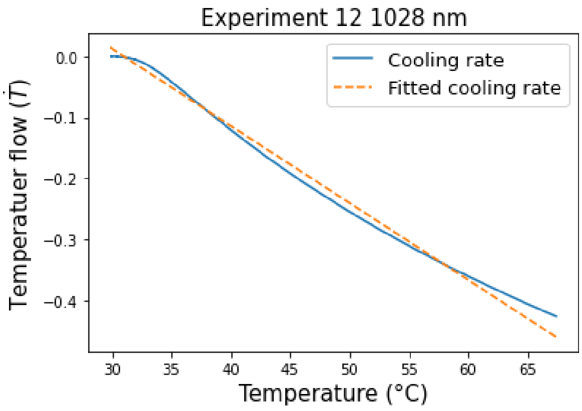
Experiment 12 1028 nm
Cooling rate
Fitted cooling rate
Temperatuer flow $(\dot{T})$
0.0
−0.1
−0.2
−0.3
−0.4
Temperature (°C)
30
35
40
45
50
55
60
65

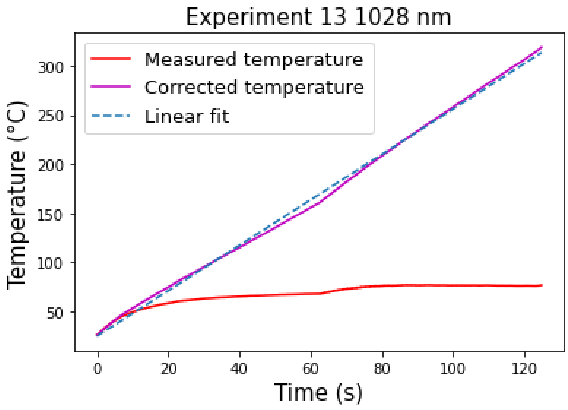
Experiment 13 1028 nm
Measured temperature
Corrected temperature
Linear fit
Temperature (°C)
50
100
150
200
250
300
Time (s)
0
20
40
60
80
100
120

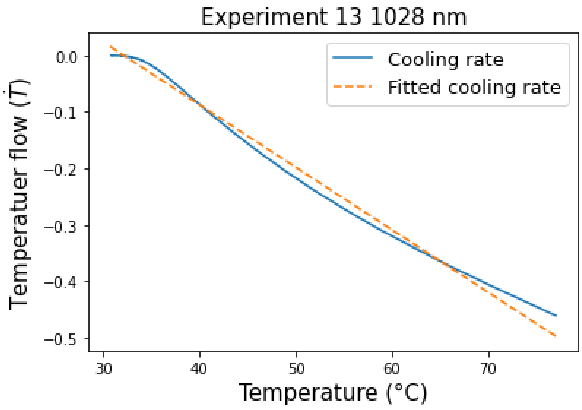
Experiment 13 1028 nm
Cooling rate
Fitted cooling rate
Temperatuer flow $(\dot{T})$
0.0
−0.1
−0.2
−0.3
−0.4
−0.5
Temperature (°C)
30
40
50
60
70

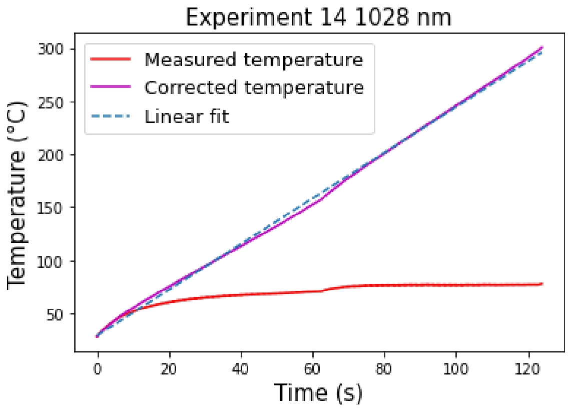
Experiment 14 1028 nm
Measured temperature
Corrected temperature
Linear fit
Temperature (°C)
50
100
150
200
250
300
Time (s)
0
20
40
60
80
100
120

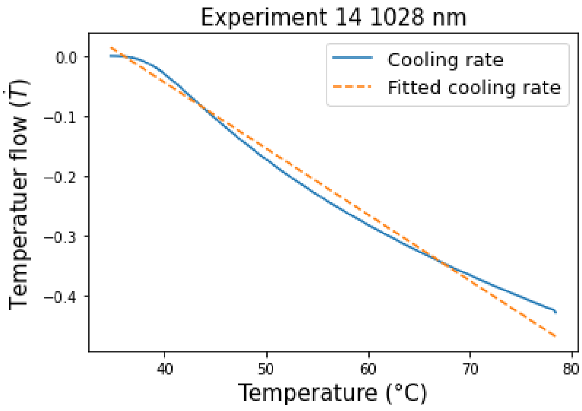
Experiment 14 1028 nm
Cooling rate
Fitted cooling rate
Temperatuer flow $(\dot{T})$
0.0
−0.1
−0.2
−0.3
−0.4
Temperature (°C)
40
50
60
70
80

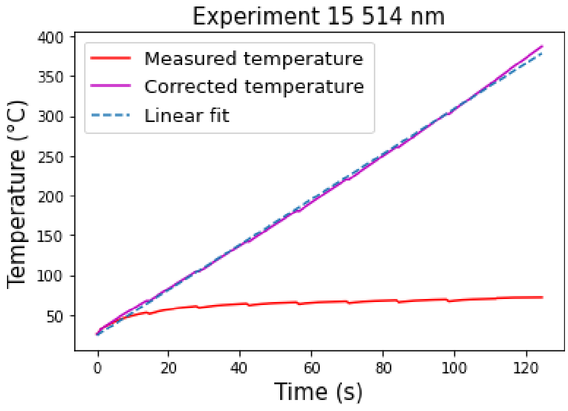
Experiment 15 514 nm
Measured temperature
Corrected temperature
Linear fit
Temperature (°C)
50
100
150
200
250
300
350
400
Time (s)
0
20
40
60
80
100
120

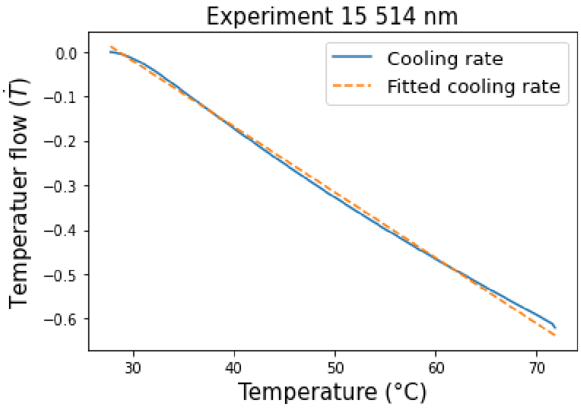
Experiment 15 514 nm
Cooling rate
Fitted cooling rate
Temperatuer flow $(\dot{T})$
0.0
−0.1
−0.2
−0.3
−0.4
−0.5
−0.6
Temperature (°C)
30
40
50
60
70

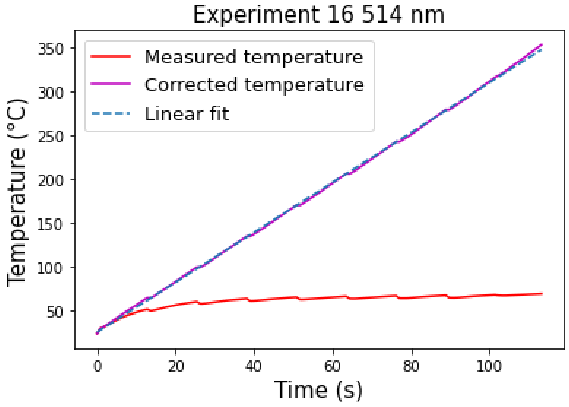
Experiment 16 514 nm
Measured temperature
Corrected temperature
Linear fit
Temperature (°C)
350
300
250
200
150
100
50
0
20
40
60
80
100
Time (s)

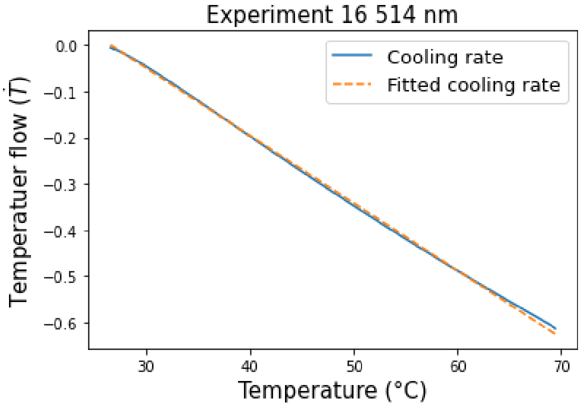
Experiment 16 514 nm
Cooling rate
Fitted cooling rate
Temperatuer flow ($\dot{T}$)
0.0
−0.1
−0.2
−0.3
−0.4
−0.5
−0.6
30
40
50
60
70
Temperature (°C)

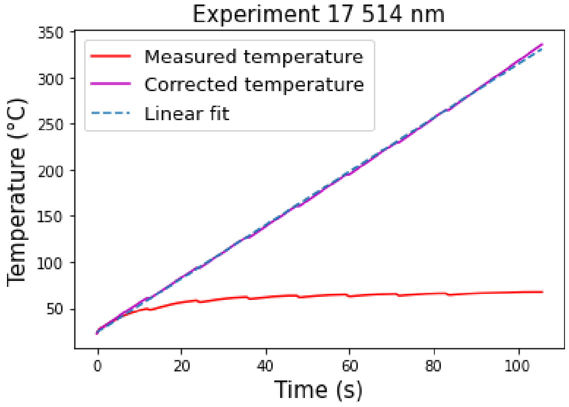
Experiment 17 514 nm
Measured temperature
Corrected temperature
Linear fit
Temperature (°C)
350
300
250
200
150
100
50
0
20
40
60
80
100
Time (s)

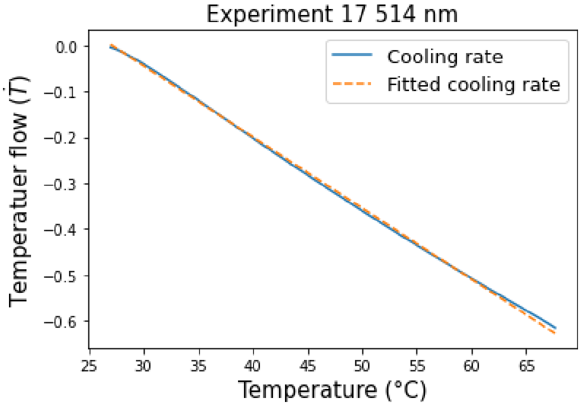
Experiment 17 514 nm
Cooling rate
Fitted cooling rate
Temperatuer flow ($\dot{T}$)
0.0
−0.1
−0.2
−0.3
−0.4
−0.5
−0.6
25
30
35
40
45
50
55
60
65
Temperature (°C)

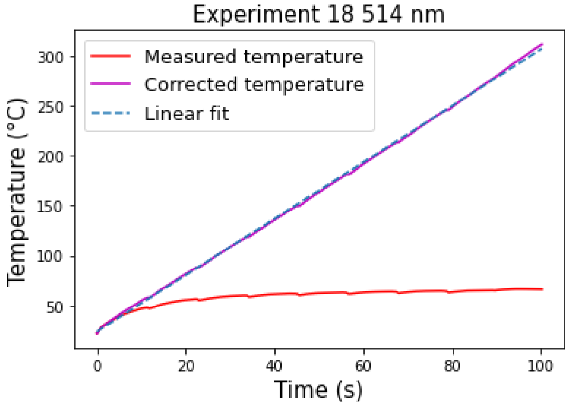
Experiment 18 514 nm
Measured temperature
Corrected temperature
Linear fit
Temperature (°C)
300
250
200
150
100
50
0
20
40
60
80
100
Time (s)

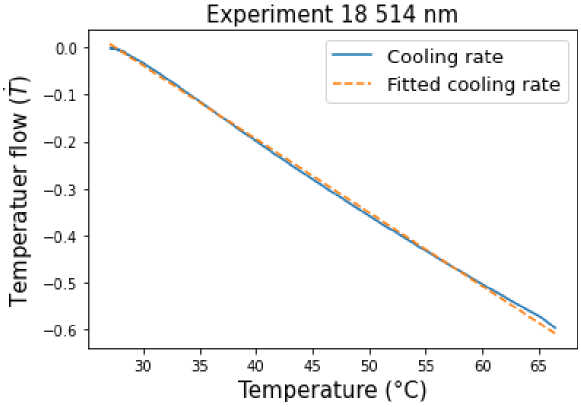
Experiment 18 514 nm
Cooling rate
Fitted cooling rate
Temperatuer flow ($\dot{T}$)
0.0
−0.1
−0.2
−0.3
−0.4
−0.5
−0.6
30
35
40
45
50
55
60
65
Temperature (°C)

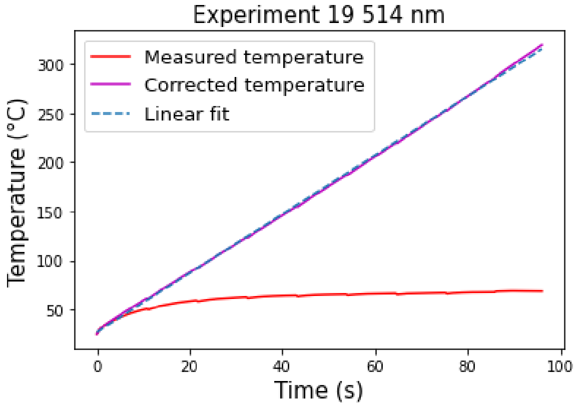
Experiment 19 514 nm
Measured temperature
Corrected temperature
Linear fit
Temperature (°C)
300
250
200
150
100
50
0
20
40
60
80
100
Time (s)

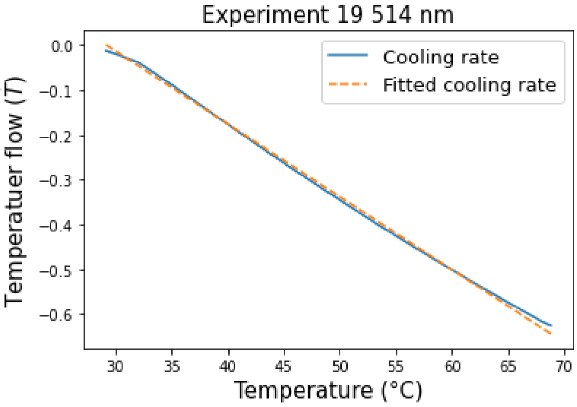
Experiment 19 514 nm
Cooling rate
Fitted cooling rate
Temperatuer flow ($\dot{T}$)
0.0
−0.1
−0.2
−0.3
−0.4
−0.5
−0.6
30
35
40
45
50
55
60
65
70
Temperature (°C)

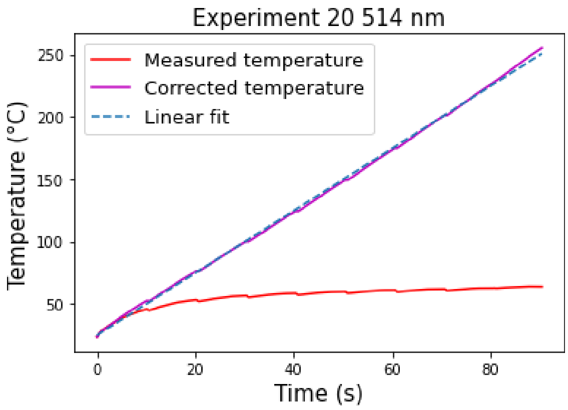
Experiment 20 514 nm
Temperature (°C)
Time (s)
Measured temperature
Corrected temperature
Linear fit
250
200
150
100
50
0
20
40
60
80

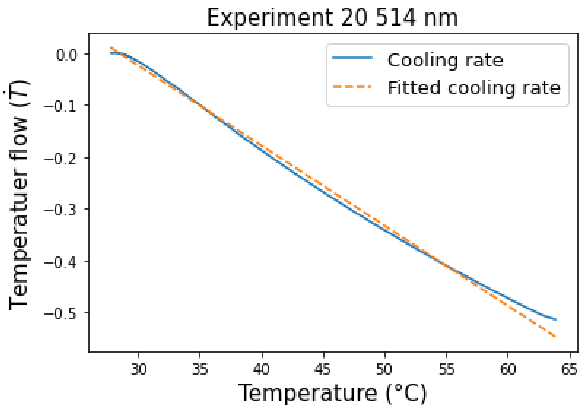
Experiment 20 514 nm
Temperatuer flow $(\dot{T})$
Temperature (°C)
Cooling rate
Fitted cooling rate
0.0
−0.1
−0.2
−0.3
−0.4
−0.5
30
35
40
45
50
55
60
65

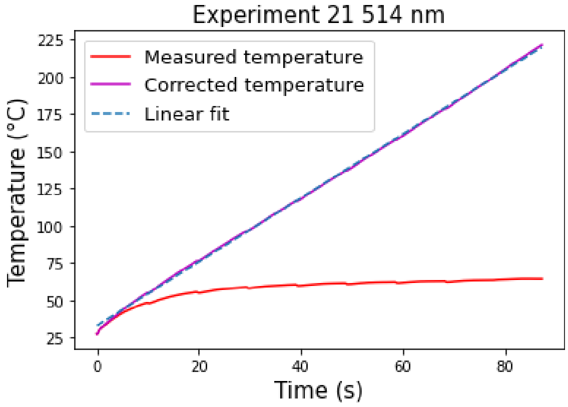
Experiment 21 514 nm
Temperature (°C)
Time (s)
Measured temperature
Corrected temperature
Linear fit
225
200
175
150
125
100
75
50
25
0
20
40
60
80

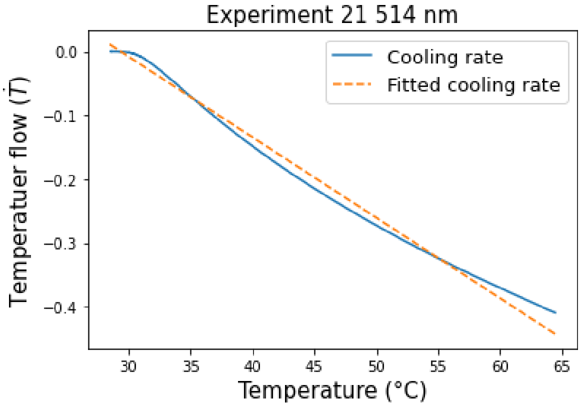
Experiment 21 514 nm
Temperatuer flow $(\dot{T})$
Temperature (°C)
Cooling rate
Fitted cooling rate
0.0
−0.1
−0.2
−0.3
−0.4
30
35
40
45
50
55
60
65

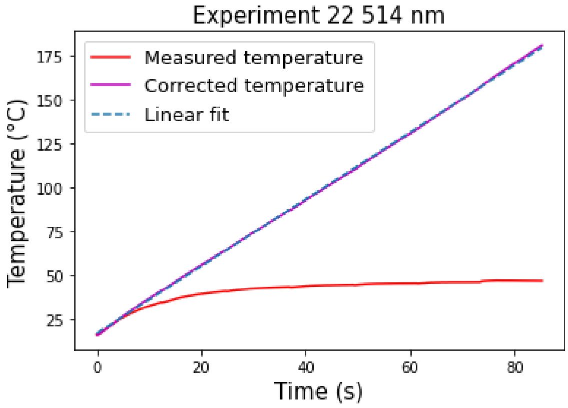
Experiment 22 514 nm
Temperature (°C)
Time (s)
Measured temperature
Corrected temperature
Linear fit
175
150
125
100
75
50
25
0
20
40
60
80

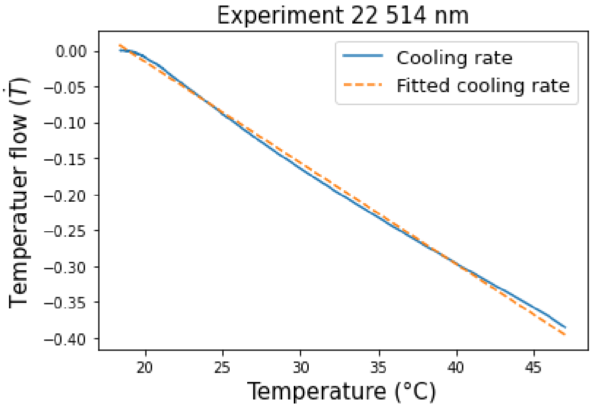
Experiment 22 514 nm
Temperatuer flow $(\dot{T})$
Temperature (°C)
Cooling rate
Fitted cooling rate
0.00
−0.05
−0.10
−0.15
−0.20
−0.25
−0.30
−0.35
−0.40
20
25
30
35
40
45

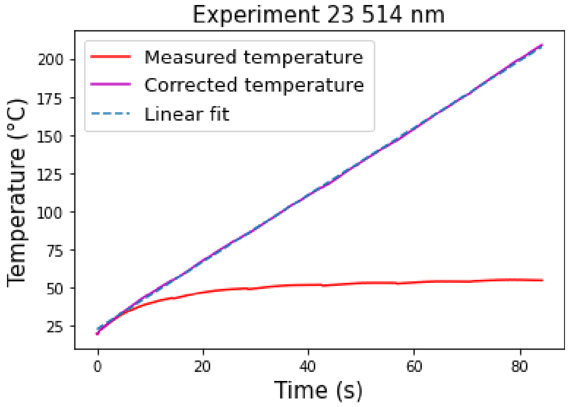
Experiment 23 514 nm
Temperature (°C)
Time (s)
Measured temperature
Corrected temperature
Linear fit
200
175
150
125
100
75
50
25
0
20
40
60
80

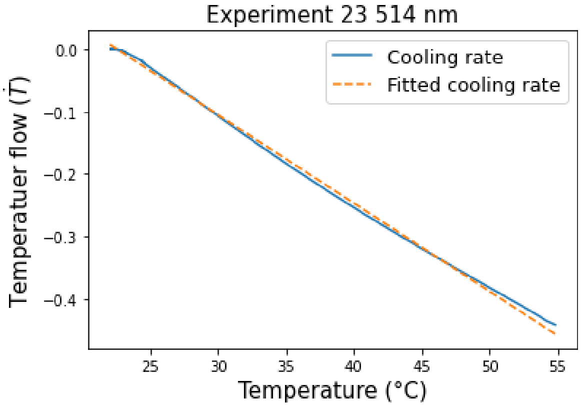
Experiment 23 514 nm
Temperatuer flow $(\dot{T})$
Temperature (°C)
Cooling rate
Fitted cooling rate
0.0
−0.1
−0.2
−0.3
−0.4
25
30
35
40
45
50
55

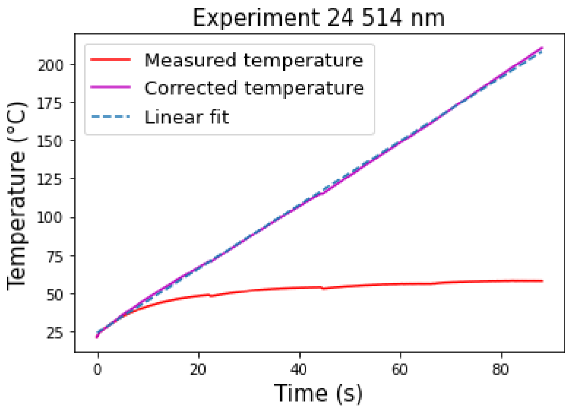
Experiment 24 514 nm

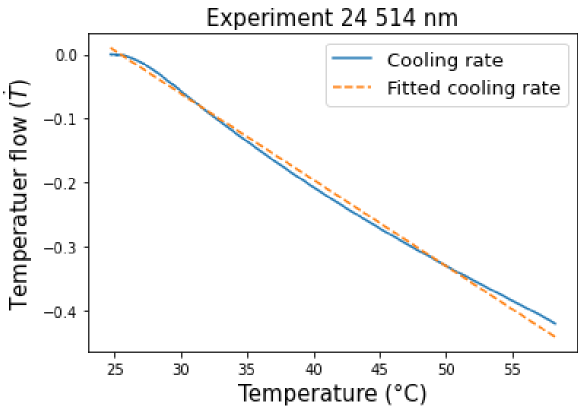
Experiment 24 514 nm

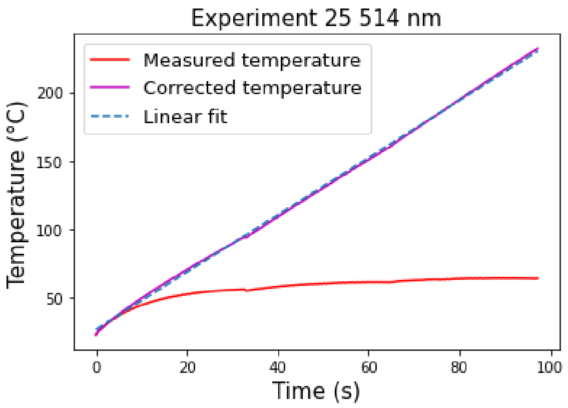
Experiment 25 514 nm

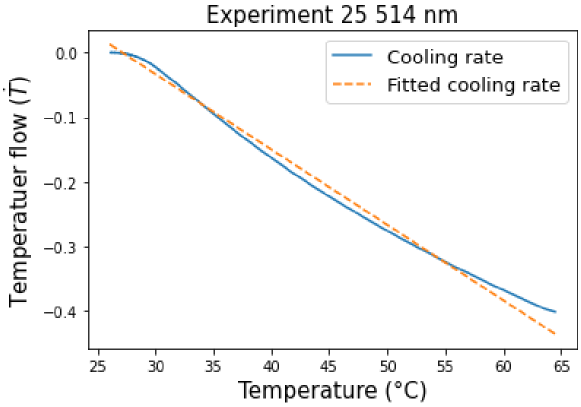
Experiment 25 514 nm

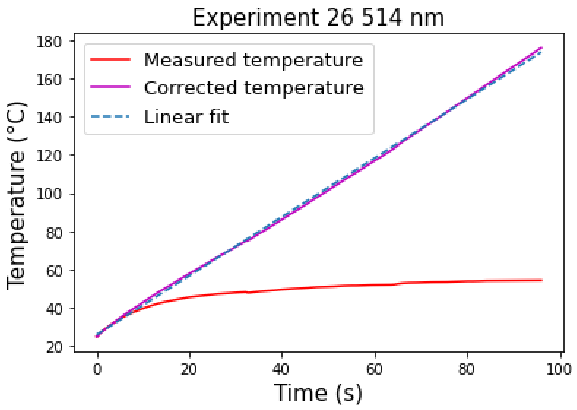
Experiment 26 514 nm

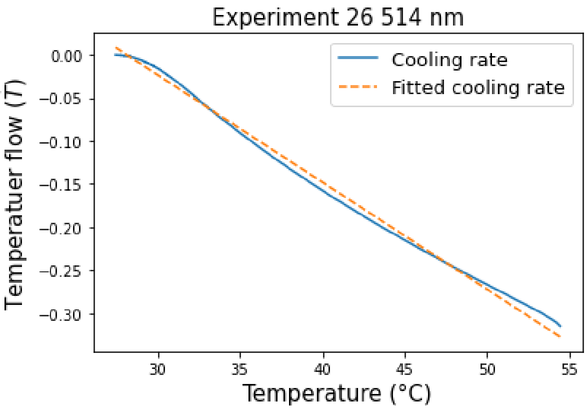
Experiment 26 514 nm

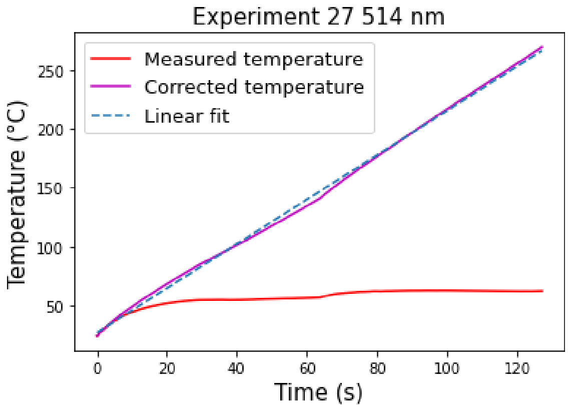
Experiment 27 514 nm

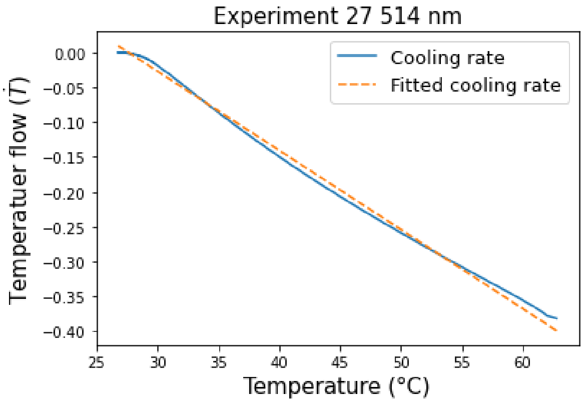
Experiment 27 514 nm

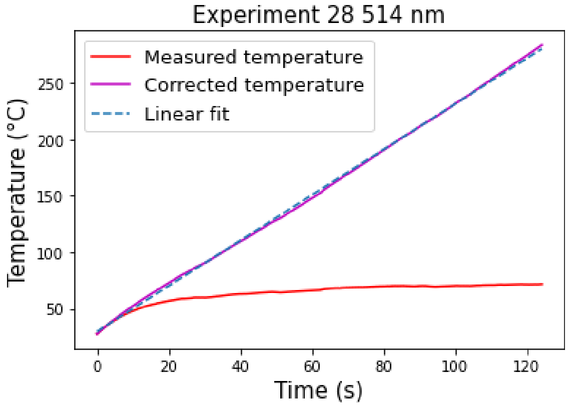
Experiment 28 514 nm
Measured temperature
Corrected temperature
Linear fit
Temperature (°C)
250
200
150
100
50
0
20
40
60
80
100
120
Time (s)

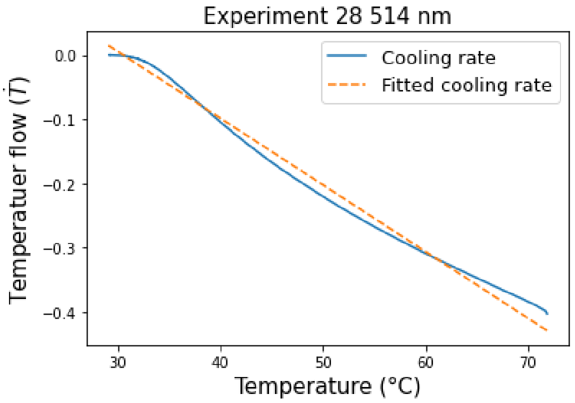
Experiment 28 514 nm
Cooling rate
Fitted cooling rate
Temperatuer flow (Ṫ)
0.0
−0.1
−0.2
−0.3
−0.4
30
40
50
60
70
Temperature (°C)

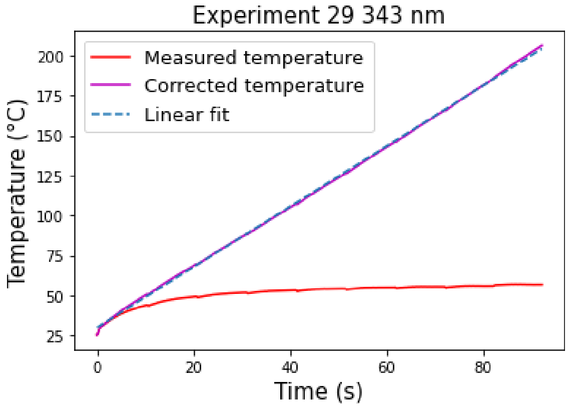
Experiment 29 343 nm
Measured temperature
Corrected temperature
Linear fit
Temperature (°C)
200
175
150
125
100
75
50
25
0
20
40
60
80
Time (s)

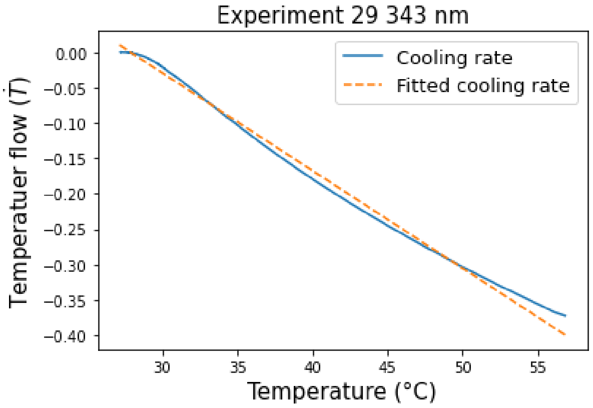
Experiment 29 343 nm
Cooling rate
Fitted cooling rate
Temperatuer flow (Ṫ)
0.00
−0.05
−0.10
−0.15
−0.20
−0.25
−0.30
−0.35
−0.40
30
35
40
45
50
55
Temperature (°C)

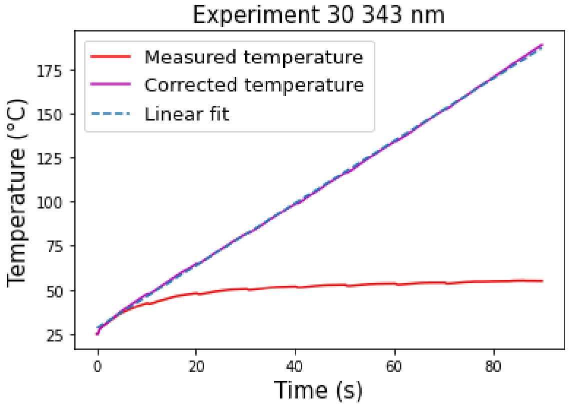
Experiment 30 343 nm
Measured temperature
Corrected temperature
Linear fit
Temperature (°C)
175
150
125
100
75
50
25
0
20
40
60
80
Time (s)

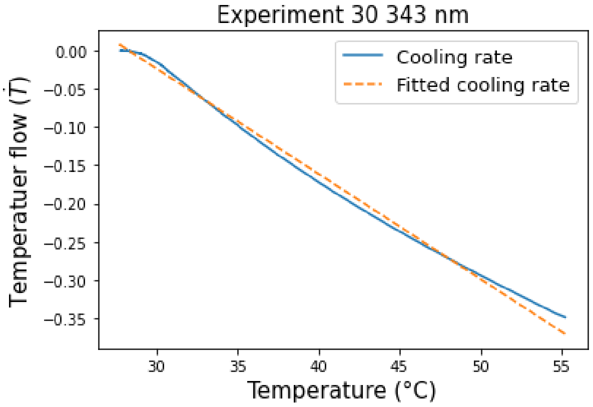
Experiment 30 343 nm
Cooling rate
Fitted cooling rate
Temperatuer flow (Ṫ)
0.00
−0.05
−0.10
−0.15
−0.20
−0.25
−0.30
−0.35
30
35
40
45
50
55
Temperature (°C)

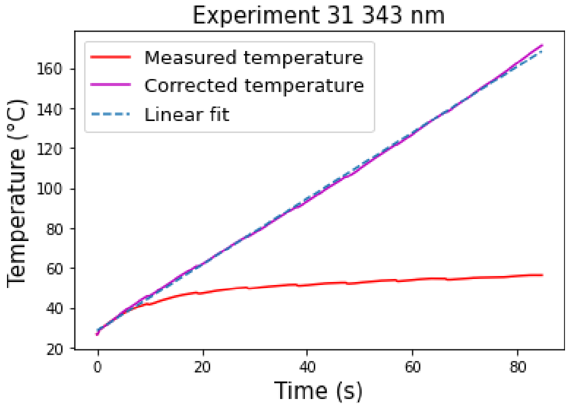
Experiment 31 343 nm
Measured temperature
Corrected temperature
Linear fit
Temperature (°C)
160
140
120
100
80
60
40
20
0
20
40
60
80
Time (s)

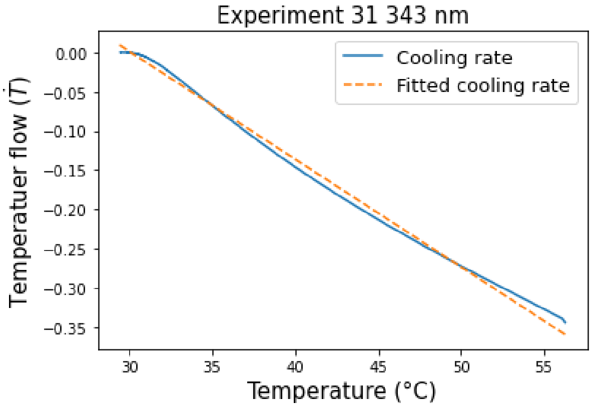
Experiment 31 343 nm
Cooling rate
Fitted cooling rate
Temperatuer flow (Ṫ)
0.00
−0.05
−0.10
−0.15
−0.20
−0.25
−0.30
−0.35
30
35
40
45
50
55
Temperature (°C)

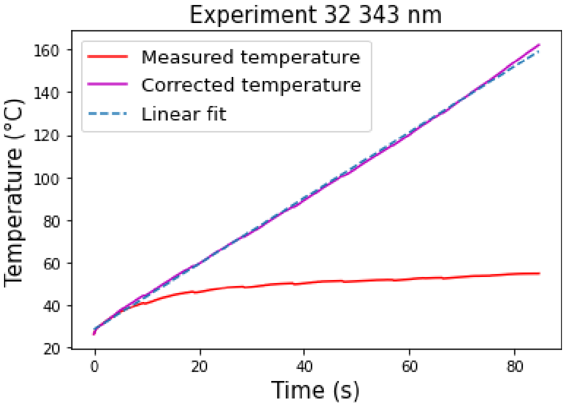
Experiment 32 343 nm
Measured temperature
Corrected temperature
Linear fit
Temperature (°C)
Time (s)
20
40
60
80
100
120
140
160
0
20
40
60
80

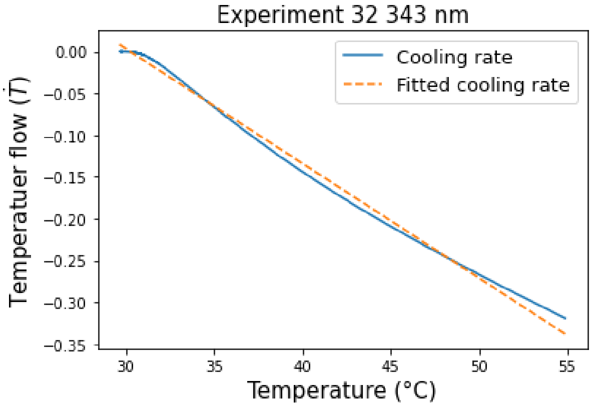
Experiment 32 343 nm
Cooling rate
Fitted cooling rate
Temperatuer flow ($\dot{T}$)
Temperature (°C)
0.00
−0.05
−0.10
−0.15
−0.20
−0.25
−0.30
−0.35
30
35
40
45
50
55

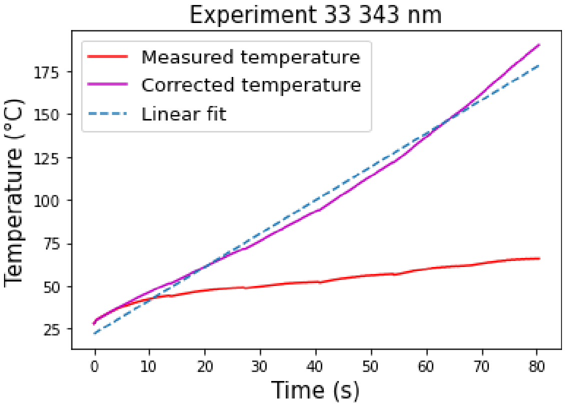
Experiment 33 343 nm
Measured temperature
Corrected temperature
Linear fit
Temperature (°C)
Time (s)
25
50
75
100
125
150
175
0
10
20
30
40
50
60
70
80

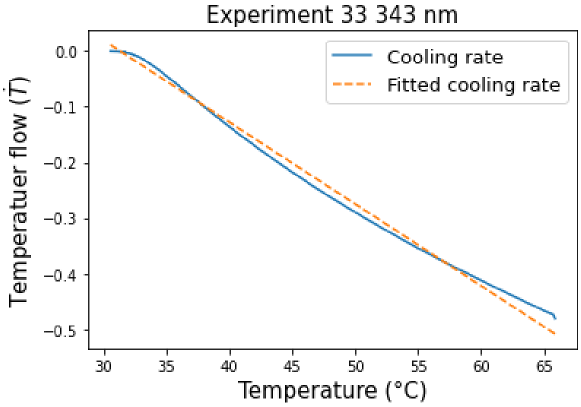
Experiment 33 343 nm
Cooling rate
Fitted cooling rate
Temperatuer flow ($\dot{T}$)
Temperature (°C)
0.0
−0.1
−0.2
−0.3
−0.4
−0.5
30
35
40
45
50
55
60
65

APPENDIX E

Source code for determination of the spot diameter, in this case for 343 nm.

```python
# -*- coding: utf-8 -*-
"""
Created on Tue Feb 21 13:47:45 2023

for the fitting and measurement of the spotsize of a laser via the
knife-edge method

@author: Jelmer Maarten Vis
"""

import pandas as pd
import matplotlib.pyplot as plt
import math
from scipy.optimize import curve_fit
from scipy import special

#import data
curve1 = pd.read_csv("Curve1.csv", encoding="UTF-16 LE", header=None,
decimal=",", sep="\t")
curve1 = curve1[1:-1].to_numpy()

#complementary error function with offset:
def erfc(h, Poff, P, ho,w):
    return Poff+0.5*P*special.erfc((h-ho)/(w/math.sqrt(2)))

#curve fit
popt,pcov = curve_fit(erfc,curve1[:,0],curve1[:,1], p0 =
[0.42,69.3,20,30])

#plot data
plt.plot(curve1[:,0], curve1[:,1], label = "Measurement data")
plt.plot(curve1[:,0], erfc(curve1[:,0],popt[0],popt[1],popt[2],popt[3]),
label = "Fitted error function")
plt.axvline(x = popt[2]-popt[3], color = "r", linestyle = "--",
linewidth = 1, label = "Lower spot size (1/e² )")
plt.axvline(x = popt[2]+popt[3], color = "r", linestyle = "--",
linewidth = 1, label = "Upper spot size (1/e² )")
plt.axvline(x = popt[2], color ="g", linestyle = "--", linewidth = 1,
label = "Spot centre")
plt.ylabel("Average laser power (mW)", fontsize = 12)
plt.xlabel("Knife edge distance (µm)", fontsize = 12)
plt.title("Knife-edge spot size measurement 343 nm", fontsize = 12)
plt.legend(fontsize = 11)
plt.show()

print("spotsize radius is {} µm".format(round(popt[3],2)))
print("spotsize diameter is {} µm".format(round(2*popt[3],2)))
```

Source code for the calculation of the ablation efficiency and heat input. In this case for 1028 nm.

```
# -*- coding: utf-8 -*-
"""
Created on Fri Dec 16 19:08:29 2022

@author: Jelmer Maarten Vis
"""
import numpy as np
import matplotlib.pyplot as plt
from scipy.optimize import curve_fit
import pandas as pd

mass = 0.02525      #gr
measurestep = 0.2   #seconds per measurement step
c = 475             #J/kgK

##Import data function
def importfunc(filename, cs_power,avg_power, time, titlename):
    matrix = pd.read_csv(filename+'.csv', encoding="UTF-16 LE",
header=None,…
    decimal=",", sep="\t")
    matrix = matrix.to_numpy()
    splitvalue = np.argmax(matrix)
    heat_matrix = matrix[0:splitvalue]
    cool_matrix = matrix[splitvalue:len(matrix)]

    #calc cooldown fuction
    def func(time, a, r, c):
       return a * np.exp(-r * time) + c
    popt,pcov = curve_fit(func,np.linspace(0,len(cool_matrix[:,0])-1…
    ,len(cool_matrix[:,0])),cool_matrix[:,0], p0 = [0.1,0.1,25])

    #Calculate temperature if there was no cooling
    r = popt[1]
    a = popt[0]
    dTdt = -r*a*np.exp(-r*(np.linspace(0,len(cool_matrix[:,0])-1…
    ,len(cool_matrix[:,0]))))
    plt.figure()
    plt.plot(cool_matrix[:,0], dTdt, label="Cooling rate")
    plt.xlabel("Temperature (°C)", fontsize = 15)
    plt.ylabel(r"Temperatuer flow ($\dot{T}$)", fontsize = 15)
    plt.title(titlename+" 1028 nm", fontsize = 15)
    def func2(x,a,b):
     return a*x+b
    popt1,pcov1 = curve_fit(func2,cool_matrix[:,0],dTdt)
    plt.plot(cool_matrix[:,0],func2(cool_matrix[:,0],popt1[0],popt1[1])…
    ,"--",label = "Fitted cooling rate")
    plt.legend(fontsize = 13)
    temploss1 = func2(heat_matrix[:,0],popt1[0],popt1[1])
    tottemp1 = 0*heat_matrix[:,0]
    for i in range(len(heat_matrix[:,0])):
        tottemp1[i] = heat_matrix[:,0][i]-np.sum(temploss1[0:i])
    popt2,pcov2 = curve_fit(func2,np.linspace(0,len(heat_matrix[:,0])-1…
    ,len(heat_matrix[:,0])),tottemp1)

    time = np.arange(0,len(heat_matrix[:,0])/5, 0.2)
    plt.figure()
    plt.plot(time,heat_matrix[:,0], color = "r", label = "Measured
temperature")
    plt.plot(time,tottemp1, color = "m", label = "Corrected temperature")
    plt.plot(time,popt2[0]*np.linspace(0,len(heat_matrix[:,0])-1…
    ,len(heat_matrix[:,0]))+popt2[1], linestyle = "--", label = "Linear
fit")
    plt.legend(fontsize = 13)
    plt.xlabel("Time (s)", fontsize = 15)
    plt.ylabel("Temperature (°C)", fontsize = 15)
    plt.title(titlename+" 1028 nm", fontsize = 15)
    print(popt1[0]*5*(mass/1000)*c)
    REC = popt2[0]*5*(mass/1000)*c/avg_power
    print("REC = {}%".format(round(REC*100,2)))
    data = ([REC])
    return data

## Import data. Filename, constant power, average power, time, titlename
temp1 = importfunc("temp1", 0.100, 0.0623, 117.2, "Experiment 1")
temp2 = importfunc("temp2", 0.100, 0.0674, 102.3, "Experiment 2")
temp3 = importfunc("temp3", 0.100, 0.0719, 96.43, "Experiment 3")
temp4 = importfunc("temp4", 0.100, 0.0751, 92.59, "Experiment 4")
temp5 = importfunc("temp5", 0.100, 0.0778, 90.24, "Experiment 5")
temp6 = importfunc("temp6", 0.100, 0.0795, 86.09, "Experiment 6")
temp7 = importfunc("temp7", 0.100, 0.0832, 83.77, "Experiment 7")
temp8 = importfunc("temp8", 0.100, 0.087, 83.18, "Experiment 8")
temp9 = importfunc("temp9", 0.100, 0.0898, 82.23, "Experiment 9")
temp10 = importfunc("temp10", 0.100, 0.0927, 88.7, "Experiment 10")
temp11 = importfunc("temp11", 0.100, 0.0948, 97.59, "Experiment 11")
temp12 = importfunc("temp12", 0.100, 0.0975, 127.05, "Experiment 12")
temp13 = importfunc("temp13", 0.100, 0.0944, 92.7, "Experiment 13")
temp14 = importfunc("temp14", 0.100, 0.0971, 124.04, "Experiment 14")

peakfluencelist =
np.array([0.2,0.25,0.3,0.35,0.4,0.5,0.6,0.8,1,1.5,2,3,2.5,4])
REClist = [temp1[0],temp2[0],temp3[0],temp4[0],temp5[0],temp6[0],temp7[0]…
,temp8[0],temp9[0],temp10[0],temp11[0],temp12[0],temp13[0],temp14[0]]

#import ablation effiencies
eff = pd.read_csv('ableff.csv', encoding="UTF-16 LE", header=None,
decimal=",",…
sep="\t")
eff = eff.to_numpy()

volumes = eff[:,1]/1000000000
efficiency = volumes*0
efficiency[0] = volumes[0]/(0.0623*(117.2/60))
efficiency[1] = volumes[1]/(0.0674*(102.3/60))
efficiency[2] = volumes[2]/(0.0719*(96.43/60))
efficiency[3] = volumes[3]/(0.0751*(92.59/60))
efficiency[4] = volumes[4]/(0.0778*(90.24/60))
efficiency[5] = volumes[5]/(0.0795*(86.09/60))
efficiency[6] = volumes[6]/(0.0832*(83.77/60))
efficiency[7] = volumes[7]/(0.087*(83.18/60))
efficiency[8] = volumes[8]/(0.0898*(82.23/60))
efficiency[9] = volumes[9]/(0.0927*(88.7/60))
efficiency[10] = volumes[10]/(0.0948*(97.59/60))
efficiency[11] = volumes[11]/(0.0975*(127.05/60))
efficiency[12] = volumes[12]/(0.0944*(93.7/60))
efficiency[13] = volumes[13]/(0.0971*(124.04/60))

plt.figure()
plt.plot(peakfluencelist, REClist, 'ro', label = 'REC', marker = "^")
plt.plot(peakfluencelist,efficiency,'bo', label = 'Ablation efficiency')
plt.errorbar(peakfluencelist,efficiency…
,xerr=(np.multiply(peakfluencelist,0.27)),fmt='none',ecolor = "k"…
,elinewidth = 0.5, capsize = 2)
plt.errorbar(peakfluencelist,REClist…
,xerr=(np.multiply(peakfluencelist,0.27)),fmt='none',ecolor = "k"…
, elinewidth = 0.5, capsize = 2)
plt.errorbar(peakfluencelist,efficiency…
,yerr=(np.multiply(efficiency,(np.divide(0.02,efficiency,)+0.01)))…
,fmt='none',ecolor = "k", elinewidth = 0.5, capsize = 2)
plt.errorbar(peakfluencelist,REClist,yerr=0.04,fmt='none',ecolor = "k",
elinewidth = 0.5, capsize = 2)
plt.xlabel("Peak fluence (J/cm²)")
plt.ylabel("REC (-) / ablation efficiency (mm³/(w·min)")
plt.title("REC and ablation efficiency, AISI 420, 1028 nm")
plt.legend()
plt.axis([0.15,4.5,0,0.7])
plt.xscale("log")
plt.grid(axis = "y")
plt.xticks([0.2,0.5,1,2,4],labels=["0.2","0.5","1","2","4"])
plt.gca().set_aspect("equal")

## Fit ablation model function
def func3 (fl, epd, thres):
    return 0.5*(0.006*epd/fl)*np.log(fl/thres)**2 #0.006 to get epd in nm
popt,pcov = curve_fit(func3,peakfluencelist,efficiency, p0=(15,0.1))
plt.plot(np.arange(0.2,4,0.01),
func3(np.arange(0.2,4,0.01),popt[0],popt[1]), label = "Theoretical model")
print(popt)
plt.legend()
```

Source code for the integrating sphere calculations.

```
# -*- coding: utf-8 -*-
"""
Created on Wed Dec 21 09:00:16 2022

@author: Jelmer Maarten Vis

this script is written to process the data gathered from the
integrating sphere.

"""

import numpy as np
import matplotlib.pyplot as plt
from statistics import mean

##Import text file data

#AISI420 standard measurement 1
AISI420_stan_1_M = np.genfromtxt('AISI 420 gehard
standaard\\Metal.txt')
AISI420_stan_1_W = np.genfromtxt('AISI 420 gehard
standaard\\White.txt')
AISI420_stan_1_D = np.genfromtxt('AISI 420 gehard standaard\\Dark.txt')
Wavelengths_AISI420_stan_1 = AISI420_stan_1_M[:,0]
AISI420_stan_1_M = AISI420_stan_1_M[:,1]
AISI420_stan_1_W = AISI420_stan_1_W[:,1]
AISI420_stan_1_D = AISI420_stan_1_D[:,1]

#AISI420 standard measurement 2
AISI420_stan_2_M = np.genfromtxt('AISI 420 gehard standaard
2\\Metal.txt')
AISI420_stan_2_W = np.genfromtxt('AISI 420 gehard standaard
2\\White.txt')
AISI420_stan_2_D = np.genfromtxt('AISI 420 gehard standaard
2\\Dark.txt')
Wavelengths_AISI420_stan_2 = AISI420_stan_2_M[:,0]
AISI420_stan_2_M = AISI420_stan_2_M[:,1]
AISI420_stan_2_W = AISI420_stan_2_W[:,1]
AISI420_stan_2_D = AISI420_stan_2_D[:,1]

#AISI420 standard measurement VIS fiber
AISI420_stan_VIS_M = np.genfromtxt('AISI 420 gehard standaard VIS
vezel\\Metal.txt')
AISI420_stan_VIS_W = np.genfromtxt('AISI 420 gehard standaard VIS
vezel\\White.txt')
AISI420_stan_VIS_D = np.genfromtxt('AISI 420 gehard standaard VIS
vezel\\Dark.txt')
Wavelengths_AISI420_stan_VIS = AISI420_stan_VIS_M[:,0]
AISI420_stan_VIS_M = AISI420_stan_VIS_M[:,1]
AISI420_stan_VIS_W = AISI420_stan_VIS_W[:,1]
AISI420_stan_VIS_D = AISI420_stan_VIS_D[:,1]




##perform calculations
filtervalue = 0.1
#AISI420 standard measurement 1
```

```
AISI420_stan_1_M_Dcorr = AISI420_stan_1_M-AISI420_stan_1_D  #correct
for dark spectrum
AISI420_stan_1_W_Dcorr = AISI420_stan_1_W-AISI420_stan_1_D
for i in range(len(AISI420_stan_1_W_Dcorr)):   #filter
    if AISI420_stan_1_W_Dcorr[i] < filtervalue:
        AISI420_stan_1_W_Dcorr[i] = 1
    if AISI420_stan_1_M_Dcorr[i] < filtervalue:
        AISI420_stan_1_M_Dcorr[i] = 0
AISI420_stan_1_rel =
100*(AISI420_stan_1_M_Dcorr/AISI420_stan_1_W_Dcorr)      #calculate the
relative value of the dark corrected values

#AISI420 standard measurement 2
AISI420_stan_2_M_Dcorr = AISI420_stan_2_M-AISI420_stan_2_D  #correct
for dark spectrum
AISI420_stan_2_W_Dcorr = AISI420_stan_2_W-AISI420_stan_2_D
for i in range(len(AISI420_stan_2_W_Dcorr)):   #filter
    if AISI420_stan_2_W_Dcorr[i] < filtervalue:
        AISI420_stan_2_W_Dcorr[i] = 1
    if AISI420_stan_2_M_Dcorr[i] < filtervalue:
        AISI420_stan_2_M_Dcorr[i] = 0
AISI420_stan_2_rel =
100*(AISI420_stan_2_M_Dcorr/AISI420_stan_2_W_Dcorr)      #calculate the
relative value of the dark corrected values

#AISI420 standard measurement VIS
AISI420_stan_VIS_M_Dcorr = AISI420_stan_VIS_M-AISI420_stan_VIS_D
#correct for dark spectrum
AISI420_stan_VIS_W_Dcorr = AISI420_stan_VIS_W-AISI420_stan_VIS_D
for i in range(len(AISI420_stan_VIS_W_Dcorr)):   #filter
    if AISI420_stan_VIS_W_Dcorr[i] < filtervalue:
        AISI420_stan_VIS_W_Dcorr[i] = 1
    if AISI420_stan_VIS_M_Dcorr[i] < filtervalue:
        AISI420_stan_VIS_M_Dcorr[i] = 0
AISI420_stan_VIS_rel =
100*(AISI420_stan_VIS_M_Dcorr/AISI420_stan_VIS_W_Dcorr)      #calculate
the relative value of the dark corrected values



## plot results
plt.plot(Wavelengths_AISI420_stan_2, AISI420_stan_2_rel,
label="AISI420_2")
plt.plot(Wavelengths_AISI420_stan_1, AISI420_stan_1_rel,
label="AISI420_1")
plt.plot(Wavelengths_AISI420_stan_VIS, AISI420_stan_VIS_rel,
label="AISI420_VIS")
plt.axis([350,1100,0,500])
plt.title("Relative reflectance of AISI 420 stainless steel")
plt.xlabel("Wavelength [nm]")
plt.ylabel("Metal/white reflected light intensity [%]")
plt.legend()
plt.axis([350, 1100, 0, 200])
plt.grid(axis = "y")
plt.show()

plt.plot(Wavelengths_AISI420_stan_VIS,AISI420_stan_1_W, label = "White
spectrum")
plt.plot(Wavelengths_AISI420_stan_VIS,AISI420_stan_1_D, label = "Dark
spectrum")

```

```
plt.plot(Wavelengths_AISI420_stan_VIS,AISI420_stan_1_M, label = "Metal
spectrum")
# plt.plot(Wavelengths_AISI420_stan_VIS,AISI420_stan_1_W_Dcorr)
plt.title("Measurement results")
plt.xlabel("Wavelength (nm)")
plt.ylabel("Reflected light intensity (counts)")
plt.axis([350,1100,0,20])
plt.legend()
```

Source code for the calculation of the saddle shape deformation for the Philips cases.

```
# -*- coding: utf-8 -*-
"""
Created on Mon Nov 28 09:07:26 2022

@author: Jelmer Maarten Vis
"""

import numpy as np
import matplotlib.pyplot as plt
import math

Height_matrix = np.zeros((2000,2000))       #matrix with the XY
coordinates
a = (9.3892-6.73)/((19100/2)-(18000/2))            #steepness. µm/µm
b = 9.3892-(19100/2)*a                             #crossing with sym.
axis
r = 1
theta = 1

for x in range(len(Height_matrix)):
    for y in range(len(Height_matrix)):
        x1 = x-1000
        y1 = y-1000
        r = math.sqrt(x1**2+y1**2)
        if r < (1970/2) and r > (1634/2):
            if x1 != 0:
                theta = math.atan(y1/x1)
                Height_matrix[x,y] =
((a*(r*10)+b))*((math.sin(2*theta)+1)/2)#devided by 2 due to amplitude
to total height. *10 to go from 10µm to µm

volume = Height_matrix.sum()*(10*10)        #heights times the surface
per pixel
print("volume µm^3",volume)
print("volume mm^3",volume/1000000000)      #volume that needs to be
ablated.

fig = plt.imshow(10-Height_matrix-10, cmap=plt.cm.gray)
plt.title("Deformation in blacklevels   Scale in µm")
plt.xlabel("test")
fig.axes.get_xaxis().set_visible(False)
fig.axes.get_yaxis().set_visible(False)
plt.colorbar()

maxval = Height_matrix.max()
minval = Height_matrix.min()
print("min", minval,"max",maxval)

 ## INNER GROOVE
a = 0            #steepness. 9.3892 µm at 19100 µm dia
b = 2.9516       #crossing with sym. axis

for x in range(len(Height_matrix)):
    for y in range(len(Height_matrix)):
        x1 = x-1000
        y1 = y-1000
        r = math.sqrt(x1**2+y1**2)
        if r < (1400/2) and r > (1050/2):
            if x1 != 0:
                theta = math.atan(y1/x1)
                Height_matrix[x,y] =
((a*(r*10)+b))*((math.sin(2*theta)+1)/2)#devided by 2 due to amplitude
to total height. *10 to go from 10µm to µm



volume = Height_matrix.sum()*(10*10) - volume        #heights times the
surface per pixel, Take away volume of outher ring
print("INNER GROOVE volume µm^3",volume)
print("INNER GROOVE volume mm^3",volume/1000000000)       #volume that
needs to be ablated.

# Calculations for inner circle
# fig = plt.imshow(10-Height_matrix, cmap=plt.cm.gray)
# plt.title("Deformation in blacklevels")
# plt.xlabel("test")
# fig.axes.get_xaxis().set_visible(False)
# fig.axes.get_yaxis().set_visible(False)


maxval = Height_matrix.max()
minval = Height_matrix.min()
print("min", minval,"max",maxval)
```

UNIVERSITY OF TWENTE
Drienerlolaan 5
7522 NB Enschede

P.O.Box 217
7500 AE Enschede

P +31 (0)53 489 9111

info@utwente.nl
www.utwente.nl